GE Global Research
Structural Materials Technologies

1 Research Circle
Schenectady, NY 12309 USA

+1-518-387-4311
rebak@ge.com

30 March 2018

Final Technical Report:

Environmental Cracking and Irradiation Resistant Stainless Steels by Additive Manufacturing

Lead Organization: General Electric Company

Award Number: DE-NE0008428

Technical Point of Contact:

Raul B. Rebak, GE Global Research, 1 Research Circle, Schenectady, NY 12309, USA

Principal Investigators:

Raul B. Rebak, GE Global Research, 1 Research Circle, Schenectady, NY 12309
Xiaoyuan Lou, Auburn University, 283 Wilmore Labs, Auburn, AL 36849

Co-Investigators:

Gary S. Was, University of Michigan, 1921 Cooley Bldg., 2355 Bonisteel Blvd., Ann Arbor MI 48109
Francis T. Bolger, GE-Hitachi Nuclear Energy, 3901 Castle Hayne Road, Wilmington, NC 28402
Frederick A. List III, Oak Ridge National Lab, 2370 Cherahala Blvd, Knoxville, TN 37932

Contributors:

Paul W. Emigh, **Michelle A. Othon**, **Peter L. Andresen**, GE Global Research, 1 Research Circle, Schenectady, NY 12309
Miao Song, **Mi Wang**, University of Michigan, 1921 Cooley Bldg., 2355 Bonisteel Blvd., Ann Arbor MI 48109
Myles L. Connor, **Valerie Andersen**, **David W. Webber**, GE-Hitachi Nuclear Energy, 3901 Castle Hayne Road, Wilmington, NC 28402

Executive Summary

Metal additive manufacturing (AM), or metal 3D printing is an emergent advanced manufacturing method that can create near net shape geometries directly from computer models. This technology can provide the capability to rapidly fabricate complex parts that may be required to enhance the integrity of reactor internals components. Such opportunities may be observed during a plant refueling outage and AM parts can be rapidly custom designed, manufactured and deployed within the outage interval. Additive manufacturing of stainless steel (SS) components can add business benefits on fast delivery on repair hardware, installation tooling, new design prototypes tests, etc. For the nuclear industry, the supply chain is always an issue for reactor service. AM can provide through-life supply chain (40-60 years) for high-value low-volume components. In the meantime, the capability of generating complex geometries and functional gradient materials will improve the performance, reduce the overall component cost, plant asset management cost and increase the plant reliability by the improvement in materials performance in nuclear environments.

While extensive work has been conducted regarding additively manufacturing of austenitic SS parts, most efforts focused only on basic attributes such as porosity, residual stress, basic tensile properties, along with components yield and process monitoring. Little work has been done to define and evaluate the material requirements for nuclear applications. Technical gaps exist, which limit this technology adoption in the nuclear industry, which includes high manufacturing cost, unknown risks, limited nuclear related data, lack of specification and qualification methods, and no prior business experience. The main objective of this program was to generate research data to address all these technical gaps and establish a commercial practice to use AM technology in the nuclear power industry. The detailed objectives are listed as follows:

(1) Evaluate nuclear related properties of AM 316L SS, including microstructure, tensile properties, impact toughness, stress corrosion cracking (SCC), corrosion fatigue (CF), irradiation effects, and irradiation assisted stress corrosion cracking (IASCC).

(2) Understand the correlations among laser processing, heat treatment, microstructure and SCC/irradiation properties;

(3) Optimize and improve the manufacturing process to achieve enhanced nuclear application properties;

(4) Fabricate, evaluate, qualify and test a prototype reactor component to demonstrate the commercial viability and cost benefit;

(5) Create regulatory approval path and commercialization plans for the production of a commercial reactor component.

Table of Contents

1. Introduction

1.1. Background

In recent years, laser powder bed fusion (L-PBF) additive manufacturing (AM) has been widely explored in both the academia and industry [1-5]. It uses a high-power laser to precisely melt and solidify alloy powder layer-by-layer and create a final geometry directly from its 3D computer model. This innovative process offers higher degrees of design freedom and can significantly accelerate the deployment schedule of a new component from design to production. Given the enthusiasm of the aerospace industry for this technology, the nuclear industry is realizing its potentials to produce reactor internal components with improved performance, and reduced supply chain, cost and time to market [6]. The technology also provides a unique capability to rapidly design and fabricate parts and tools during a power plant refuel outage.

A wide range of materials have been studied and manufactured based on L-PBF, including austenitic stainless steel (SS) [7], precipitation hardened SS [8], Co-Cr alloy, Alloy 718 [9], and Titanium 6Al-4V alloy [10]. While extensive work has been conducted to additively fabricate austenitic SS parts, including complex components, most effort focused only on basic attributes such as porosity, residual stress, basic tensile properties, along with component yield and process monitoring [4, 7, 11-14]. Compared to tensile properties, the current understandings of the fracture and cracking behavior of AM metals in nuclear environments are limited [4, 15-17], and little work has been done to define and evaluate the unique material requirements for nuclear applications.

Austenitic 316L SS is used extensively for components both inside and outside the reactor pressure vessel. While it is still challenging to achieve acceptable density and microstructure in other alloys by additive manufacturing, AM 316L SS has achieved significant success with near full density, reasonable tensile properties and fatigue crack growth behavior, and good component yield [7, 11, 14, 18, 19]. However, for nuclear applications, it is well known that austenitic SS may be susceptible to SCC and IASCC in high temperature water (~300°C). SCC can be influenced by temperature, residual plastic strain in the alloy, irradiation damage, sensitization, water chemistry, and electrochemical potential [20-22]. L-PBF utilizes the high local heat density from the laser to fuse and solidify the metal powder. This process results in extremely fast heating and cooling rate and leads to high levels of residual stress and strain inside the material. In addition, higher porosity (compared to wrought material) is expected in AM parts due to incomplete fusion. Hot isostatic pressing (HIP) and heat treatment are normally performed following L-PBF to ensure good microstructure and low porosity. The microstructure of the AM products highly depends on the process parameters. Due to a lack of a forging process, the microstructure after a recrystallization process in an additive component may not be uniform due to a variation in its local cooling rate. Microstructure variations from an AM process (e.g. from machine-to-machine, process-to-process, and location-to-location) can potentially be higher than those from the conventional melting/casting/forging/machining process. The consequences of these variations to fatigue, SCC, and IASCC resistance of AM 316L SS in high temperature water remains unknown in both academia and the industry.

Conversely, the AM 316L SS directly made by L-PBF contains a high density of sub-grain cellular nanostructure, a mixed boundary structure from low to high angle boundaries, and ultrafine precipitated secondary particles. These unique microstructural features may produce beneficial

effects on the mechanical properties, cracking and irradiation resistance of AM materials. By understanding the relationships among laser process, heat treatment, microstructure, and SCC/IASCC properties, the nuclear related required properties may be tailored and improved by utilizing features within the AM manufacturing steps and methods.

While metal additive manufacturing has been investigated in previous projects sponsored by Nuclear Energy Enabling Technologies (NEET), US Department of Energy, technical gaps still exist which limit its commercialization in the nuclear industry. In addition to the unknown nuclear related properties, the nuclear industry around the world has no prior commercial experience on this manufacturing method. Nuclear material specification and qualification method for AM have not been established yet. Research is needed to address the processing and material variability prior to codifying the material for nuclear use. Code and regulatory bodies are skeptical about adopting AM due to the scatter and uneven consistency in metallurgical and mechanical properties. For this newer AM technology, nuclear materials experts have limited experience in many areas, including component design strategy, material performance, qualification/certification, cost structure, repair, etc. Although many nuclear vendors have interest in AM, the technical gaps limit the wide acceptance of AM in the industry.

1.2. Project Overview

The objective of this project was to address all the major technical challenges which may limit the wide acceptance of AM technology in the nuclear energy sector and demonstrate this newer technology on the actual design of nuclear components. The project utilizes the expertise from four different organizations to bring the AM close to commercialization.

L-PBF process was conducted with the collaboration between GE Global Research and Oak Ridge National Lab. Both teams aimed to establish a correlation between laser process, heat treatment and microstructure. The key contribution of this project to the nuclear community was to establish a fundamental understanding of a variety of nuclear properties that are currently not available in both academia and industry, which include microstructure and its evolution during the process, tensile properties, impact toughness, SCC, corrosion fatigue, irradiation effects, and IASCC. Un-irradiated materials were investigated at GE Global Research. SCC and corrosion fatigue crack growth were studied using compact tension (CT) specimens and in-situ crack length measurements was made using a direct current potential drop (DCPD) system. The testing environment was 288^{o}C high temperature water, 20 ppb sulfate, 2 ppm O_2 or 63 ppb H_2 to simulate both oxygenated and hydrogenated BWR water chemistries. The University of Michigan conducted proton irradiation at 2 MeV to a dose in the range 5-10 dpa. The evaluation of the irradiation resistance was based on three critical parameters: (1) microstructure evolution under irradiation; (2) mechanical property changes due to irradiation; and (3) IASCC susceptibility changes after irradiation. The irradiated microstructure was characterized using TEM and APT and analyses were focused on the dislocation loop microstructure, radiation induced precipitation and radiation-induced segregation. Micro-hardness tests were used to evaluate the degree of irradiation hardening. IASCC susceptibility was studied by crack initiation evaluation using SSRT tests conducted to increasing strain levels. A second set of irradiations was conducted using 5 MeV Ni++ and Fe++ ions to high dose (~100 dpa) to evaluate the high dose microstructure of the AM material. The high dose irradiation was useful in determining dimensional (voids) and phase (precipitates) stability at doses relevant for a 60-year reactor component life.

With the comprehensive understanding of the process-microstructure-property relationship, the project also sought to optimize the laser manufacturing process, heat treatment and alloy chemistry

to improve the material properties and reduce the process variability. Different from most AM research, this project focused on the control and optimization of the microstructure which is the key contributor to a local phenomenon such as SCC.

The other mission of this project was to demonstrate the technology on an actual size and geometry nuclear component and develop a path for regulatory approval and nuclear commercialization. GE-Hitachi (GEH) Nuclear Energy, as a major nuclear technology provider, utilized AM technology to support the redesign of their Defender™ advanced debris filtration system. Through the development, the business went through all the key elements which are critical for commercializing AM technology for a nuclear component. The results from the prior 2 years of experimental work were consolidated to form a baseline for GE Nuclear internal AM material specification. GEH has communicated with US Nuclear Regulatory Commission (NRC) about the plans with the AM component. The additive manufacturing design and fabrication process was executed with a rigorous nuclear quality assurance (QA) oversight program to produce three nuclear fuel debris filters. These parts were subjected to material testing and have the fabrication pedigree to be considered for in-reactor use. A GE Nuclear component inspection and qualification program was adapted and executed for the first time on AM parts. This included supplementing the standard GE Nuclear inspection processes with CT and Blue Light scanning to better characterize additive manufacturing tolerances. The cost per part and capital investment requirements for a production scale facility were determined via a mathematical model developed in collaboration with the GE Greenville AMW manufacturing plant. As part of the commercialization analysis, a customer with serious interest in using these AM nuclear in-reactor debris filters was identified.

2. Materials, L-PBF Process and Heat Treatment

2.1. Materials

Austenitic stainless steels are the most common structural materials used in reactor internals and fuel assemblies. Therefore, this project mainly focused on understanding and optimizing AM austenitic stainless steel for nuclear use. Commercial 316L SS powder from Carpenter Powder Products (Bridgeville, PA, USA) was used to fabricate AM 316L SS samples for this research. The powder was sieved using 325 mesh screens. To ensure the reasonable flowability, powder size below 15 µm was limited to < 3 wt%. Table 1 shows the chemical compositions of the as-received powder and the AM made sample. The powder and the fabricated sample had a similar composition and met the ASTM A276 specification [23]. The AM samples had a slight increase in oxygen and carbon, and a decrease in nitrogen, which was probably due to reactions (e.g. oxidation, nitrogen removal) during laser melting.

Table 1. Measured chemical compositions of AM 316L powder and AM 316L made sample studied in this work by inductively coupled plasma optical emission spectrometry and instrumental gas analysis.

Material	Fe wt%	Cr wt%	Mn wt%	Si wt%	Ni wt%	Cu wt%	Mo wt%	V wt%	P wt%	Co wt%	W wt%	C ppm	S ppm	O ppm	N ppm
Powder	Bal.	16.7	1.02	0.74	10.7	0.19	2.29	0.05	0.02	0.13	0.04	221	62	326	1163
AM Part	Bal.	16.9	1.13	0.71	10.7	0.20	2.24	0.05	0.02	0.12	0.03	266	61	384	935

Alloy 800/800H has 40 years' experience in CANDU and Siemens (now AREVA) reactors. Alloy 800 family generally provides better oxidation and creep resistance than austenitic stainless steel. Since it contains less Ni than Ni based alloys, they are considered a good trade-off between cost and performance. Alloy 800/800H class is in the code approved material for GEN IV Reactor. The Alloy 800 powder used in this research was also made by Carpenter Powder Products (Bridgeville, PA, USA) using the gas atomization technique. Table 2 shows the chemical composition of the as-received Alloy 800 powder.

Table 2. Measured chemical compositions of Alloy 800 powder

Material	Fe wt%	Cr wt%	Mn wt%	Si wt%	Ni wt%	Ti wt%	Al wt%	C wt%	O ppm	N ppm
Powder	Bal.	21	0.88	0.62	34	0.41	0.38	0.095	95	30

This project also tried to produce oxide dispersion strengthened (ODS) austenitic stainless steel by promoting the in-situ formation of nano oxide particles. The first attempt showed that the oxygen level was too low to promote a high density of nano oxides in the AM product. Later, due to the organizational change inside GE, the effort of producing ODS AM SS was removed from the project.

2.2. L-PBF process

To evaluate the process-to-process and machine-to-machine variations of AM process, this project evaluated materials produced by three different L-PBF systems (EOS M270, EOS M280, Renishaw AM250) and four different additive manufacturing vendors. The laser process, heat treatment, and

hot isostatic pressing (HIP) conditions were also systematically adjusted to understand the effects of process and heat treatment on the microstructure, porosity, and buildability. Since the study involved a variety of laser parameters, and some of which are business proprietary information for different vendors, this report will not list all the L-PBF processing information. Instead, the report will focus on how the process influenced the microstructural features, and eventually affect the nuclear related properties of the manufactured AM materials.

2.3. Heat treatment

Like laser process, a variety of thermal heat treatment were also used to control the microstructure and understand its effects on environmental cracking and irradiation properties. To give an example how heat treatment controls microstructure, Table 3 shows a list of heat treatments used for a typical L-PBF process with the parameters of 195 W laser power, 1.2 m/s laser scan speed, and 20 µm powder thickness. Four heat treatment conditions were applied to AM 316L SS to assess the effects of microstructural variations: (1) as-built condition from L-PBF; (2) stress relief at 650°C for 2 hours in argon, (3) HIP in argon for 4 hours at 1150°C and 1000 bar, followed by solution annealing (SA) at 1066 ºC for 1 hour, and (4) heat treatment at 955°C for 4 hours in argon. Treatment 2 is called stress relief because it releases some of the residual stress from the as-built component using a low-temperature treatment. Most AM 316L SS parts by AM vendors are supplied using either Treatment 1 or Treatment 2 if a heat treatment condition is not specified by the buyer. Treatment 3 utilized HIP to densify the as-built part and recrystallize its microstructure. After the HIP process, a solution annealing at 1066 ºC for 1 hour followed by a water quench was conducted to remove carbides that might form during the slow cooling following HIP. Treatment 4 (955 °C for 4 hours) was selected to produce a bimodal microstructure involving both recrystallized equiaxed grain (~30% recrystallized) and as-built characteristics, which was used in this study to understand the impact of the retained unrecrystallized grains on SCC. In an AM part, full recrystallization is not always achieved due to the strain variations in the part. Solution-annealed AM materials generally possess some unrecrystallized grains, as discussed later.

Table 3. Heat treatment conditions and microstructural characteristics of the AM 316L SS investigated here.

Condition	Thermal Treatment	Resulting Microstructure
Primary material in this study, Treatment 1 = As-built	None	Anisotropic, retained strain
Primary material in this study, Treatment 2 = Stress relief	650°C for 2h in argon	Anisotropic, retained strain
Primary material in this study, Treatment 3 = HIP + SA	HIP for 4 h at 1150°C and 1000 bar in argon, followed by solution annealing at 1066 ºC for 1 hour	Fully-recrystallized like wrought 316L SS
Primary material in this study, Treatment 4 = Partial recrystallization	955°C for 4 hours in argon	Bimodal, partially-recrystallized (30% recrystallized)
High-porosity material = SA	1150°C for 2 hours in argon	Higher porosity, fully-recrystallized

A higher porosity AM 316L SS was also evaluated to understand the effect of porosity on SCC. This material was recrystallized by solution-annealing, but HIP was not performed. The elimination of HIP, if possible, is considered by GEH as a cost reduction method. In this project, the effect of HIP on SCC susceptibility was also evaluated. Table 4 shows the difference in porosity

between the stress-relieved condition (Treatment 2) and the HIP+SA condition (Treatment 3). The primary heat of AM 316L SS used in this study had reasonably low porosity with small defect size, so the HIP in Treatment 3 did not yield significant improvement. The high porosity heat showed higher porosity and larger pore size.

Table 4. Porosity analysis of AM 316L part before and after hot isostatic pressing process based on ASTM E2109 [24]

	Porosity Mean (%)	**Porosity Std. Dev. (%)**	**Pore Size Mean (µm)**	**Pore Size Std. Dev. (µm)**	**Min. Pore Size (µm)**	**Max. Pore Size (µm)**
Primary material in this study (Stress relief)	0.19	0.08	3.2	3.5	0.9	36.0
Primary material in this study (HIP+SA)	0.08	0.03	2.8	2.3	0.9	27.1
High-porosity material (SA only)	0.3	0.5	16	14.5	2.9	83.9

3. Microstructure

3.1. Grain Structure

Fig. 1 shows the BSE images of AM 316L SS with different heat treatments. As-built and stress-relieved AM 316L SS showed a similar fast cooled solidification structure. The stress relief treatment did not produce a visible change in the microstructure of the as-built material. Under these conditions, AM 316L SS exhibited an anisotropic non-equilibrium microstructure with a directional solidified structure oriented along the material build direction, which has also been reported by other researchers [12, 14, 18, 25]. In the cross-sectional X-Z or Y-Z plane which is parallel to the build direction (Fig. 1b and Fig. 1d), the grains in AM 316L SS exhibited a much higher aspect ratio than those found in the wrought materials, i.e. the AM grains were highly elongated. It is shown later in Fig. 2 that AM 316L SS had a fine columnar structure inside the grains. The average width of the columnar structure was about 300-500 nm, while the length of the grain could be over 100 μm. The formation of such fine structures was a result of the high thermal gradient caused by fast cooling after laser solidification. However, in the X-Y plane (Fig. 1a and Fig. 1c, normal to the build direction), there was no clear anisotropy in the microstructure. Because of some lack of fusion, porosity defects were visible.

Fig. 1e shows the BSE images of AM 316L SS after HIP and SA. The material was fully recrystallized and equiaxed. The plastic residual strain in the as-built material as well as the local deformation from HIP served as the driving force for grain recrystallization. The grain growth kinetics was controlled by the heat treatment temperature and time. The average grain size was approximately 70-100 μm. Recrystallization was not uniform, and variations in grain size were visible. Overall, the material after HIP+SA exhibited coarse grains like its wrought counterpart.

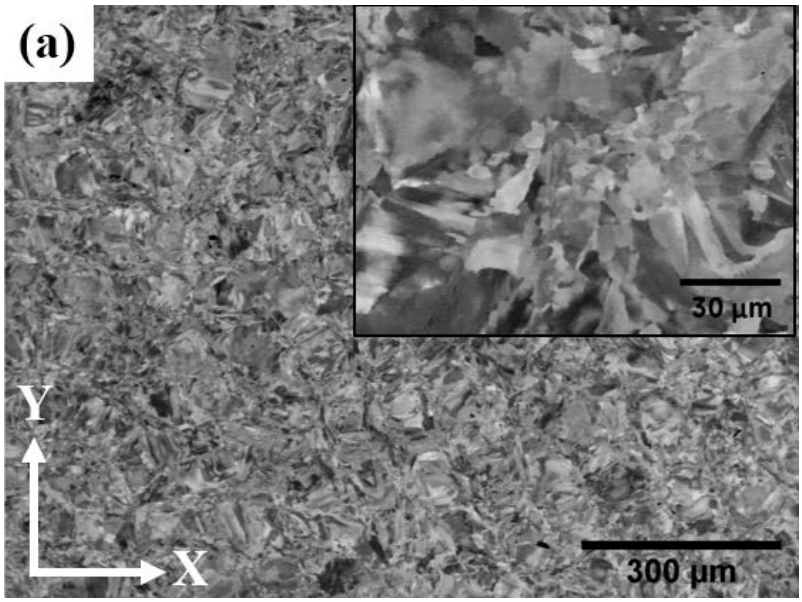

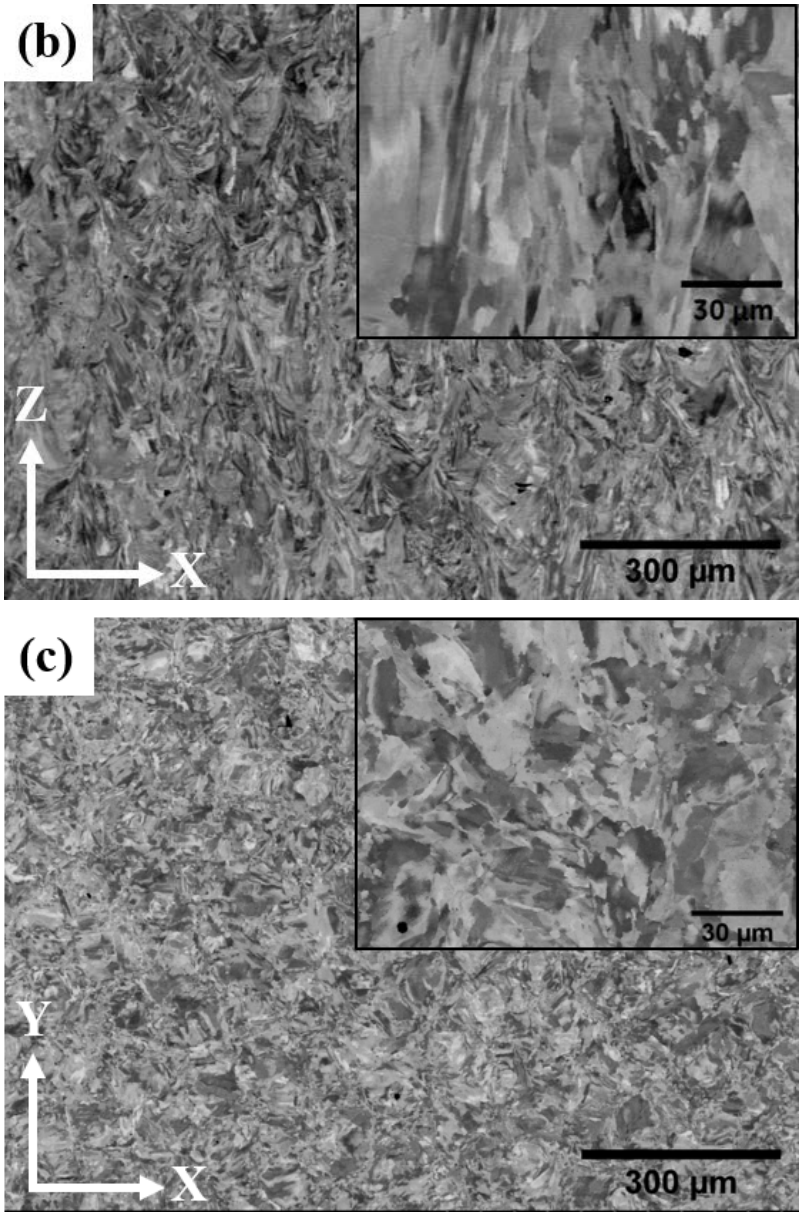
(b)
30 µm
Z
X
300 µm
(c)
30 µm
Y
X
300 µm

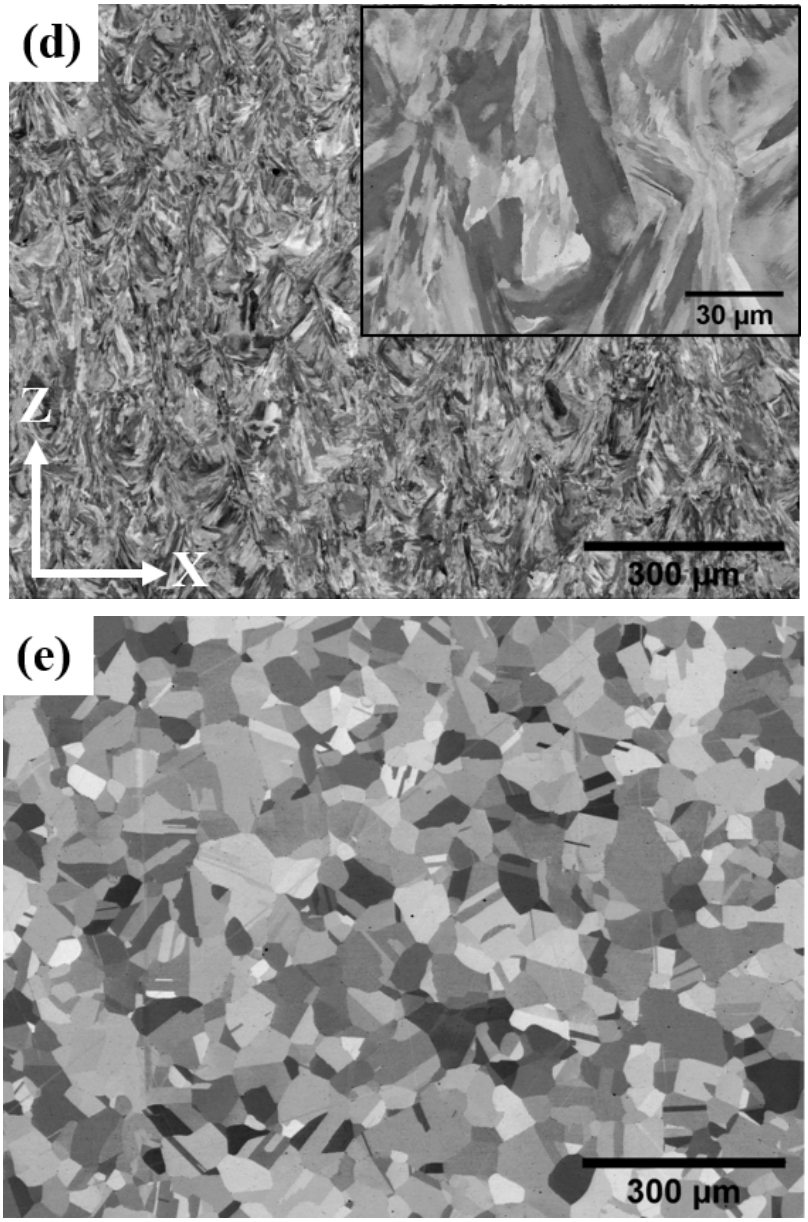

Fig. 1. Back scattered scanning electron (BSE) images of AM 316L SS: (a) as-built, cross-section parallel to powder bed; (b) as-built, cross-section parallel to material build direction Z; (c) stress relief, cross-section parallel to powder bed; (d) stress relief, cross-section parallel to material build direction Z; (e) HIP+SA. The inserts are the high-magnification images.

The details of the grain boundary structure and the residual strain distribution were evaluated by electron backscatter diffraction (EBSD) mapping. Fig. 2 shows the EBSD boundary map and the 10° misorientation map of the stress-relieved material. The AM material after stress relief contained a variety of boundary types from low to high angle boundaries. The grain microstructure formed a hierarchical order from submicron columnar structure to large dendrite grains. The low angle boundaries were between the close-spaced columns, while the high angle boundaries defined the elongated large grains. The microstructure was oriented along the material build direction. Twins were not common in the stress-relieved material. The grain boundary network was not well connected and defined. The boundaries were tangled and sometimes disconnected. The misorientation map

shows the distribution of plastic residual strain in the material. AM materials contained a large amount of plastic strain even after stress relief. The strain was not uniform in the material. Larger grains possessed a higher strain level than smaller grains. The differences in the local plastic strain may result in the variations in the recrystallization kinetics at different locations.

Fig. 3 shows the EBSD mapping of AM 316L SS after HIP and SA. The material exhibited equiaxed coarse grains with high angle grain boundaries and twins. 316L SS is categorized as a low or medium stacking fault energy material. Annealing twins were formed to compensate the energy released from the non-equilibrium microstructure. The material was mostly strain free. However, there were still some unrecrystallized grains with retained plastic strain. It should be noted that the HIP temperature was 1150°C, which is beyond the normal solution annealing temperature for austenitic SSs. So, it is highly possible that the AM parts from different vendors/processes can still possess plastic strain even after high temperature annealing. The existence of these unrecrystallized grains in the solution-annealed AM material makes it critical to evaluate the SCC behavior of the partially-recrystallized bimodal material shown in Table 3.

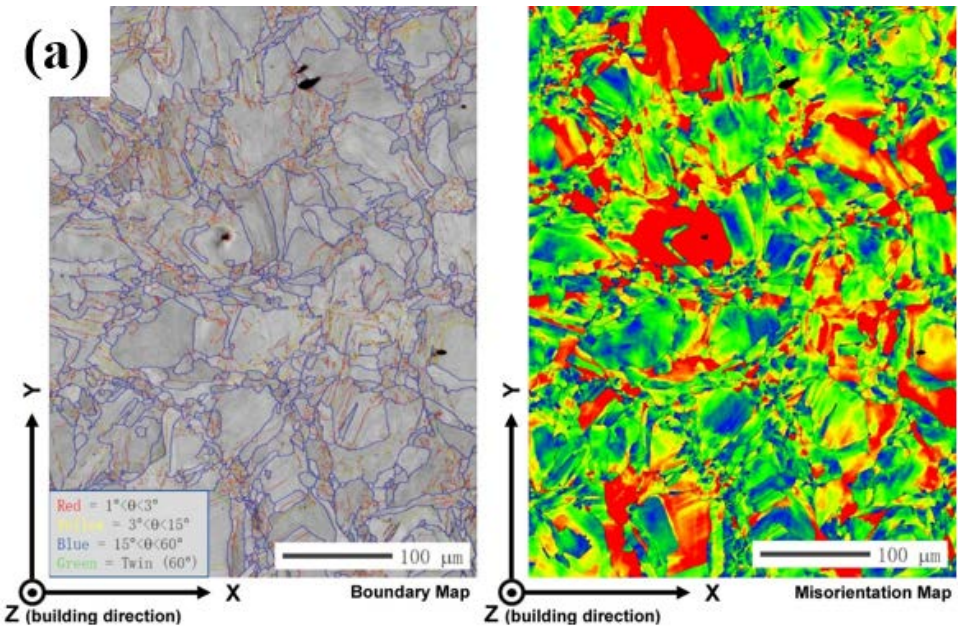

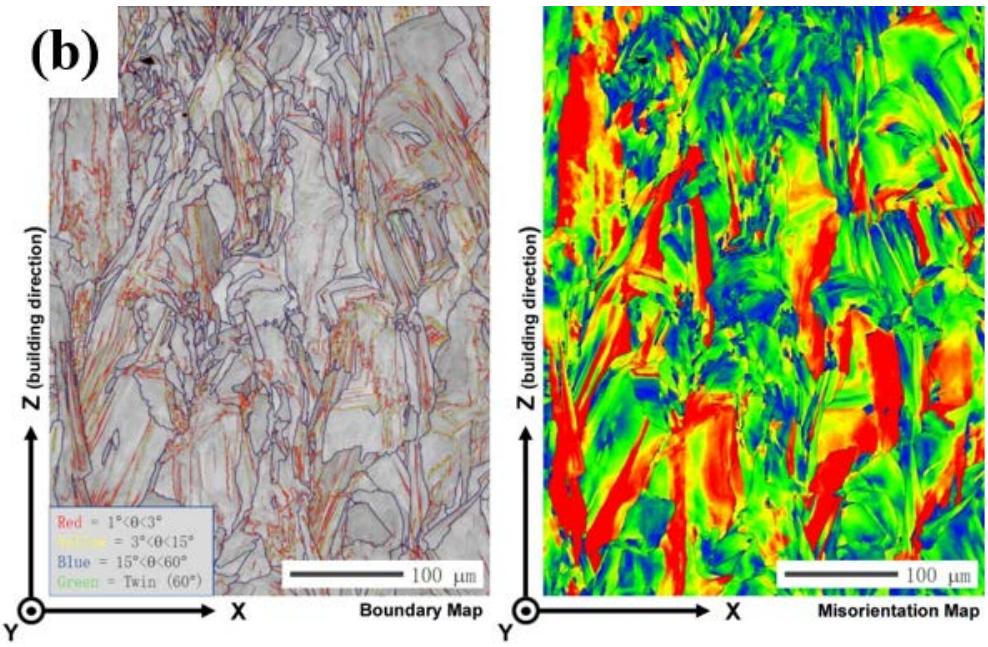

Fig. 2. EBSD boundary map and 10° misorientation map of AM 316L SS: (a) stress relief, cross-section parallel to powder bed; (b) stress relief, cross-section parallel to the material build direction Z.

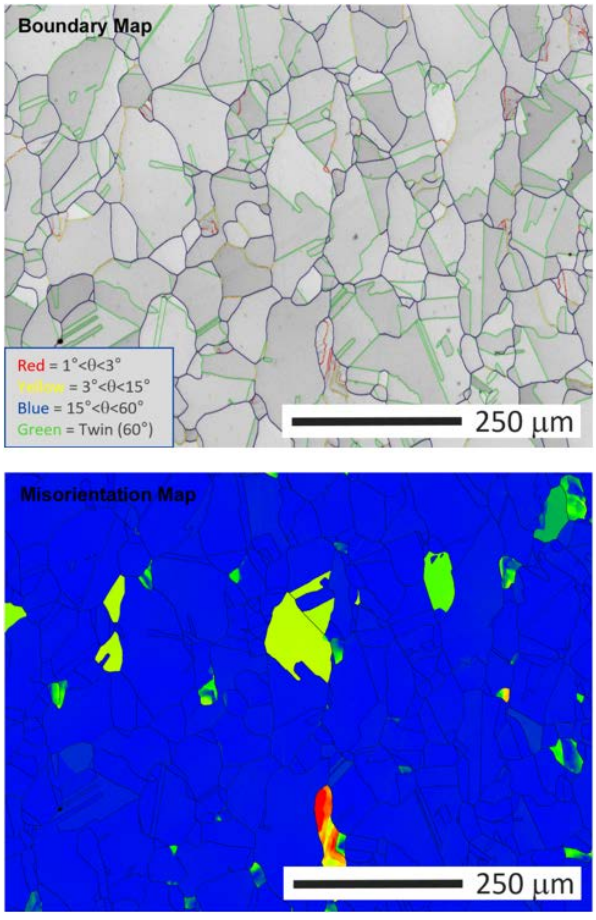

Fig. 3. EBSD boundary map and 10° grain misorientation map of AM 316L stainless steel after HIP+SA.

3.2. Process-to-process, vendor-to-vendor, location-to-location variations

In the world of L-PBF, it is very common to see the same AM 316L SS from different processes and vendors exhibits different macroscopic defects (pores, cracks, etc.) and microstructural features (unrecrystallized grains, precipitates, etc.). Fig. 4 shows the example of the same 316L powder fabricated by two different L-PBF processes. As shown in the figures, Heat #1 exhibits a fully-recrystallized microstructure with equiaxed grain structure. In comparison, Heat #2 contains a large fraction of unrecrystallized grains even though the material was also post heat treated in the same condition above the solution annealing temperature. The solidification microstructure and residual plastic strain from the laser process can significantly impact the final microstructure in the material.

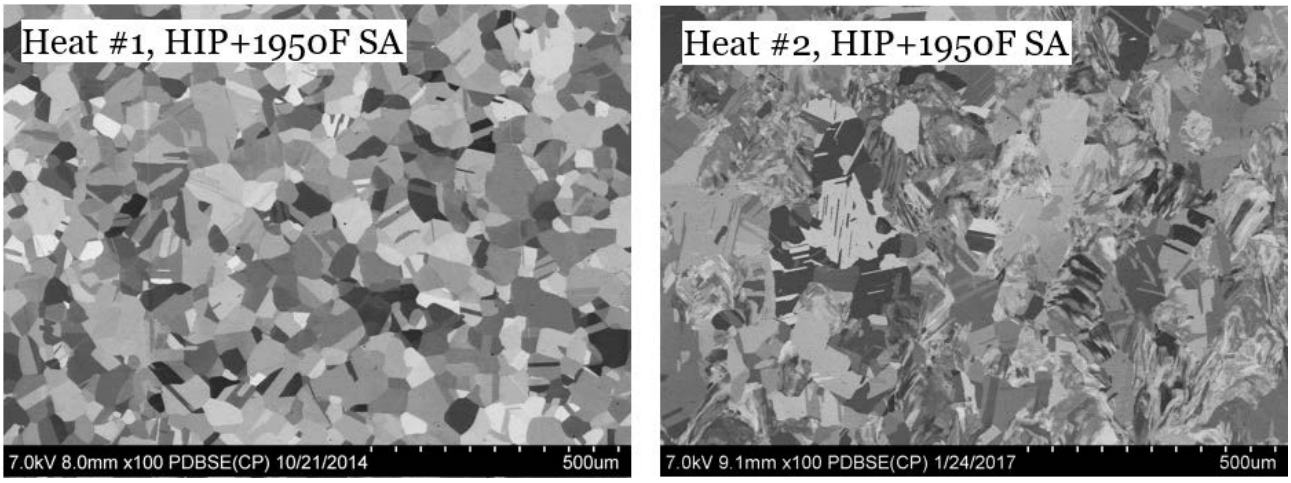

Fig. 4. BSE images of AM 316L stainless steel after the same HIP+SA, processed with different L-PBF parameters.

The AM 316L SS part can also show location-to-location differences in its microstructure. Fig. 5 shows the BSE image of a part produced by L-PBF. The material exhibited microstructural variations due to the difference in thermal history at different locations. Even though the part went through high temperature annealing, the unrecrystallized microstructure was non-uniformly distributed throughout the material. In the center of the specimen, the material was largely unrecrystallized. The material shows a clear melt pool structure.

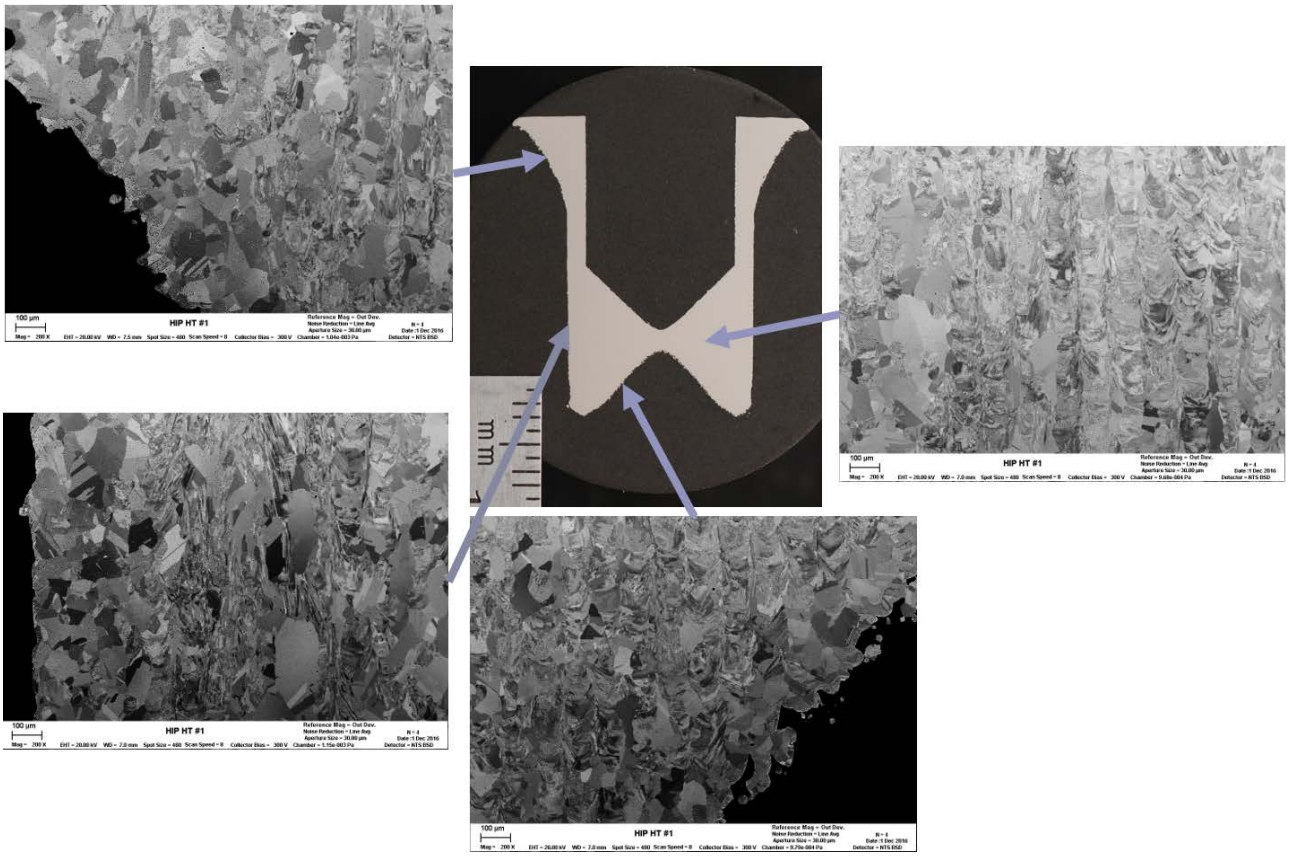

Fig. 5. Microstructural location-to-location differences in an AM 316L stainless steel part after the same HIP+SA

3.3. Subgrain structure and inclusions

AM 316L SS by L-PBF generally shows unique hierarchical structures with fine subgrain features, such as high angle boundary, low angle cellular boundary, dislocation cellular boundary. Element segregation and inclusion precipitation are visible along these boundaries. Fig. 6 shows a typical subgrain structure in AM SS after stress relief heat treatment. Dislocation entanglement creates dislocation cells inside the grain. Cell walls are formed by dislocation tangling and oriented parallel to the thermal gradient from laser solidification. Low angle boundaries are also formed by highly concentrated dislocation clusters. The subgrain dislocation structure is like cold worked stainless steel and oriented primarily towards the build direction.

Nanoscale inclusion particles were also observed in AM 316L SS, as shown in Fig. 7. These inclusion particles were silicon (Si) and manganese (Mn) rich oxides, identified by TEM/EDS. Most particles were formed along columnar boundaries and distributed uniformly in the material. After recrystallization, as shown in Fig. 8, the nanoscale inclusions coarsened and formed larger oxides with the average size around 300 nm.

The nanoscale features in AM 316L SS were expected to serve as sinks for the point defects created by neutron irradiation. This project conducted proton and heavy ion irradiation as well as IASCC evaluation to validate their benefits. In conclusion, we do not see clear irradiation benefit from these features. In fact, the dislocation cellular structure in the stress-relieved AM 316L SS seems to enhance the swelling and IASCC susceptibility.

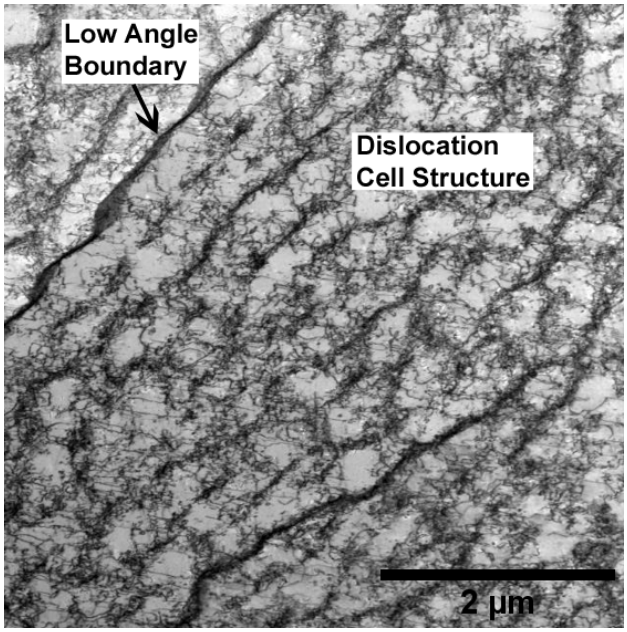

Fig. 6. TEM image of a subgrain dislocation cellular structure and boundary structure in AM 316L stainless steel after stress relief.

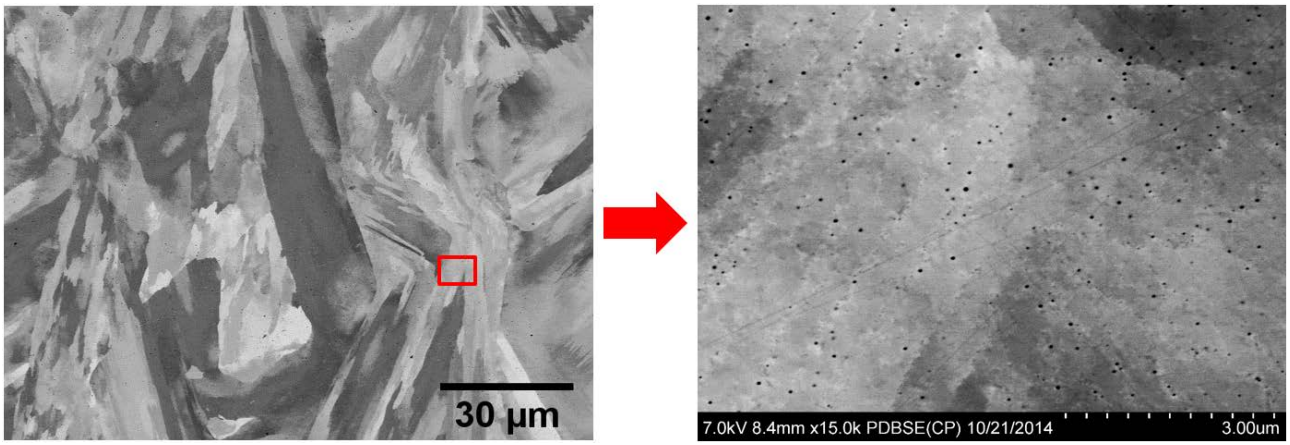

Fig. 7. Nanoscale inclusions in AM 316L stainless steel under as-built or stress-relieved condition

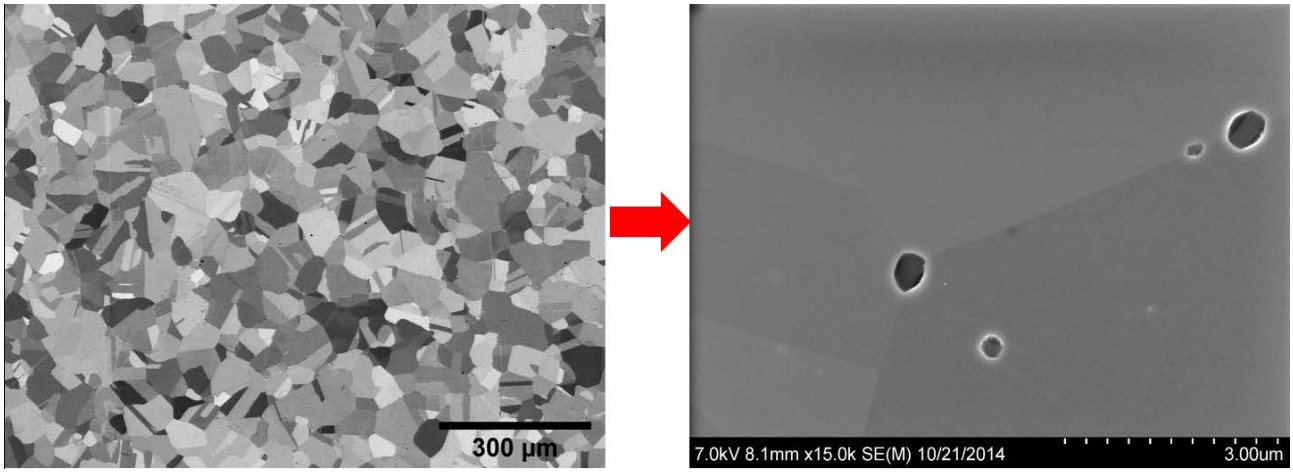

Fig. 8. Coarsened large inclusions in AM 316L stainless steel after high temperature annealing.

4. Tensile Properties

The tensile properties of AM 316L SS and other AM alloys have been widely reported in the literature. The general conclusion is that the tensile properties of most AM alloys are similar to or better than traditional wrought alloys, as long as the AM materials have reasonable quality and material density. Many different heats of AM 316L SS were evaluated in this project. Those materials were fabricated by different vendors and process parameters to understand the variation in tensile properties due to the macro and microstructural differences by the process.

Tensile specimens, with a nominal gage diameter of 0.250 inches, were machined from the horizontally and vertically built specimens, as shown in Fig. 9. The specimens' dimensions and testing followed ASTM E8-16a at room temperature. Specimens were loaded in strain control at a rate of 0.015 in/in/min until a strain of 0.012 was reached. Testing then continued in displacement control at a rate of 0.063 in/min until rupture. Elongation was determined using a gage length of 1.000 inches. Fig. 9 shows specimen orientation relative to the powder bed. The directions were designated by the axes of the coordinate system shown in Fig. 9. "X" and "Y" axes refer to the directions in the plane parallel to the powder bed, while "Z" axis refers to the material build direction.

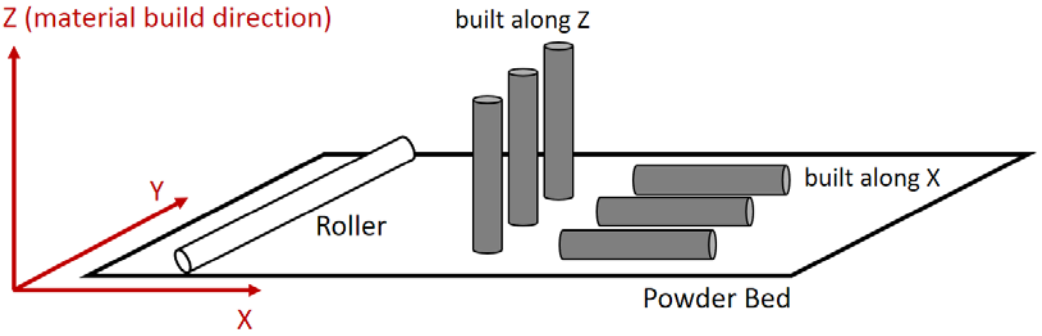

Fig. 9. Tensile specimen orientation relative to powder bed

Three different heats of AM 316L SS were evaluated in this study. Heat #1, Heat #2, and Heat #3 were processed by different vendors on EOS 270, Renishaw AM250, and EOS 280, respectively. The materials were tested under stress relief, or hot isostatically pressed followed by solution annealing, or solution annealing only. Heat #2 was evaluated at both room temperature and 288°C to confirm the temperature effect.

The tensile properties of AM 316L SS heat #1 under stress relief and HIP+SA are shown in Fig. 10, and compared to the values of wrought traditional 316L material. Since AM 316L SS has non-equilibrium anisotropic microstructure under stress relief, the tensile tests were conducted along both the X and Z directions. With stress relief, the material showed higher yield strength (YS) and ultimate tensile strength (UTS) along the X direction than along the Z direction. Compared to the annealed wrought 316L, the stress-relieved AM 316L showed a yield strength more than two times higher as the wrought 316L. The higher strength in AM 316L SS is attributed to its finer microstructure and retained cold work, as shown in previous sections. While stress-relieved AM 316L showed higher strength, it still had a reasonable ductility. The minimum elongation to failure measured along the X direction was still above 40%. It is shown in Fig. 2 that the grain boundary spacing along the X direction was smaller than that along the Z direction, which may contribute to the lower ductility and higher strength along the X direction. The solution annealing heat treatment significantly reduced the yield strength due to recrystallization or annealing of the retained strain.

The tensile properties of AM 316L SS after HIP+SA treatment was slightly higher than the properties of wrought 316L SS.

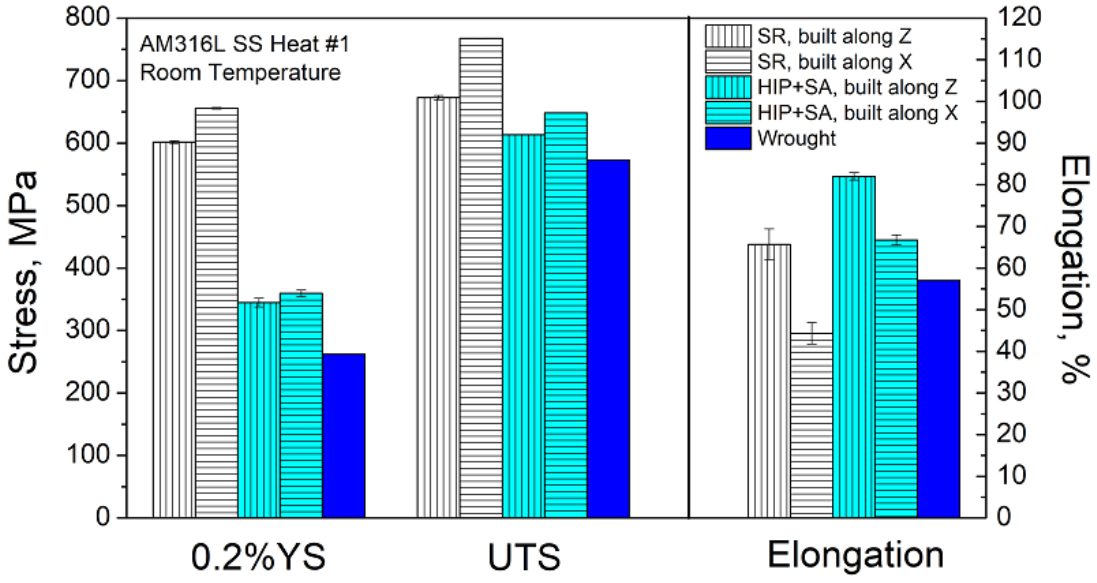

Fig. 10. Tensile properties of AM 316L Heat #1: stress relief vs. HIP+SA

Fig. 11 shows the tensile properties of AM 316L Heat #2 tested at two different temperatures. 288 °C was used to simulate boiling water reactor primary system temperature. The material was fully solution annealed at 1066°C for 1 hour. No HIP was applied to the material so higher porosity was present in this material compared to Heat #1. At room temperature, Heat #2 showed similar yield strength and UTS to Heat #1. The ductility was slightly lower which may be due to its higher porosity. At both room temperature and 288°C, Heat #2 exceeded the tensile performance of its wrought counterpart that was also tested under the same conditions.

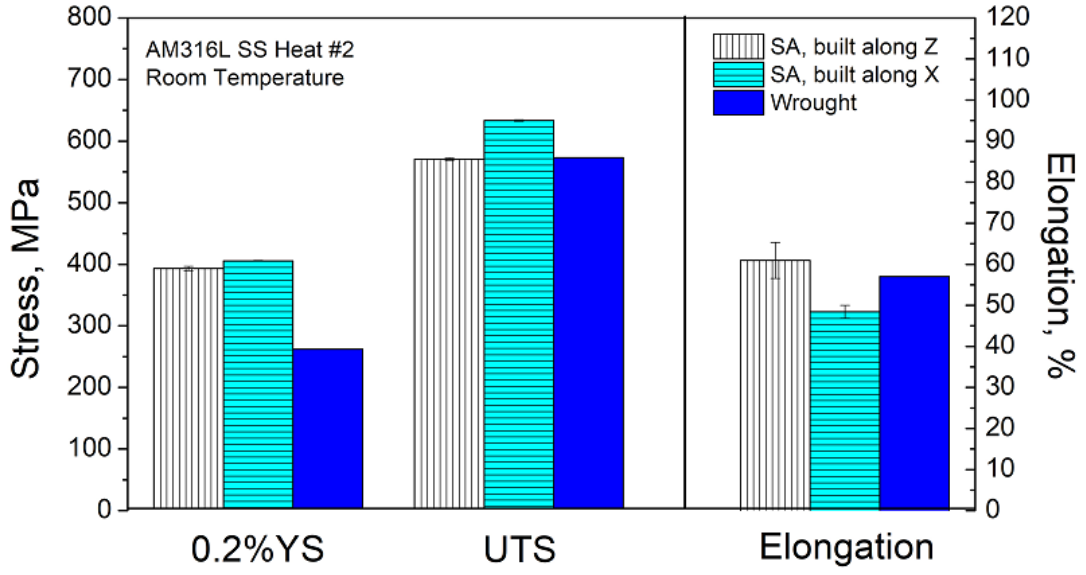

(a) Room Temperature

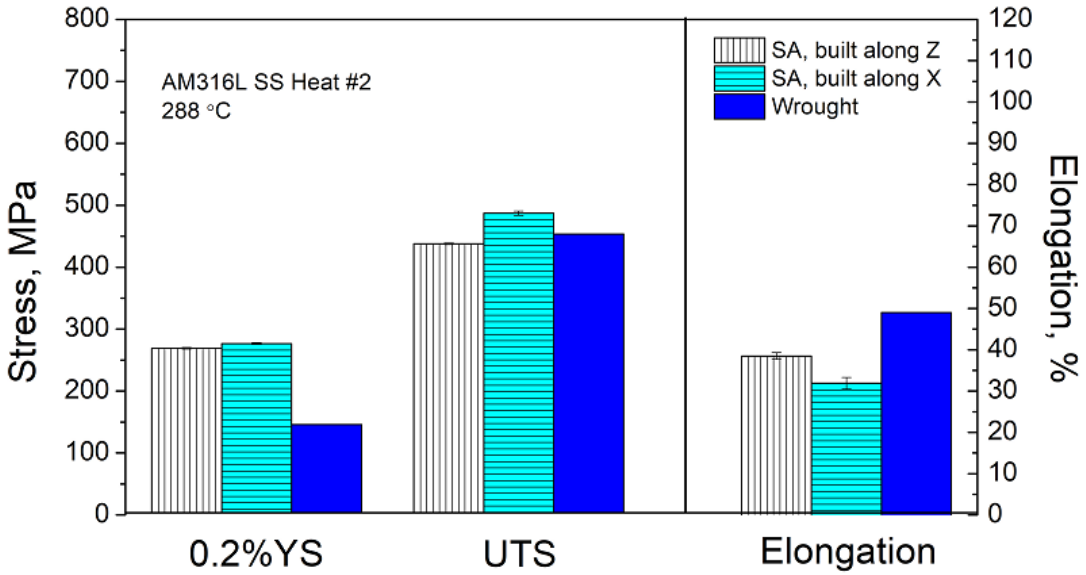

(b) 288°C

Fig. 11. Tensile properties of AM 316L Heat #2 at room temperature and 288 °C

Fig. 12 shows the tensile properties from AM 316L Heat #3 at room temperature. The material shows similar tensile properties to both Heat #1 and Heat #2 under solution annealing treatment. It also exceeded the performance of wrought 316L SS.

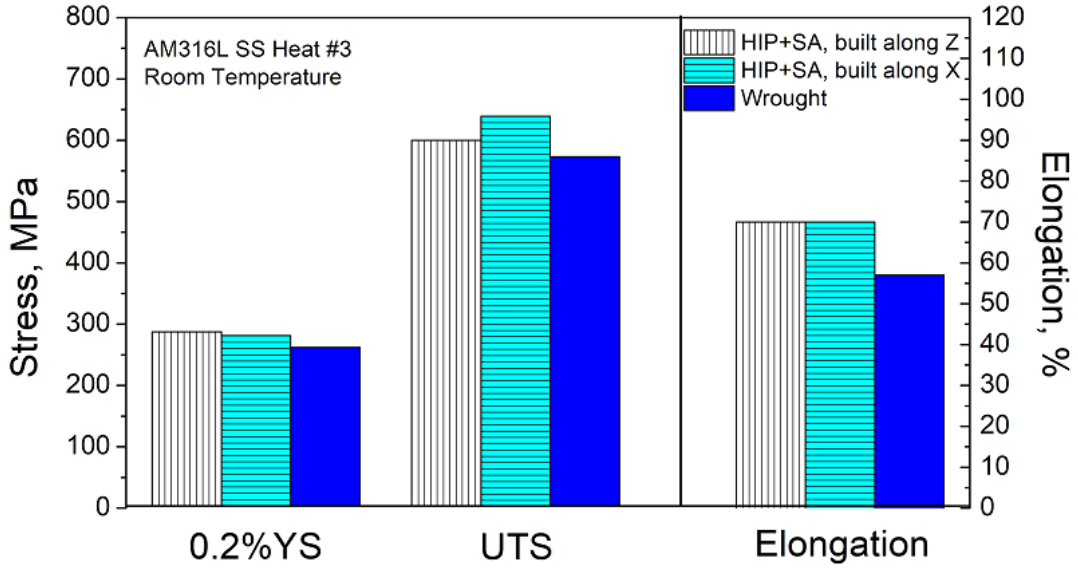

Fig. 12. Tensile properties of AM 316L Heat #3 at room temperature

In summary, this study confirmed that AM 316L SS generally exhibits similar or better tensile properties than its wrought counterpart. If the AM material shows reasonably low porosity, AM 316L SS shows consistently good tensile properties, regardless of the differences of vendors, processes, and even microstructures.

5. Charpy Impact Toughness

Charpy V-notch specimens were machined according to ASTM A370 (10 mm X 10 mm X 55 mm). Because of the anisotropic nature of the AM materials, two different orientations were evaluated for Charpy impact toughness, with the notch either parallel ("horizontal" specimen in Fig. 13) or perpendicular ("vertical" specimen in Fig. 13) to the material build direction. At least three specimens were tested for each orientation at room temperature.

Two different heats of AM 316L SS were evaluated in this study. Heat #1 and Heat #2 were processed by different vendors on EOS 270 and Renishaw AM250, respectively. The materials were tested under stress relief, or hot isostatically pressed followed by solution annealing.

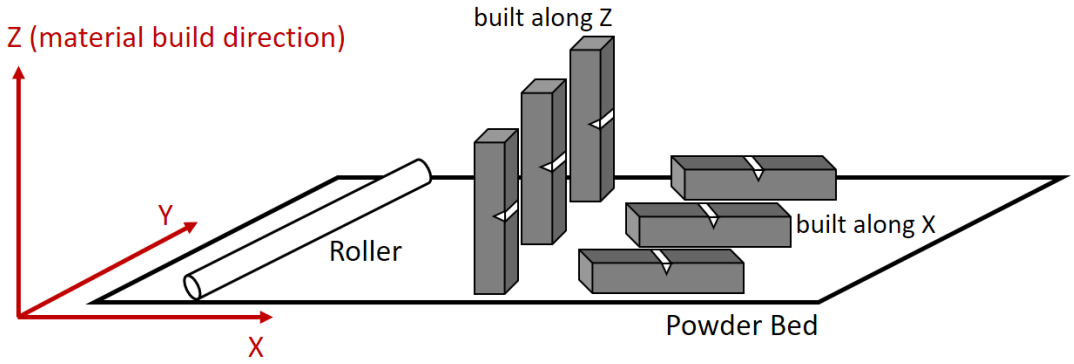

Fig. 13. Charpy impact toughness specimen orientation relative to powder bed

Fig. 14 shows the Charpy impact toughness of AM 316L Heat #1 under stress relief and HIP+SA. The specimen built along Z with X oriented notch showed slightly higher impact toughness than the specimens built along X with Z oriented notch. Overall, both stress-relieved material and HIP+SA material showed similar impact toughness values.

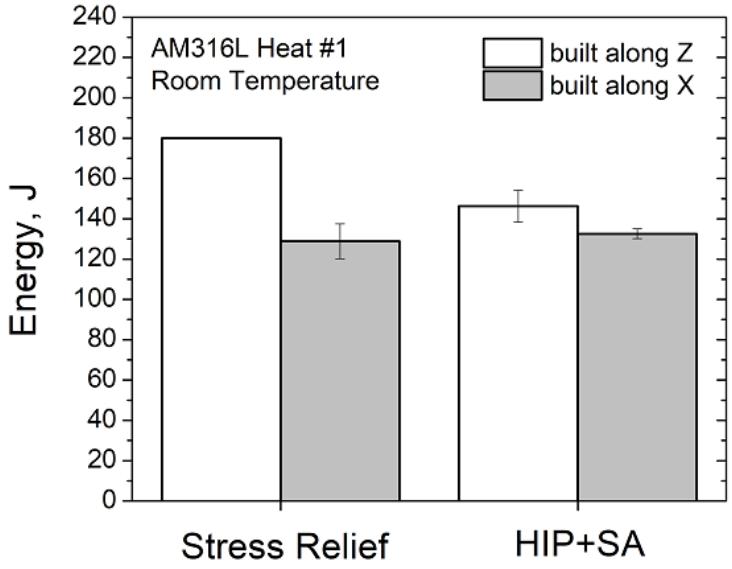

Fig. 14. Charpy impact toughness of AM 316L Heat #1.

Fig. 15 shows the comparison of Charpy impact toughness between Heat #1 and Heat #2 after solution annealing. Both heats performed similarly in the research.

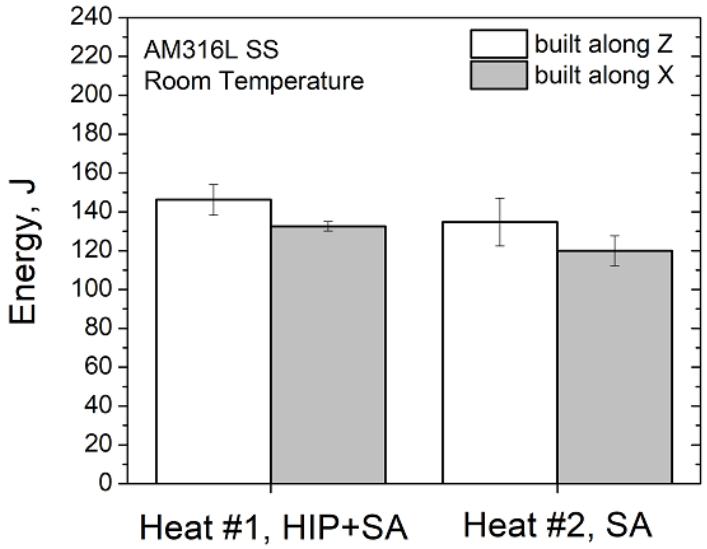

Fig. 15. Comparison in Charpy impact toughness between Heat #1 and Heat #2. Both heats were tested under solution annealing condition.

Fig. 16 shows Charpy impact toughness data of AM 316L SS used in this study, compared to data obtained from the literature for AM 316L SS [26], PM-HIP 316L SS [27-29], and wrought 316L SS [30-33]. Among these materials, AM SSs and wrought SSs had comparable grain size. PM-HIP SSs generally possessed a slightly smaller grain size. AM 316L SS was tested in two different orientations, as described before, which showed a similar Charpy impact energy of about 130-150 J at room temperature, consistent with the equiaxed grain structures from full recrystallization [18, 19, 34]. These values were also similar to literature data [26]. By comparison, the wrought products from forging generally had a higher impact energy under the same testing conditions. The reported values for wrought 316L SS were generally above 200 J, with the highest value being 350 J. PM-HIP 316L SS were also formed from alloy powder, and generally exhibited an impact energy of 200-250 J. A systematic study by Cooper et al. [29] suggested that the impact toughness of PM-HIP 316L SS decreased as the oxygen level increased. As oxygen concentration increased up to 190 ppm, the impact energy exponentially decreased to ~150 J. No further decline in impact toughness was observed for oxygen values above 200 ppm. In Fig. 16, the wrought material with a toughness of 335 J contained only 23 ppm oxygen.

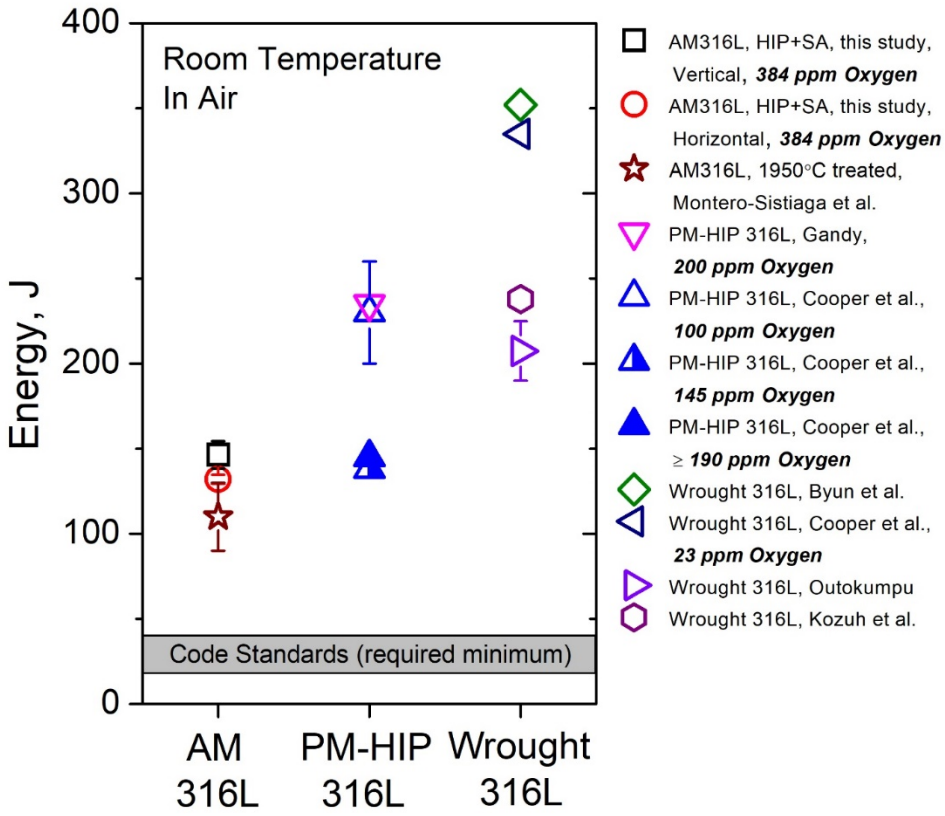

Fig. 16. A comparison of Charpy impact toughness values at room temperature between AM 316L SS, PM-HIP 316L SS, and wrought 316L SS. Data shown were obtained from solution-annealed materials with coarse grain structures. AM 316L SS in this study were evaluated in two orientations. Other data were obtained from the literature, including L-PBF AM 316L (Montero-Sistiaga, et al. [26]), PM-HIP 316L (Gandy [27], Cooper et al. [28, 29]), wrought 316L (Byun et al.[30], Cooper et al. [29], Outokumpu [31], Kozuh et al. [32]). The code required minimums are from American Institute of Steel Construction [33]. The unit of ppm is based on weight, mg/kg.

Fig. 17 shows the fractography of the AM 316L SS Charpy specimen, which consistently showed the complete fracture in the Charpy test. Similar to the PM-HIP 316L SS [28], AM 316L SS produced a single fragment with signs of plastic deformation. High resolution SEM showed that AM SS exhibited typical ductile fracture like wrought SSs. A large area of the fracture surface was examined and, in most cases, oxide inclusions were found in the dimples, which suggested that the presence of oxides served as initiation sites for microvoid formation and may have led to the reduced toughness. EDS mapping confirmed the oxide chemistry and the inclusion particles were all rich in Si and Mn. Some oxide particles also contained molybdenum (Mo).

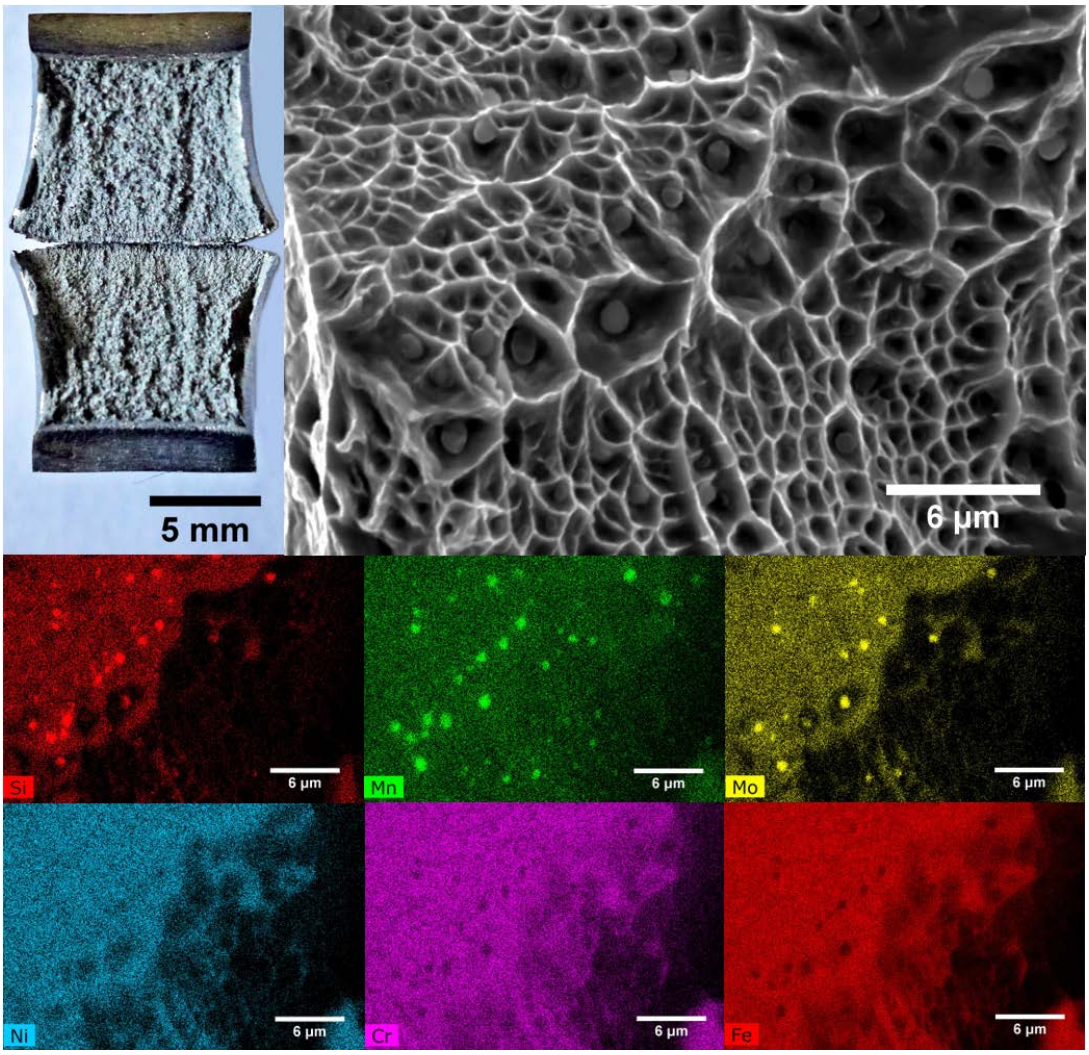

Fig. 17. SEM image and EDS map of the Charpy impact fracture surface. The spherical particles were oxides. An oxygen map is not included in this figure.

It is well-known that oxygen can influence the impact toughness of cast or welded metals [35-37]. Modern casting and forging techniques have successfully minimized oxygen in the final product. Compared to steelmaking, there is a much higher chance of oxygen incorporation during AM and HIP-PM. For austenitic SS, PM-HIP typically yield an oxygen level at 100-200 ppm, an order of magnitude greater than forging and casting [29]. Powder oxidation, from either gas atomization or handling/storage, was considered to be the main source of oxygen in PM-HIP products [29]. Cooper et al. [29] reported a direct relationship between microporosity, non-metallic oxide inclusions (100-500nm) and impact toughness in PM-HIP 316L SS. As the oxide inclusions increased above 0.3 vol%, the impact toughness decreased to ≤150 J. A similar relationship between brittle oxide inclusions and impact toughness was also reported in different alloys and welds [37, 38].

AM process utilizes the same powder manufacturing process as PM-HIP. Oxygen in powder is nearly impossible to eliminate. The reported oxygen levels in AM 316L SS were generally twice those found in PM-HIP products (see Fig. 16) [39, 40], probably because L-PBF is performed in argon gas instead of vacuum. AM 316L SS by L-PBF had oxide dispersions with similar size and volume fraction as its PM-HIP counterpart [29]. Following Cooper et al.'s theory [29], the reduced impact

toughness of AM 316L SS at 100-150 J can be well explained by the microporosity created by brittle oxide inclusions (0.23 vol%, Fig. 8) and lack-of-fusion defects (0.08 vol%, Table 4).

In summary, in this study, different heats of AM 316L SS also showed similar Charpy impact toughness. However, AM 316L SS generally exhibited lower impact toughness than its wrought counterpart. The intragranular oxide inclusions promoted early microvoid formation which reduced the impact toughness relative to the PM-HIP and wrought materials of comparable grain size. The reduced impact toughness can be explained by the elevated oxygen level in the material and numerous oxide particles. Therefore, attention is needed if a manufacturer decides to reuse the recycled powder to save cost.

6. Stress Corrosion Crack Growth Behavior

6.1. Experiment

Compact tension (CT) specimens with 5% side grooves on each side were machined from the AM 316L SS blocks after all the heat treatments. The specimen's dimensions followed ASTM E647 [41] with a thickness of 12.7 mm and a width of 25.4 mm. Fig. 18 shows the specimen orientation relative to the powder bed of the EOS system. The directions were designated by the axes of the coordinate system shown in the figure. "X" and "Y" axes refer to the directions in the plane parallel to the powder bed, while "Z" axis refers to the material build direction. In a crack growth test, the notation "Z-X" means that the loading is in the "Z" direction and the crack advances in the "X" direction.

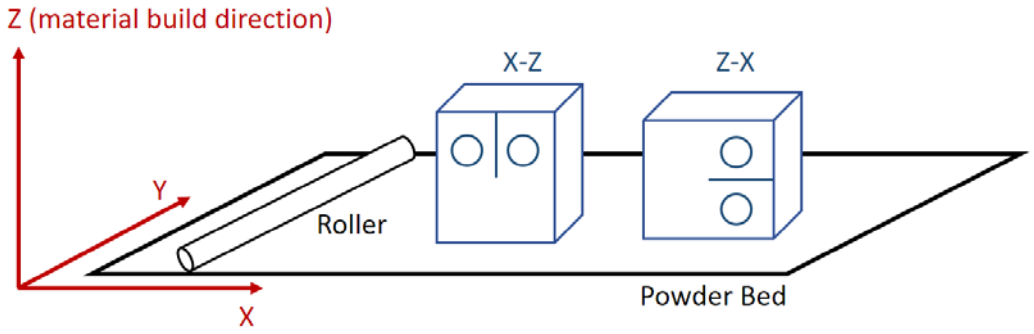

Fig. 18. Schematic of the orientations of compact tension specimens relative to powder bed. "X" and "Y" axes refer to the directions in the plane parallel to the powder bed, while "Z" axis refers to the material build direction. In a crack growth test, the notation "Z-X" means that the loading is in the "Z" direction and the crack advances in the "X" direction.

The validity and accuracy of the SCC growth rate measurement capabilities have been proven by a Round Robin organized by the Swedish Nuclear Power Inspectorate and Electric Power Research Institute in the 1990s [42] and adopted by many labs around the world [43-50]. As shown in Fig. 19, the CT specimens were instrumented with platinum (Pt) current and potential leads for direct current potential drop (DCPD) measurements, which provides a resolution of ~1 μm in crack length or ~10^{-9} mm/s in crack growth rate. The 2.5A DC current flowing through the specimen was supplied by an Agilent Technologies 6611C DC power supply, and reversed about once per second by a solid-state relay bridge to reduce the measurement errors associated with thermocouple effects. An Agilent Technologies multiplexer and digital voltmeter were used to measure the DCPD potentials, along with temperature, inlet and outlet conductivities, corrosion potentials, and other signals. DCPD active potential leads were positioned at the front face of the specimen to measure the voltage change during crack propagation. To compensate the voltage drift caused by the changes in metal resistivity, DCPD reference potential leads were attached on the back-face of the specimen to monitor the resistivity drift without any influence from the growing crack. Computer software controlled the current reversal, data acquisition, data averaging, and the crack length calculation, and maintained a constant *K* by automatically lowering the load as the crack advanced. [20, 21] The specimen was electrically insulated from the loading rig by zirconia sleeves and washers. Extensive finite element modelling (FEM) and experimental validation using bench marking were used in the early development of

DCPD algorithms at GE. FEM simulation determined the current distribution and the relationship of DCPD potential vs. crack length for both active and reference potential leads. The actual crack length in the test is obtained based on the pre-determined relationship of DCPD ratio vs crack length by FEM simulation. This DCPD ratio vs. crack length relationship strongly depends on the locations of the probes, but not on the material type, temperature, or specimen size, if the specimen size and probe location remain in proportion. Extensive averaging of data was used to improve the measurement resolution. DCPD is very accurate if the crack is straight, e.g. during fatigue pre-cracking in air, but errors can develop during testing in hot water if the crack front becomes uneven or if contact occurs on the wake of the crack during unloading. In these cases, DCPD tends to underestimate the crack length, which leads to a rising K during the test. An anticipatory crack length correction of 1.5X was used during the test to ensure little or no rise in K during the exposure period. The final crack growth rate and *K* was corrected based on the post-test fractography.

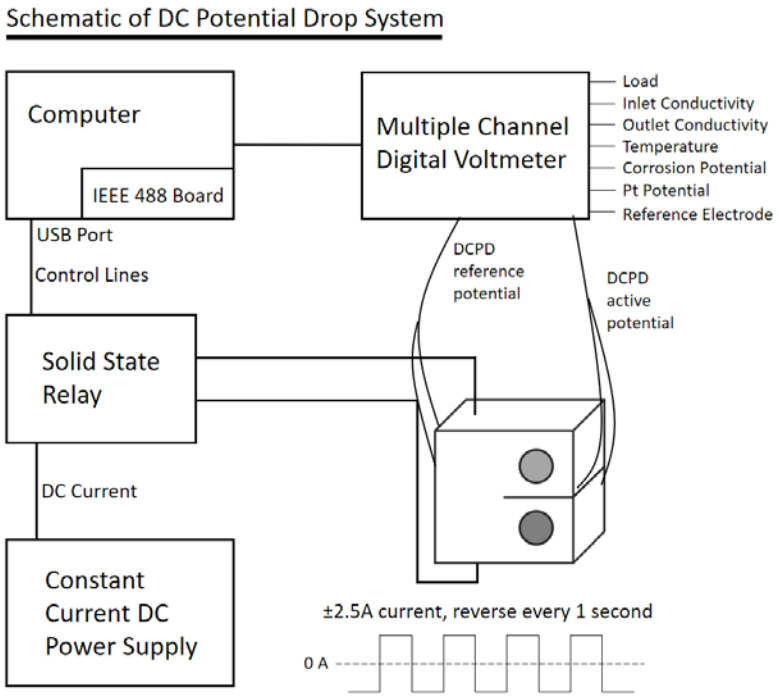

Fig. 19. Schematic of DC potential drop system used in this study for measuring crack growth rate

SCC tests were conducted in simulated boiling water reactor (BWR) environment at 288°C. Fig. 20 shows the closed-loop testing system. The water purity was maintained by the recirculation design with a demineralizer to purify the outlet water from the autoclave back to 0.055 μS/cm (or 18.2 MΩ-cm) at room temperature. The flow rate was around 150 mL/min in the 4-litre autoclave. The autoclave was maintained at a constant pressure of 103.4 bar throughout the test. The tare load on the specimen caused by the pressure acting on the pull rod was factored in the load control. The study was conducted in both high corrosion potential NWC (2 ppm dissolved oxygen or DO) and low corrosion potential HWC (63 ppb dissolved hydrogen or DH). These values were maintained by continuously bubbling a mixture of 5% O_2-95% argon, or a mixture of 4% H_2-96% argon in the glass water column at room temperature. The dissolved oxygen and hydrogen content were not

continuously monitored in the test. However, these values were verified by the oxygen and hydrogen analyzers earlier and backed up by 35+ years of testing experience using similar testing systems. The free electrode potentials of the AM 316L SS specimen (red dashed line in Figure 21) and a Pt coupon (magenta dotted line in Figure 21) were continuously monitored relative to a zirconia membrane Cu/Cu_2O reference electrode [51].

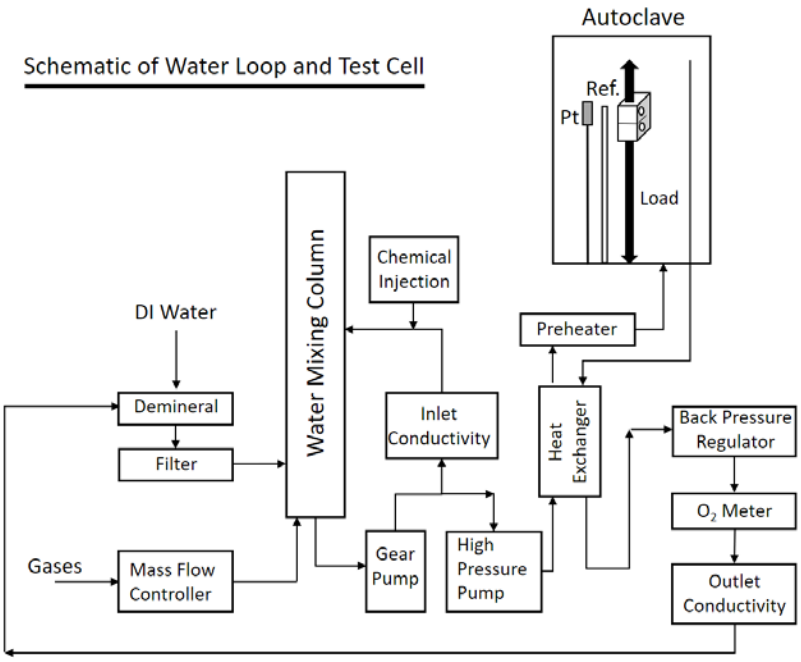

Fig. 20. Schematic of high temperature water loop and testing autoclave setup.

Fatigue pre-cracking in air was performed at the beginning of each test at ~1 Hz and an increasing load ratio (K_{min}/K_{max}) R = 0.2, 0.4, and 0.6, which helps developing a uniform SCC crack front. Subsequent steps in high temperature water to transition the crack to a stress corrosion crack were performed by gradually decreasing the frequency to 0.001 Hz, then by introducing a hold time of 9000s hold time at K_{max}, before changing to constant K condition with no load cycling. The importance of the transitioning procedure for SCC growth rate testing has been well documented [42-44, 48]. All SCC tests in this study were at constant K with no cyclic load. Fig. 21 shows an example of the crack length (blue line) vs. time. Two CT specimen's repeats were usually conducted for each test condition. Some conditions were repeated 3-4 times. The reported crack growth rate in this report is the average value of the repeat measurements. The data scattering for the same condition was usually within a factor of 2.

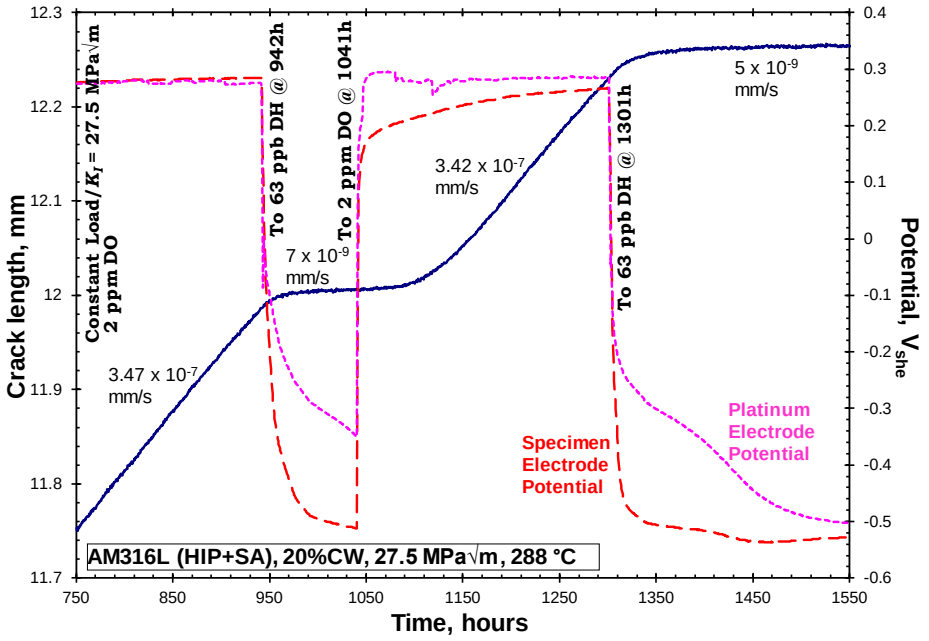

Fig. 21. Crack length vs time for AM 316L SS (HIP+SA) with 20%CW at 27.5 MPa√m. Two repeats were conducted for each testing condition. Some conditions may have three or more repeats.

6.2. SCC growth on the stress-relieved AM 316L SS with no additional cold work

Since the stress-relieved AM 316L SS exhibited an anisotropic microstructure, the effect of the crack orientation was critical in evaluating SCC, especially for the cracks growing in a complex microstructure created by AM. Fig. 22 shows the SCC growth rate of the stress-relieved AM 316L SS along X-Z and Z-X orientations at a constant K=27.5 MPa√m in both oxidizing NWC and reducing HWC. The Z direction (material build direction) showed a higher crack growth rate than the X direction or the wrought material. The differences were more than a factor of two (1.2×10^{-7} mm/s vs 5×10^{-8} mm/s in 2 ppm DO). The crack growth rate in the Z-X orientation was similar to the wrought 316L SS, although AM SS contained a higher plastic strain. The slower crack along Z-X orientation may be due to the difficult crack path cutting through the vertically-oriented and closely-spaced columnar grains. For the cracks that passed through the columnar grains, they were more tortuous and encountered grain boundaries more frequently than those propagating in the X-Z orientation. In all materials, HWC significantly suppressed the crack growth rate by about two orders of magnitude.

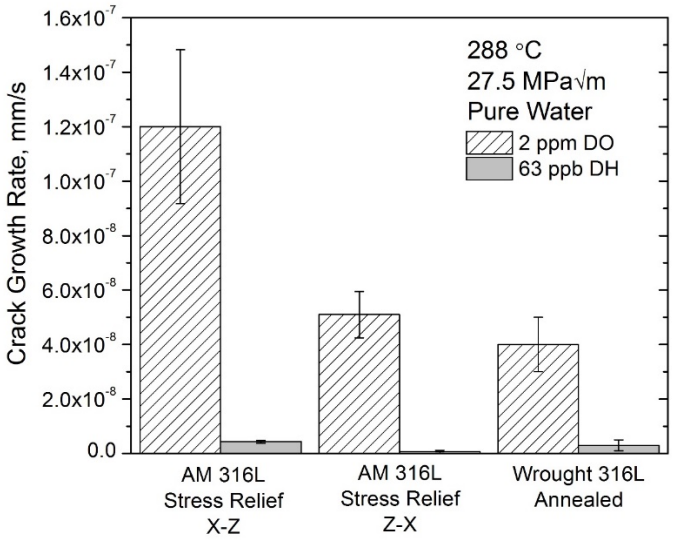

Fig. 22. SCC growth rate of AM 316L SS (stress-relieved with no additional cold work) and wrought 316L SS in NWC (2 ppm DO) and HWC (63 ppb DH) conditions.

Fig. 23 shows the crack in cross-section after testing. For the X-Z oriented cracks in Fig. 23a, the crack path was straight along the elongated grains. Secondary cracks paralleled the main crack. However, in Fig. 23b, the Z-X oriented crack was heavily branched and tended to grow out of plane. As *K* decreased, the crack turned 90 degrees and followed the Z direction, which was clearly the preferred path in the stress-relieved material. This represents the material build direction, which can be a concern for AM components with a complex geometry where the stress and strain fields are complex. DCPD can accurately predict the average crack depth in plane. However, when the crack grows 90° out of plane, the DCPD signal is less sensitive. Therefore, the actual crack extension on Z-X specimen was longer than the reported value in Fig. 22. Stress-relieved AM 316L SS showed higher SCC susceptibility than wrought material. The mixed boundary structure in AM SS does not really improve SCC resistance.

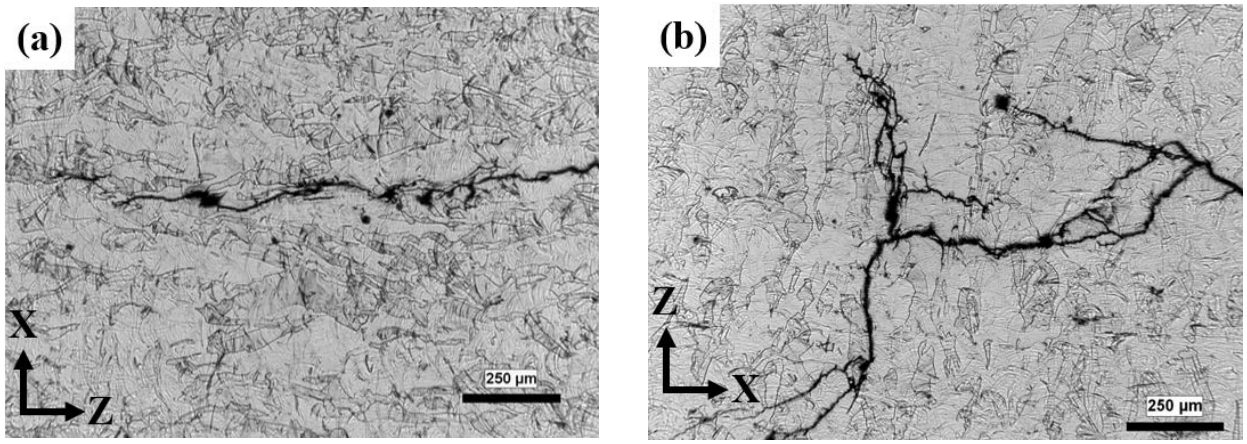

Fig. 23. Optical images of the crack path in the etched microstructure of stress-relieved AM 316L SS: (a) tested in the X-Z orientation; (b) tested in the Z-X orientation. The samples were etched by Kalling reagent.

Fig. 24 (left) shows the EBSD map of the crack front (X-Z orientation) in the non-CW AM 316L SS. The crystallographic texture map (inverse pole figure) and boundary map show that part of the crack followed the high angle boundary between two grains. Although the boundaries were tortuous in the material, the boundaries of the elongated grains in the material build direction formed an easier crack path. The high angle boundaries were not the only path for SCC. The left and right portions of the crack did not follow high angle boundaries. Instead, the crack followed sub-grain structures, which could be the low angle columnar boundaries or dislocation cells. Kernel average misorientation (KAM) maps provide direct evidence of localized orientation changes such as dislocation cells, columnar structures and sub-boundaries, all of which are associated with the strain distribution. These sub-grain deformation structures were also distributed in the material build direction. The alignment of these structures and the strain distribution served as the main driving force for the crack to follow the build direction.

After 20% cold work was applied to the material (Fig. 24, right), the sub-grain deformation structures were enhanced and further connected along the material build direction. The grains were deformed in the forging plane. The crack was straight without a tendency to follow any preferred preexisting boundaries. Corrosion products were observed inside the crack. Heavily cold-worked austenitic stainless steel were reported to show elevated SCC growth rates in HWC [46]. The kinetics of SCC is generally driven by the dissolution/repassivation rate of the metal at the crack tip and by the crack tip strain rate [52]. The corrosion kinetics [53] and the crack tip strain rate [54-56] could both be enhanced by cold work and lead to higher SCC growth rate. In a cold-worked material, the strain distribution in the microstructure affects SCC susceptibility in difference orientations [57, 58]. When forging in the X direction, the plastic strain was enhanced and distributed along the Z direction, which may also lead to higher SCC susceptibility and no response to HWC for AM 316L SS in the X-Z orientation.

Therefore, for AM 316L SS, the cracking of the stress-relieved material showed a mixed contribution from low and high angle boundaries of columnar structures and dendrites, with some intragranular morphology. The presence of subgrain deformation structures and the distribution of cold work associated to these structures served as the driving force for SCC.

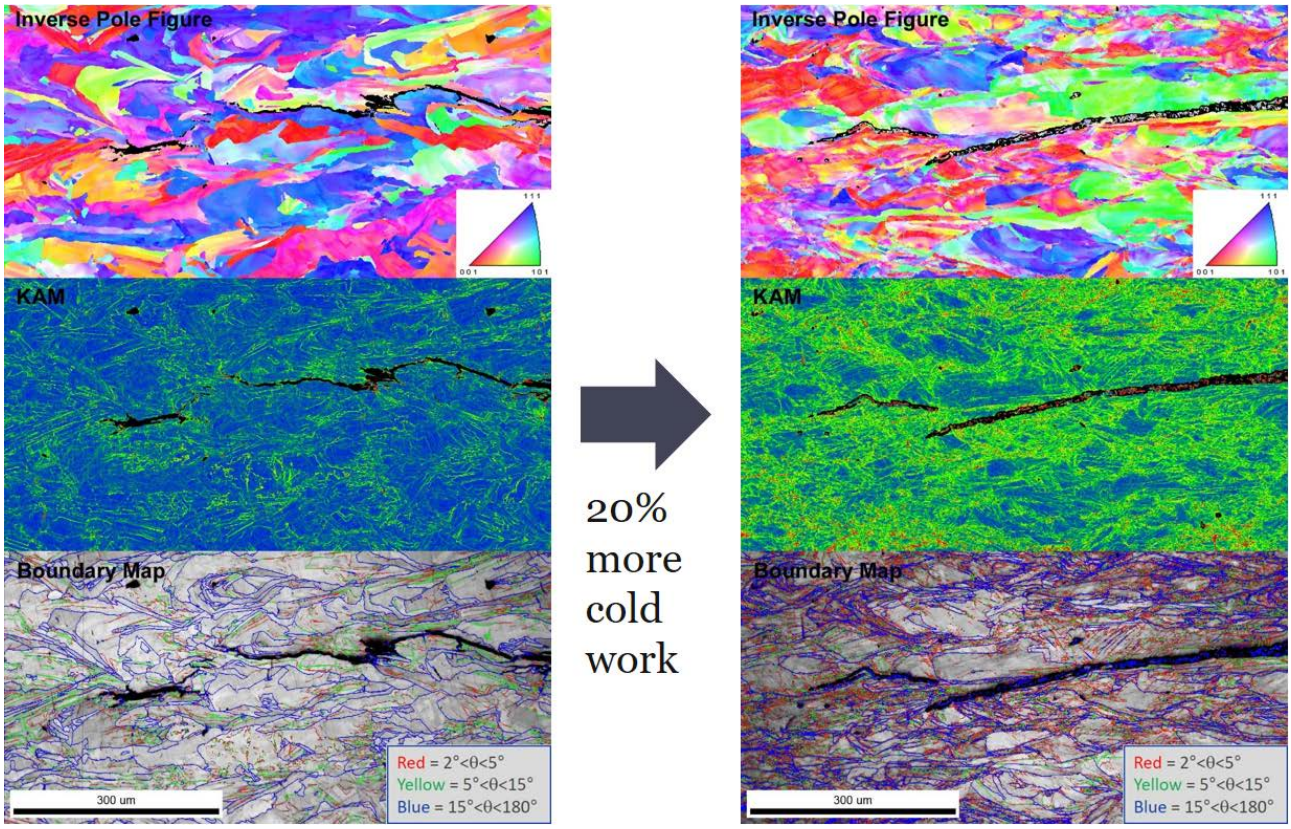

Fig. 24. EBSD mapping of a stress corrosion crack in the stress-relieved AM 316L SS tested in the X-Z orientation. The figure includes inverse pole figure map, kernel average misorientation map, and grain boundary map. Left: stress-relieved with no additional cold work; Right: stress-relieved with 20% applied cold work along Z.

6.3. SCC growth on the AM 316L SS with HIP and SA

After HIP and SA, AM 316L SS exhibited the same equiaxed coarse grain structure as the wrought material. Fig. 25 shows the SCC growth rates of the AM 316L SS after HIP+SA with and without 20%CW in both NWC and HWC. With fully-recrystallized grains, AM 316L SS showed similar SCC growth rate as its wrought counterpart in both the annealed and 20%CW conditions. The SCC growth rate of 20%CW AM material in NWC was about 3.5×10^{-7} mm/s. HWC significantly reduced SCC growth rate to 5×10^{-9} mm/s for the 20%CW material and $<1\times10^{-9}$ mm/s for the annealed material. With fully-recrystallized equiaxed grains, low porosity, reasonable SCC growth rate and good response to HWC, it is reasonable to suggest that a proper HIP and SA treatment is preferred for AM 316L SS used in nuclear service. Fig. 26 shows the crack path in the 20%CW AM 316L SS (HIP+SA), which exhibited intergranular SCC like its wrought counterpart. Based on SCC crack growth behavior, HIP and high temperature SA are recommended for nuclear AM part.

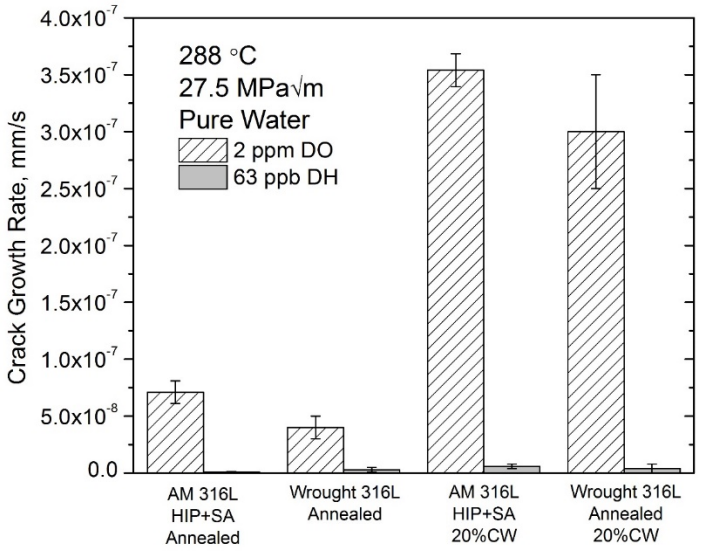

Fig. 25. SCC growth rate of AM 316L SS (HIP+SA) and wrought 316L SS in NWC (2 ppm DO) and HWC (63 ppb DH) conditions.

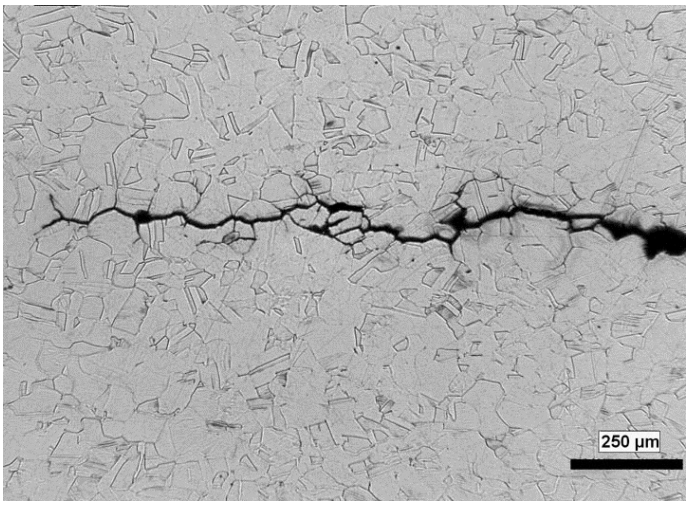

Fig. 26. Optical images of the crack path in the etched microstructure of AM 316L SS (HIP+SA) with additional 20% cold work. The samples were etched by Kalling reagent.

6.4. Effects of the unrecrystallized grains in the high temperature annealed AM 316L SS

As shown in Figs. 4 and 5, unrecrystallized grains are expected in AM parts even when the materials have been solution heat-treated at high temperatures. The volume fraction of unrecrystallized grains depends the laser parameters, the heat treatment, and even the location in the component. The effects of unrecrystallized grains on the cracking and fracture properties of AM metals are rarely studied. The bimodal grain structure in AM 316L SS was created by partial recrystallization (Treatment 4 at 955°C) to assess how unrecrystallized grains impact the SCC

behavior of AM 316L SS. After Treatment 4, 30% material was recrystallized. The dislocation density in the unrecrystallized grains was also expected to be lower than the stress-relieved material (650°C treated), as reported elsewhere [59]. Fig. 27 shows the partially-recrystallized microstructure of the bimodal AM 316L SS. In the recrystallized grains, the strain was fully removed, and many annealing twins formed. The unrecrystallized area showed the same dendritic/columnar structure as the stress-relieved material.

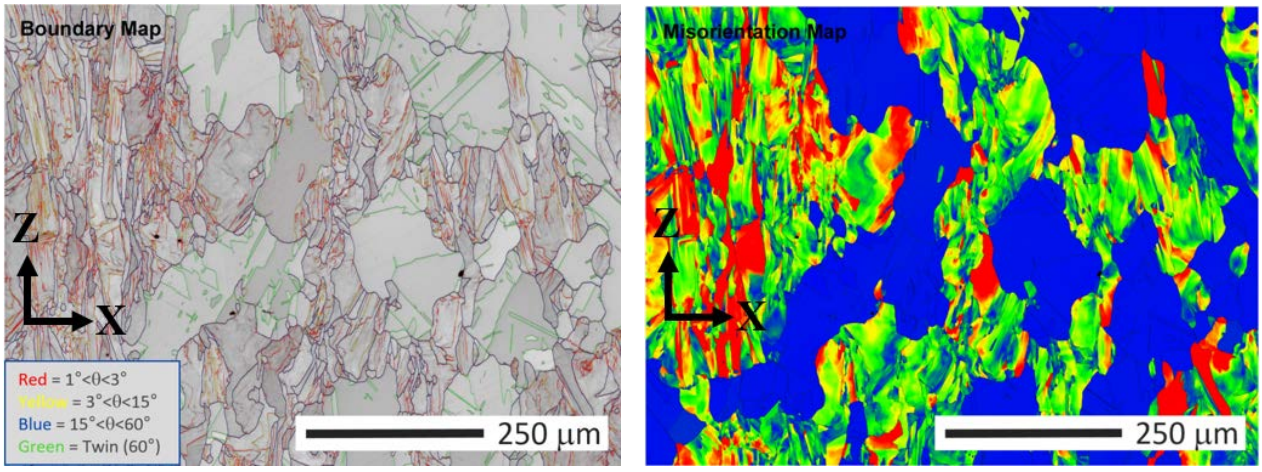

Fig. 27. EBSD grain boundary map and 10° grain misorientation map of the bimodal microstructure of the AM 316L SS that was partially-recrystallized at 955°C

Fig. 28 shows a comparison of SCC growth rates in NWC and HWC for unrecrystallized vs. partially-recrystallized vs. fully-recrystallized AM 316L SS. The materials were all tested in the X-Z orientation without forging. The partially-recrystallized material, despite possessing 70% unrecrystallized microstructure, showed a similar SCC response in NWC and HWC as the fully-recrystallized material. After high temperature annealing, the retained unrecrystallized grains may not impact the overall SCC behavior of AM 316L SS. The similar SCC behavior of the partially-recrystallized and fully-recrystallized materials may be attributed to the lower dislocation density in the material after high temperature annealing [59]. The mix of unrecrystallized and fully-recrystallized grains may also inhibit cracking. This observation again confirmed the deformation structures played a critical role in the SCC susceptibility of AM 316L SS. Further investigation is needed. Based on these results, it may be concluded that some unrecrystallized grains in the annealed AM parts are not detrimental to its SCC resistance if the parts are annealed at high temperature. Annealing treatment at temperatures higher than the stress relief help reduce the SCC growth rate on AM 316L SS.

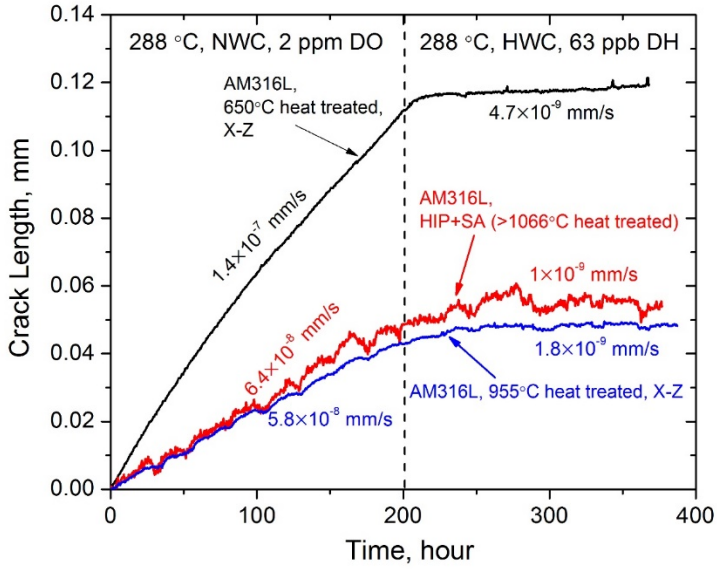

Fig. 28. Comparison of SCC growth behavior of unrecrystallized (650°C stress-relieved), partially-recrystallized (955°C heat-treated), and fully-recrystallized (HIP+SA) AM 316L SS. All materials were tested in the X-Z orientation with no additional cold work.

6.5. Effects of the porosity of AM 316L SS on SCC growth behavior

HIP is generally applied on AM parts to decrease porosity. However, as-built AM SS parts by L-PBF generally have low porosity (<0.5%). HIP does not significantly reduce the porosity and defect size. To evaluate the effects of slightly increased porosity and defect size on SCC growth rates, a high-porosity AM 316L SS was evaluated. This is important because porosity is always present in AM parts, and also variable within a part or from part to part. Eliminating the HIP process reduces cost and accelerates the deployment in the field. Fig. 29 shows the comparison of porosity, defect size, and grain structure in the high-porosity material from a different vendor vs. the low-porosity material after HIP+SA. Although they had different porosity and defect size, they both showed similar fully-recrystallized grains after heat treatments. Fig. 30 shows the SCC growth rates of the two materials in NWC and HWC. The high-porosity heat exhibited a 40% higher crack growth rate than the low-porosity heat in NWC. In HWC, their difference was more significant, close to one order of magnitude. This result suggests that an increase in porosity and pore size in AM 316L SS enhances the SCC growth rate in high temperature water. Further work is needed to establish a correlation between porosity and SCC growth rate, and is necessary to define quality specifications and assess risk for AM components.

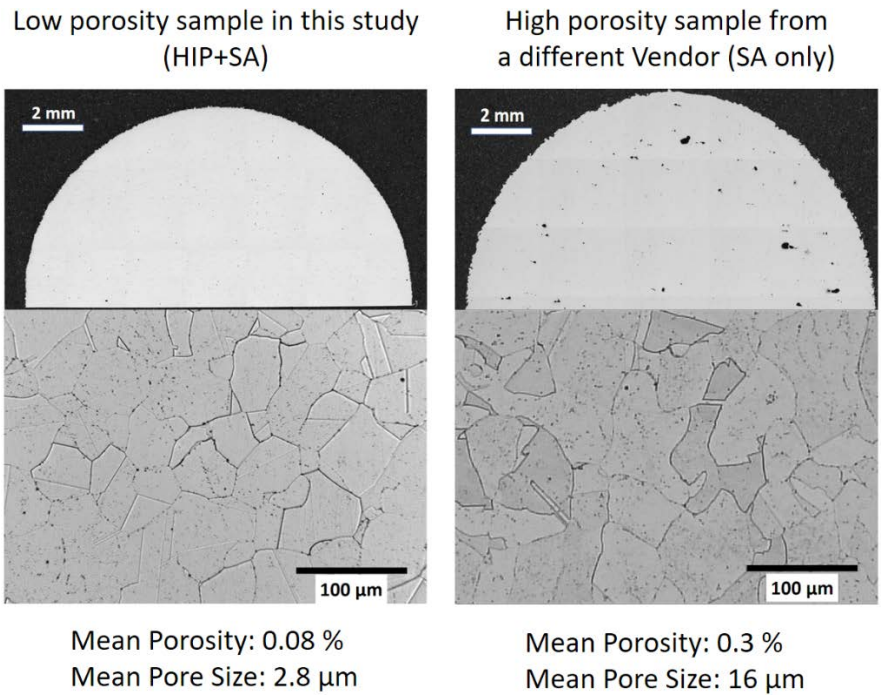

Fig. 29. Comparison of porosity and microstructure between the low porosity sample in this study (after HIP+SA) and the high porosity sample from a different vendor (SA only without HIP). The samples were etched by Kalling reagent.

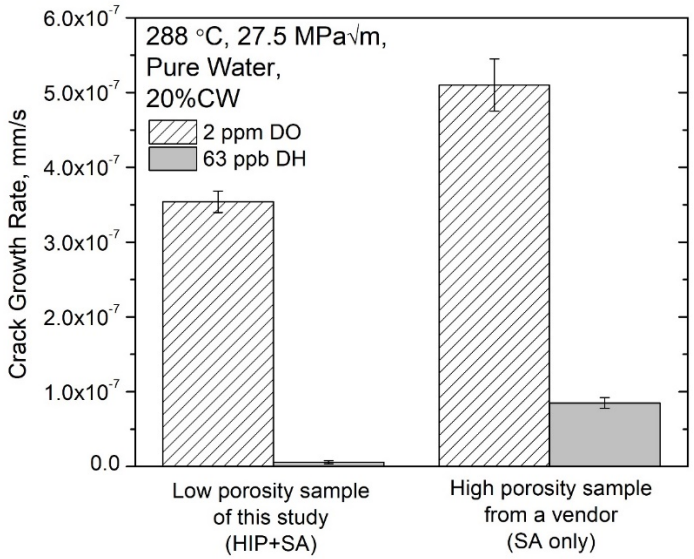

Fig. 30. Comparison of SCC growth rate in NWC and HWC 288°C water between the low porosity sample in this study (after HIP+SA) and the high porosity sample from a different vendor (SA only without HIP). Both materials were cold forged to introduce 20%CW before testing.

6.6. Effects of oxide inclusions

Fig. 31 compares the SCC growth rates of AM 316L SS (HIP+SA, with inclusions) and wrought 316L SS (with few inclusions) tested in the same laboratory. All materials had a similar grain size and were 20% cold-forged. Although AM 316L SS exhibited crack growth rates on the high end of the spectrum, there is no significant difference in crack growth rate between AM and wrought materials. Fig. 32a shows a typical cross-sectional view of the crack. Extensive secondary cracking was visible along the main crack after the transition from the fatigue pre-cracking to the constant load SCC. The cracks remained intergranular, but exhibited more branching than is usually seen in wrought SS. A close look at the secondary crack tips in Fig. 32b revealed the oxidized inclusions lined up along the oxidized grain boundaries. EDS mapping at the crack tip (squared region) confirmed that the oxidized spheres were rich in chromium (Cr) and iron (Fe). Si was not found, but Si was detected in the oxides close to the crack tip. Fig. 33 shows the fracture surface of the stress corrosion crack in AM 316L SS. While the fractography clearly indicates that AM 316L SS exhibited intergranular SCC, the material showed a unique morphology on its grain boundaries. The fracture surface was decorated with a high density of the corroded spots along the grain boundaries. This was easier to observe at locations closer to the crack tip, where there was less general corrosion due to the long-term exposure to high temperature water after the cracks formed. High magnification EDS mapping at the squared region in Fig. 34 showed Si rich oxide inclusions completely dissolved from the original locations, and some reprecipitated on iron oxide at different locations. In areas where the silica inclusions were dense, the oxidized spots might form an easier crack path along the grain boundaries. The dissolution of silicas promoted the oxidation with thick Cr rich, but Fe and Ni deficient oxide around their original locations. In BWR high temperature water, oxide formation has been well understood in both NWC and HWC [60, 61]. High Cr spinel ($FeCr_2O_4$) was reported near the metal-oxide interface on the SS [60]. To the best of our understanding, the formation of Cr only oxide was rarely seen in the same environment. Further work is needed to recognize this unique phenomenon caused by oxide inclusions at grain boundaries. Still, these experimental observations confirmed that silica inclusions in AM 316L SS can fully dissolve and change the oxidation behavior of the grain boundary in high temperature water. Furthermore, the dissolution of inclusions can promote the crack branching in AM 316L SS, as shown in Fig. 31a.

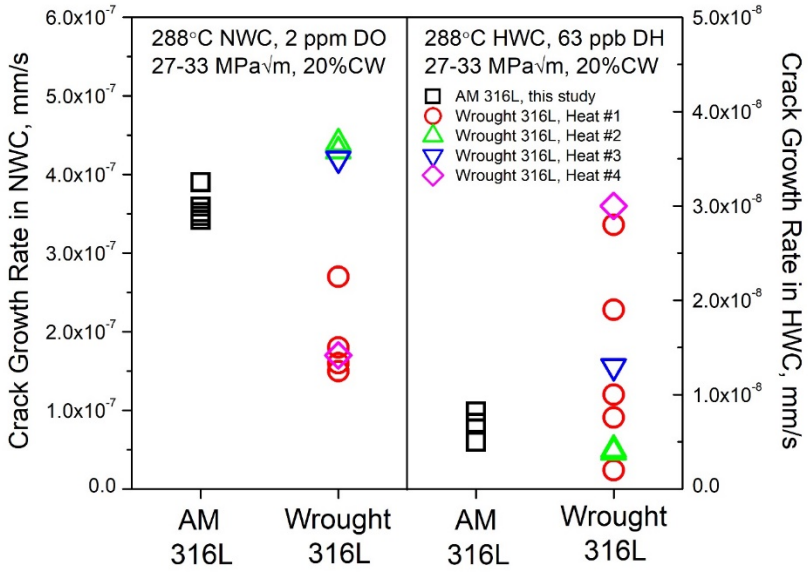

Fig. 31. A summary of SCC growth rate data of AM 316L SS (HIP+SA) and various heats of wrought 316L SS in 288°C high temperature water. All materials contained 20% cold work by warm-forging at 200°C.

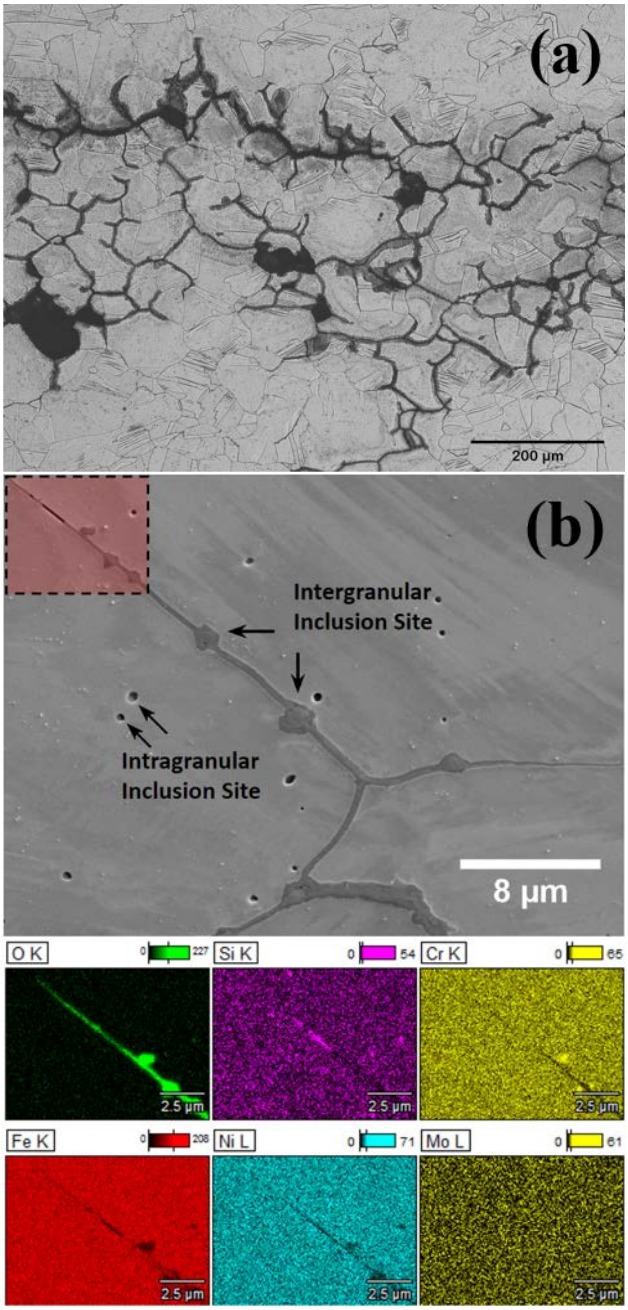

Fig. 32. The cross-sectional images of SCC in AM 316L SS after testing in high temperature water: (a) optical micrograph of the crack branching along the main crack; (b) high magnification SEM image and EDS map (squared region) of the secondary crack tip.

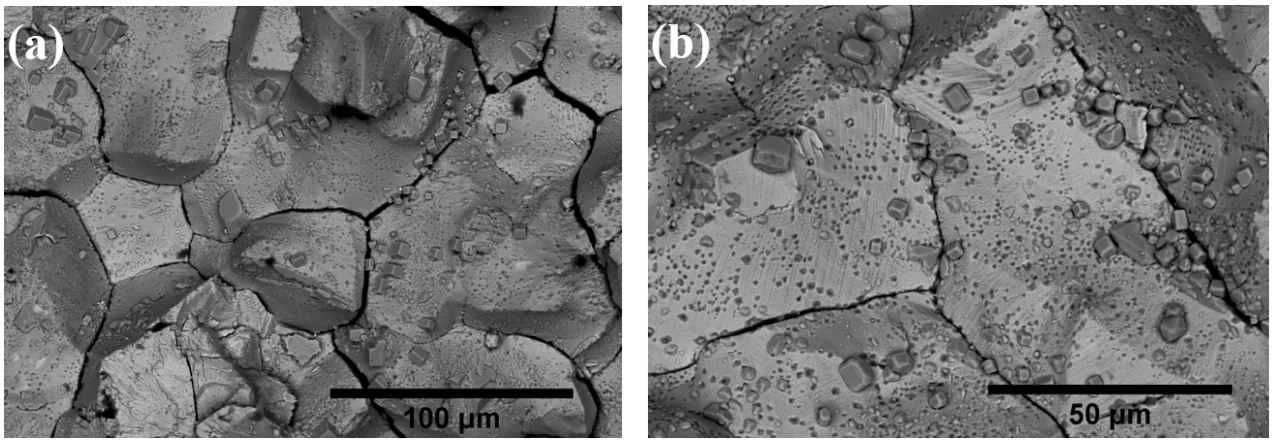

Fig. 33. Back-scattered electron image of the fracture surface on AM 316L SS (HIP+SA, 20%CW) after SCC growth test in high temperature water: (a) low magnification; (b) higher magnification.

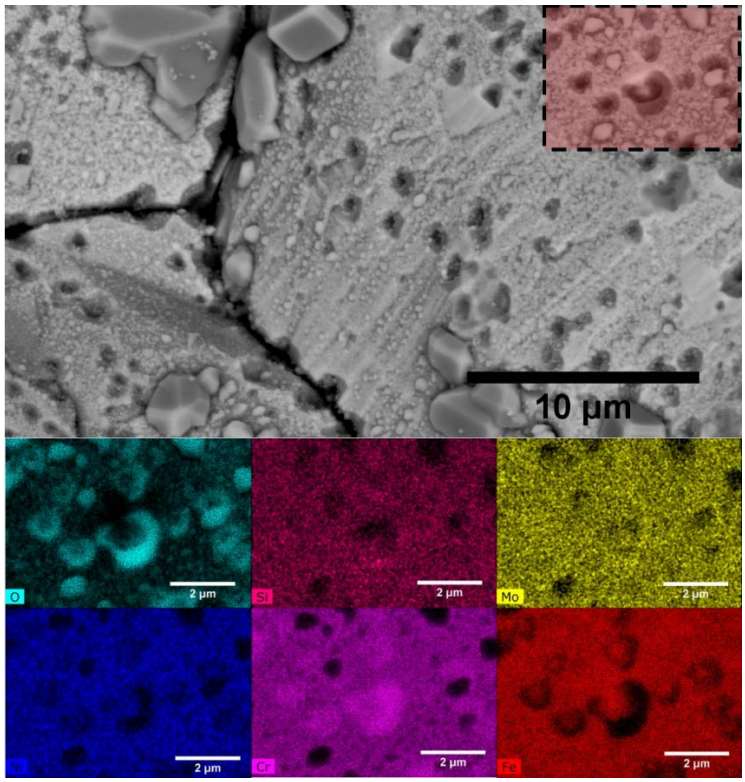

Fig. 34. SEM-EDS elemental mapping (squared region) of the dissolved inclusions and oxidation on the fracture surface on AM 316L SS (HIP+SA, 20%CW) after SCC growth test in high temperature water.

7. Corrosion Fatigue Crack Growth Behavior

7.1. Experiment

The corrosion fatigue crack growth test was performed under K control in sine waveform. With a focus on the environmental effect on 316L SS, the fatigue loading was conducted in the low-cycle region (10^{-3} to 1 Hz). The ΔK level (K_{max} - K_{min}) and the load ratio R = P_{min} / P_{max} or K_{min} / K_{max} were varied in the ranges of 8 to 20 MPa√m and 0.2 to 0.6 respectively. For all the CT specimens, the tests were conducted using the same sequence to reduce the test errors from CT specimen to CT specimen. Sufficient crack extension should be allowed between loading variables to achieve a steady-state crack growth rate. To ensure linear elastic fracture mechanics, the K_{max} values in all the loading tests were controlled well below the required limits of ASTM E399 [62] and E647 [41]. The K_{max} and ΔK values were calculated per ASTM E399 using the load and the actual measured crack length derived from the DCPD. K_{max}, ΔK, R, and load frequency can be controlled within each experimental phase to ensure an accurate crack growth rate measurement and flexibility for mechanistic studies.

7.2. Corrosion fatigue crack growth in air

Fig. 35 summarizes the fatigue crack growth rate of AM 316L SS under different ΔK at K_{max}=27.5 MPa√m and 0.5 Hz load frequency in air. A calculation based on the Paris law relationship in Section XI of the ASME BPV code for austenitic stainless steel in air was also plotted in Fig. 35 for comparison. Both HIP+SA specimen and SA only specimen exhibited similar fatigue crack growth rates under the same testing condition. The rates were also very close to the Section XI values. Therefore, with relatively slow load cycle, AM 316L SS shows very similar fatigue crack growth rate as wrought material in air.

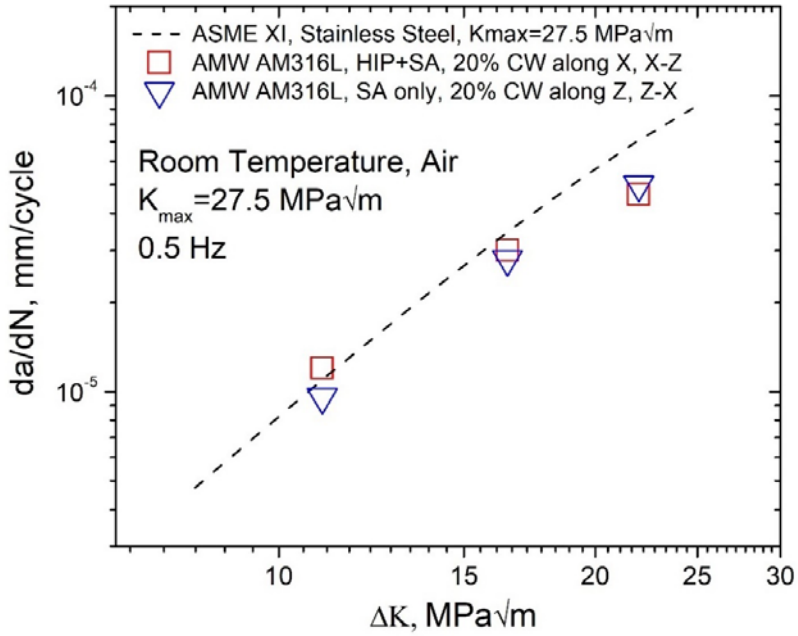

Fig. 35. A summary of fatigue crack growth rates in air for AM 316L stainless steel (HIP+SA vs. SA only). A calculation based on the Paris law relationship in Section XI of the ASME BPV code for austenitic stainless steel in air is also plotted for comparison.

7.3. Corrosion fatigue crack growth in BWR water

In high temperature water, the environment would influence the fatigue crack growth rate. Fig. 36 shows a summary of corrosion fatigue crack growth rates in BWR water environment for AM 316L stainless steel under various conditions (different heat treatments, cold work levels, crack orientations). A calculation based on the Paris law relationship in Section XI of the ASME BPV code for austenitic stainless steel in air is also plotted for comparison. Most corrosion fatigue crack growth data are above the ASME line which suggests an environmental effect. As the ΔK decreases, the deviation from the ASME line increases. The difference among all these materials were not significant which suggests that the corrosion fatigue crack growth of AM 316L SS is similar to that of its wrought counterpart under relatively low cycle fatigue loading.

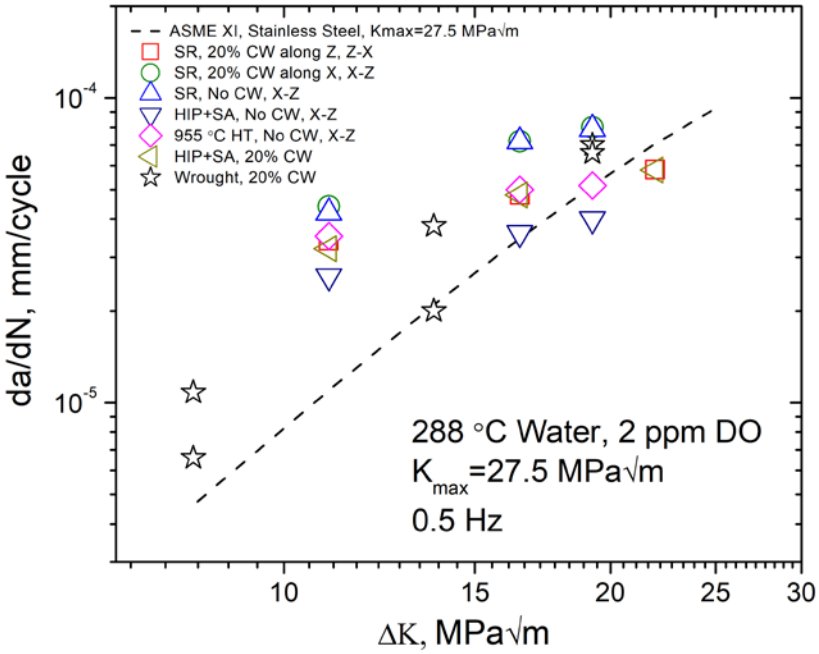

Fig. 36. A summary of corrosion fatigue crack growth rates in BWR water environment for AM 316L stainless steel under various conditions (different heat treatments, cold work levels, crack orientations). A calculation based on the Paris law relationship in Section XI of the ASME BPV code for austenitic stainless steel in air is also plotted for comparison.

To illustrate the underlying mechanism, a controlled load transition from high frequency to low frequency, and eventually to constant load was conducted during a test. Fig. 37 shows the fracture morphology changes in the transition region as the loading frequency decreased. In contrast to the similar transgranular cracking morphology in the high frequency region, the materials show clear differences when the loading frequency decreased below 0.01 Hz. For the stress-relieved material in Fig. 37a, the fracture transitioned from predominantly transgranular to a mixed mode (transgranular and interdendritic/intercolumnar) features. The crack exhibited a rougher surface in the low frequency region. For the solution-annealed material in Fig. 37b, the transgranular crack (> 0.1 Hz) slowly transitioned to a mixed mode (0.01–0.001 Hz), and eventually to an intergranular crack mode (under constant load or no cyclic loading). The increasing differences in da/dN at lower frequencies can be attributed to the different paths that cracks take in the materials when corrosion becomes more dominant.

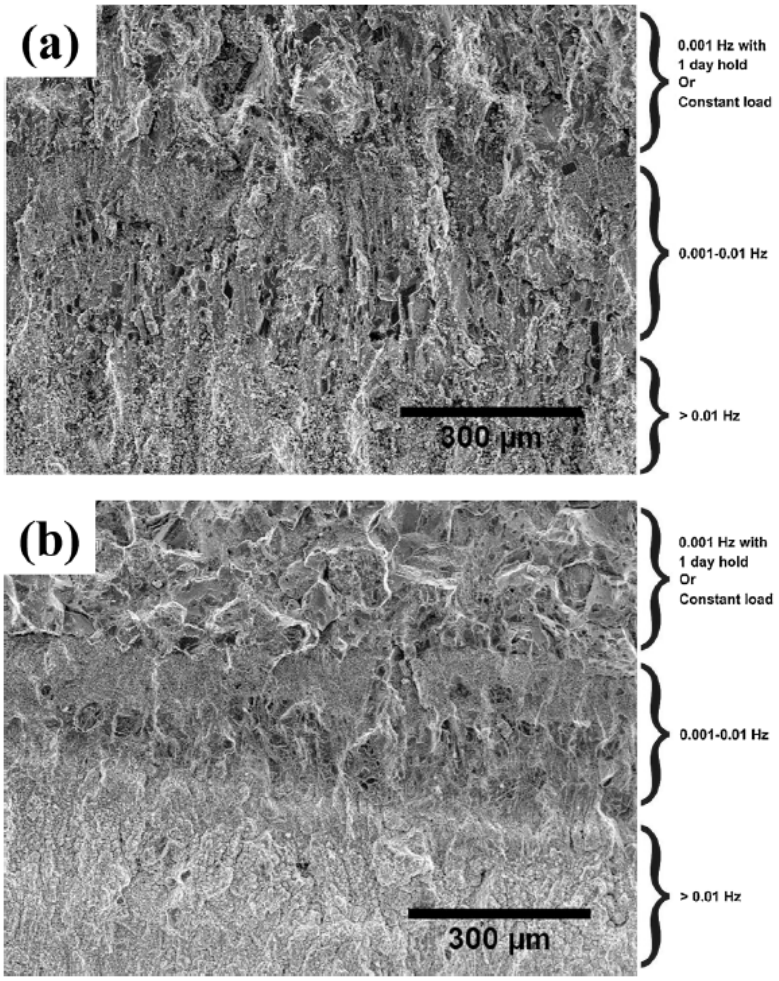

Fig. 37. Changes in fracture morphology as the loading frequency reduces: (a) stress relief, X-Z orientation; (b) HIP followed by high temperature annealing. The testing condition for both specimens was K = 27.5 MPa√m, R = 0.6, 288°C high temperature water with 2 ppm dissolved oxygen.

8. Irradiation Effects and IASCC of AM 316L

Laser powder bed fusion (L-PBF) is an emerging additive manufacturing technique receiving growing attention in both industry and academic research [63-65]. This manufacturing technique builds a 3-dimensional structure in a layer by layer fashion from computer-aided design (CAD) model, which allows unparalleled design freedom and a short lead time. Recently, the nuclear industry has been exploring the use of additive manufacturing technique for reactor internal applications to enhance performance, reduce the supply chain, cost, and time to market [66]. L-PBF is appropriate for small internal components (<100 lbs), including fuel assemblies, control rod drive internals, small spray nozzles, steam separator inlet swirler, flow deflectors, and Gen IV cooling channels [67]. The reliability of these parts is strongly dependent on the quality of the built materials.

Austenitic 316L stainless steel (SS) is still the dominant structural alloy in light water reactors (LWRs). Extensive efforts have been made to improve the quality of additively manufactured (AM) 316L SS for critical applications. With proper processing condition, AM 316L SS can be made to be nearly fully dense, with excellent tensile properties and good fatigue performance [68-70]. Lou *et.al.* [71-73] systematically studied the microstructure, heat treatment, cold work level, crack orientation, and oxidizing vs. reducing medium on the stress corrosion cracking (SCC) behavior of AM 316L SS in simulated boiling water reactor (BWR) environment, and demonstrated the potential of heat treated AM 316L SS for nuclear application.

However, radiation poses additional issues on the performance of AM 316L SS. The interaction of irradiated materials, corrosion environment, temperature and stress leads to the degradation mode of irradiation assisted stress corrosion cracking (IASCC) [74-78]. IASCC is also considered as one of the primary degradation modes of core internal components in light water reactors (LWRs) that emerges between ~0.7 dpa and a few dpa [79]. The occurrence of IASCC has been reported for 304 and 316L stainless steels, nickel-base alloys 600, X-750, and 718 in fuel cladding, control rod blades, and various bolts and springs in pressurized water reactors (PWRs) or boiling water reactors (BWRs) [75].

Characterization of the irradiated microstructure is the first step in understanding IASCC mechanism. Irradiation induces significant changes in microstructure such as formation of dislocation loops, cavities, and precipitates, and elemental segregation [80], which are highly dependent on the initial microstructure and chemical composition of the alloy. Dislocation loops, cavities and precipitates can serve as barriers for dislocation motion and induce hardening and embrittlement, which may adversely impact the IASCC susceptibility. The radiation induced segregation (RIS) at GB is another potential factor contributing to IASCC. Cr depletion at GB may lead to loss of passivation, and an increase in the susceptibility of IASCC.

In this section, we present the study of proton- and heavy ion-irradiated AM 316L SS produced by L-PBF method. The proton irradiated microstructure was investigated, and the IASCC was evaluated in both proton- and heavy ion-irradiated conditions. Significant anisotropic cracking behavior was observed in stress-relived condition. Post-printing hot isostatic pressing (HIP) was found to be critical to improve the IASCC resistance of AM 316L SS. These results from AM alloys were also compared with that of conventionally forged 316L stainless steel.

8.1. Experimental

The commercial-graded forged 316L SS material baseline was a verified good heat ordered by GE Nuclear from Crucible Specialty Metals in 1995, which has been widely tested in many earlier GE, EPRI, and DOE programs. All the irradiation and IASCC results from this heat of 316L SS presented here are recently reported in Ref. [81]. For the AM material, commercial 316L SS powder

was provided by Carpenter Powder Products. Only powder below 325 mesh size with less than 3wt% of size below 15 μm was used. AM 316L cubic blocks were printed with a laser power of 195 W, scan speed of 1.2 m/s, and 20 μm powder lay thickness.

The conventionally forged 316L material is referred here as forged 316L. Two different heat treatment conditions were applied to the as-printed AM 316L SS in this study. An annealing at 650°C for 2h produces a stress-relieved (SR) condition. Another follows hot-isotropic pressing (HIP) at 1150°C for 4h, and solution annealing at 1066°C for 1h to remove grain boundary carbides. The second is referred as HIP condition.

Both proton and self-ion irradiation experiments were conducted using a 3 MV NEC Pelletron accelerator in the Michigan Ion Beam Laboratory (MIBL) at the University of Michigan. Four tensile samples and three TEM samples were irradiated on a specially designed stage, as shown in Fig. 38. There was one TEM sample on both sides of the stage that served as the guide sample and was not fully irradiated. Four thermocouples were welded on the guide samples, used for calibrating the temperature of the samples. The irradiation area was about 16 mm wide and 10 mm long therefore, only the central part of the samples was irradiated. Both ends of the samples were positioned outside of the irradiation area. A schematic diagram of the stage design is illustrated in Fig. 39. The cross-sectional view of the stage is shown in Fig. 40, which shows a heater and an air cooling loop beneath the copper block, which were used to control the temperature of the samples.

Proton irradiation was conducted with 2 MeV protons at a dose rate of about 1.6×10^{-5} dpa/s to a damage level of 2.5 dpa at 360°C while self-ion irradiation was conducted with 5 MeV Fe^{++} at a dose rate of 6.3×10^{-4} dpa/s to a damage level of 100 dpa at 400°C. The irradiation parameters are listed in Table 5. The dose and dose rate were estimated using SRIM 2013 (Quick K-P option) with a displacement energy of 40 eV. An example of the damage profile is shown in Fig. 41. The resulting damage layer was approximately 20 microns deep with relatively uniform damage in the first 15 microns for proton irradiation.

During the irradiation, infrared thermal images taken by the FLIR camera (A310 Series) were used to monitor the temperature for both proton and self-ion irradiations. Throughout the irradiation, the sample temperature was maintained at 360 ± 4 °C and 400 ± 5.1 °C. Part of the temperature was due to the beam heating and the rest came from the heater. Before irradiation, the stage was first heated to the target temperature by the heater to calibrate the emissivity for the infrared camera. Three ROIs (regions of interest) were selected in the irradiation area on each sample at upper, middle, and bottom locations, as shown in Fig. 42. Once the beam hit the stage, the temperature increased sharply. The heater and the air cooling loop were adjusted based on the infra-red thermal image to achieve the irradiation temperature.

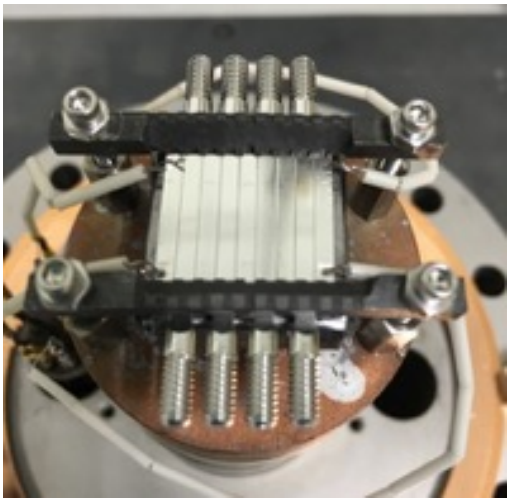

Fig. 38. Photo of the irradiation stage with 316 SS tensile and TEM samples (example: 2.5 dpa proton irradiation stage).

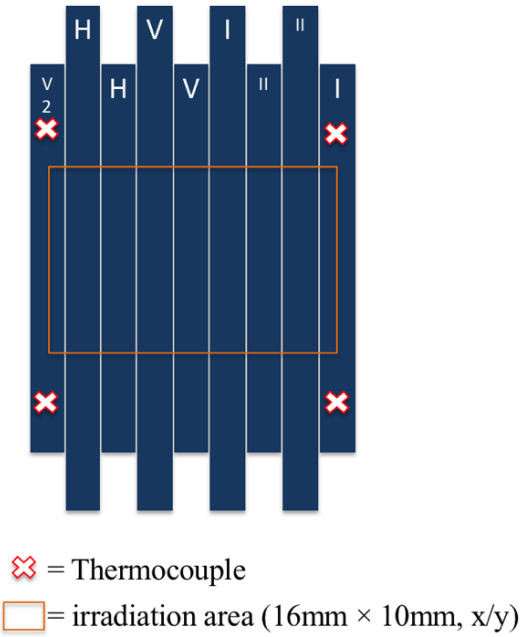

Fig. 39. Schematic diagram of the irradiation stage (2.5 dpa proton irradiation).

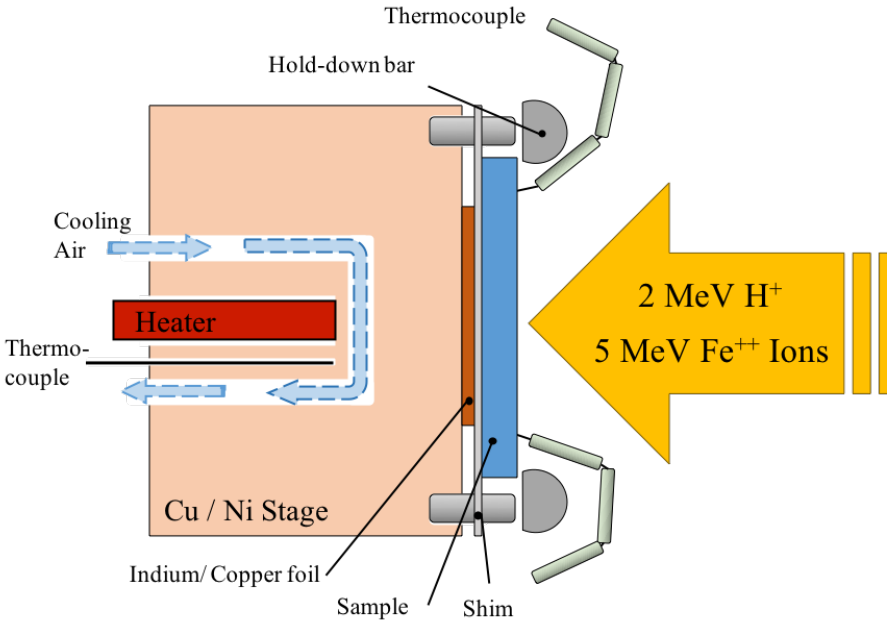

Fig. 40. Schematic diagram of the cross-sectional view of the irradiation stage.

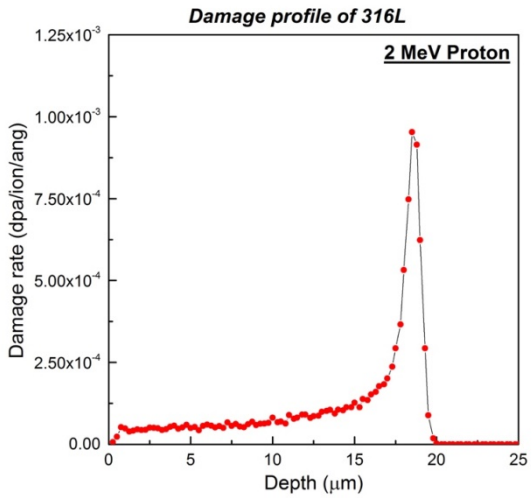

Fig. 41. Damage profile of 316L under 2 MeV proton irradiation.

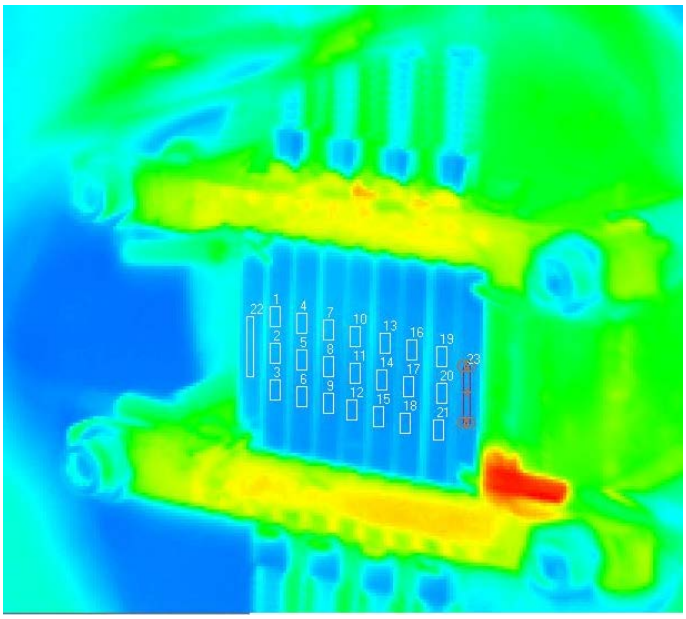

Fig. 42. Infrared image of the irradiation stage (example: proton irradiation).

Table 5 Parameters of irradiation experiments.

Parameter	2 MeV H+	5 MeV Fe++
Dose (dpa)	2.5	100
Temperature (°C)	359.9 ± 4	400.4 ± 5.1
Damage rate (dpa/s)	1.6×10^{-5}	6.3×10^{-4}
Current (μA)	37	0.618

During each irradiation, various experimental parameters were recorded. The following results are from the proton irradiation to a dose of 2.5 dpa and are used as an illustration of the recorded data. Pressure of the entire beam line is plotted Fig. 43 in and beam current is shown in Fig. 44. Temperature histograms of each sample are plotted in Fig. 45.

The pressure of the chamber where the stage was located was between 10^{-7} and 10^{-8} torr. Under this high vacuum, no oxide was formed on the surface of the sample during the irradiation. The total beam current was around 55 μA, which was the maximum stable beam current that was achieved by the accelerator. About two-thirds of the beam, near 37 μA, was on the stage with the balance on the slits. This ensured that the samples were fully irradiated during the raster-scanning process. The temperature histogram showed the temperature distribution of three different positions located in the irradiation area of each sample. Generally, it follows a normal distribution, and the three positions: upper, middle, and bottom, were overlapped with each other. The average temperature for each sample was around 360 °C, and the standard derivation valve is less than 5°C. Thus, it ensured that the proton irradiation performed well with maximum current under high vacuum at 359.9 ± 4 °C. The beta counting was conducted for each sample after irradiation to confirm that the samples were irradiated uniformly. The bar diagram of beta counting of the proton is shown in Fig. 46.

Similar recorded data for self-ion irradiation to a dose of 100 dpa are plotted in Figs. 47-49 for pressure, current, and thermocouple histories, respectively. Temperature histograms of representative samples are plotted in Fig. 50.

The pressure in the irradiation chamber was between 10^{-7} and 10^{-8} torr. Under this high vacuum, no oxide was formed on the surface of the sample during the irradiation. The total beam current was around 55 μA, which was the maximum stable beam current that was achieved by the accelerator. About two-thirds of the beam, or near 37 μA, was on the stage with the balance on the slits. This ensured that the samples were fully irradiated during the raster-scanning process. The temperature histogram showed the temperature distribution of three different positions located in the irradiation area of each sample. Generally, it followed a normal distribution, and the three positions: upper, middle, and bottom, overlapped each other. The average temperature for each sample was around 360°C, and the standard derivation was less than 5°C. Thus, it ensured that the proton irradiation was performed well with maximum current under high vacuum at 360 ± 4°C. The beta counting was conducted for each sample after irradiation to confirm that the samples were irradiated uniformly. The bar diagram of beta counting of the proton is shown in Fig. 46. Pressure, current, and thermocouple histories for self-ion irradiation to a dose of 100 dpa are plotted in Figs. 47, 48, and 49, respectively. Temperature histograms of representative sample are plotted in Figure 50.

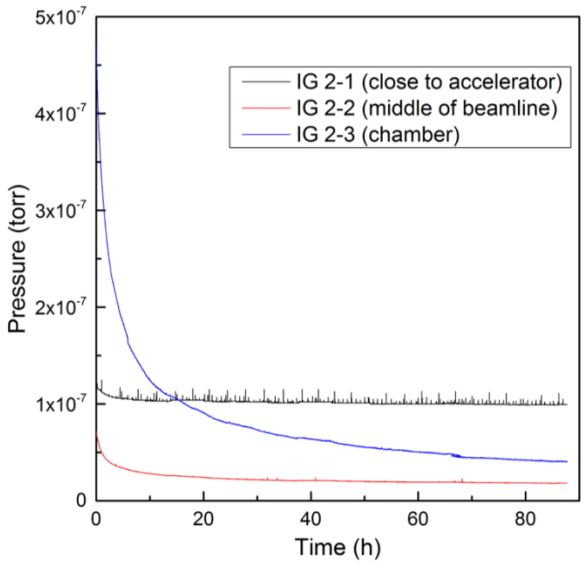

Fig. 43. Pressure of the beam line during the proton irradiation of 316L to a dose of 2.5 dpa.

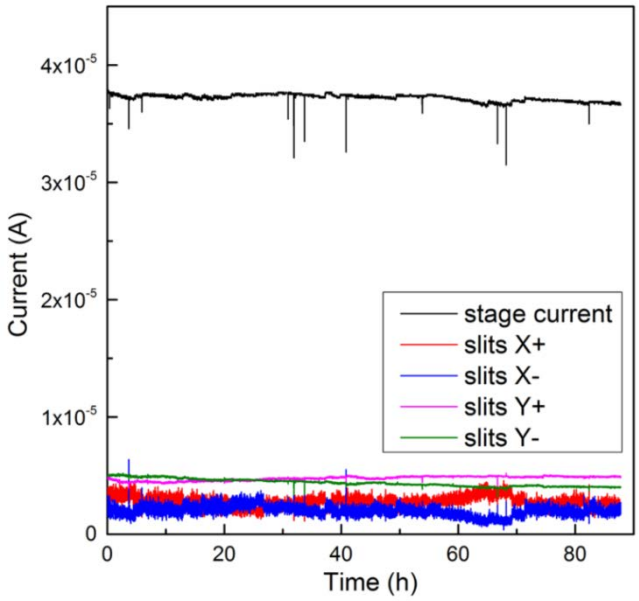

Fig. 44. Current of the proton irradiation of 316L to a dose of 2.5 dpa.

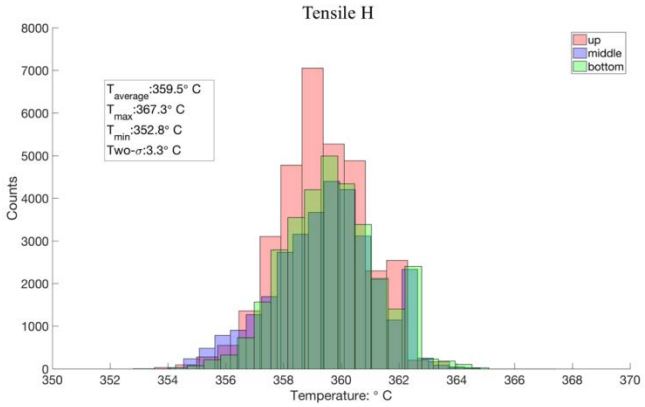

Fig. 45. Temperature history diagrams of proton irradiation to a dose of 2.5 dpa.

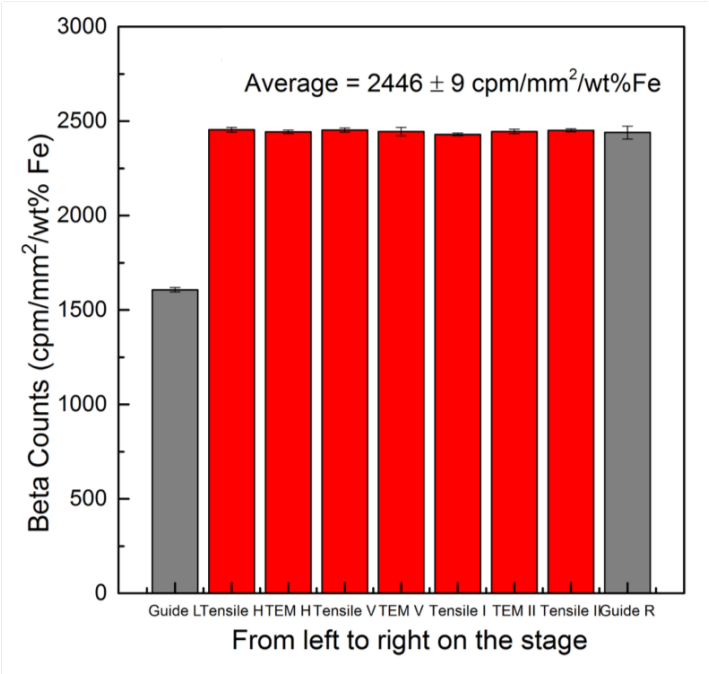

Fig. 46. Bar diagram of beta counting of each sample after 2.5 dpa proton irradiation.

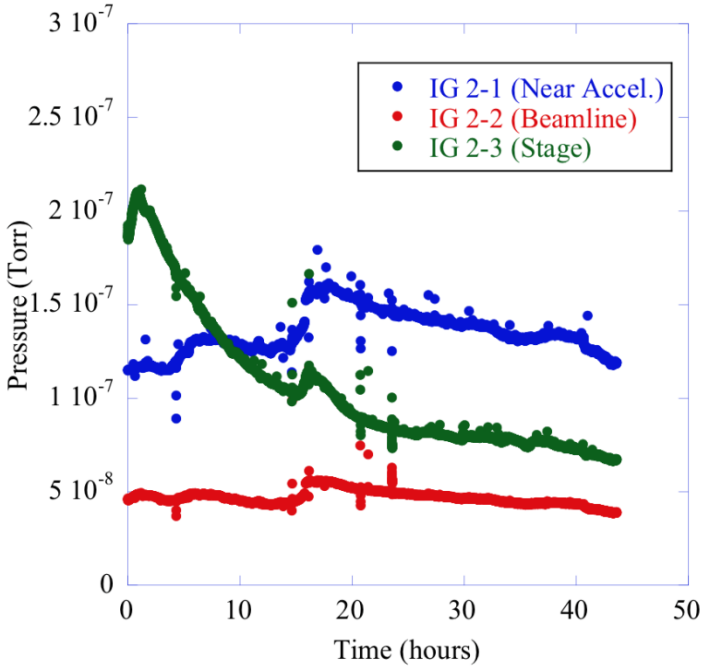

Fig. 47. Pressure of the beam line during the self-ion irradiation of 316L to a dose of 100 dpa.

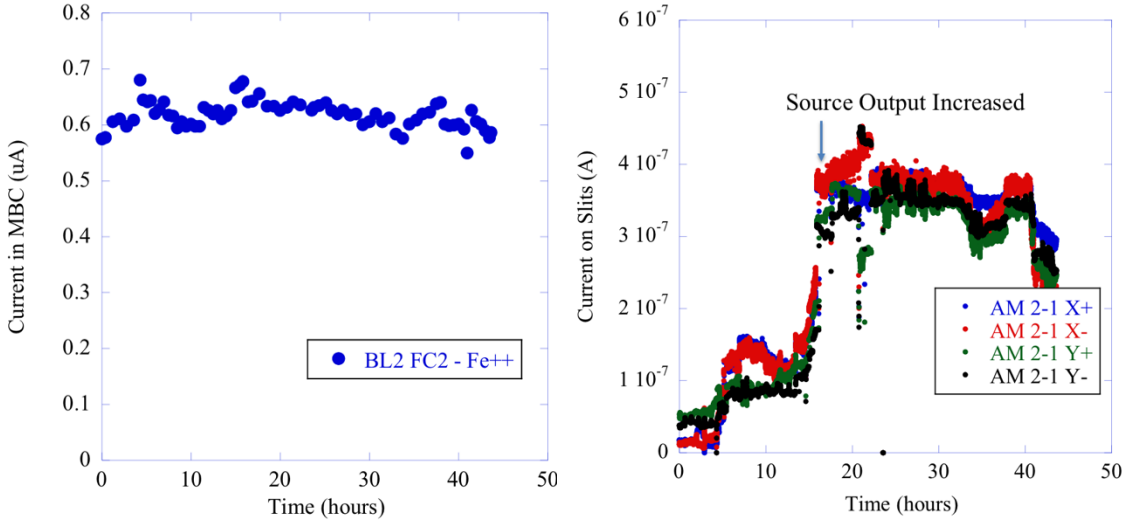

Fig. 48. Current of the self-ion irradiation of 316L to a dose of 100 dpa, current on stage (left) and current on slits (right).

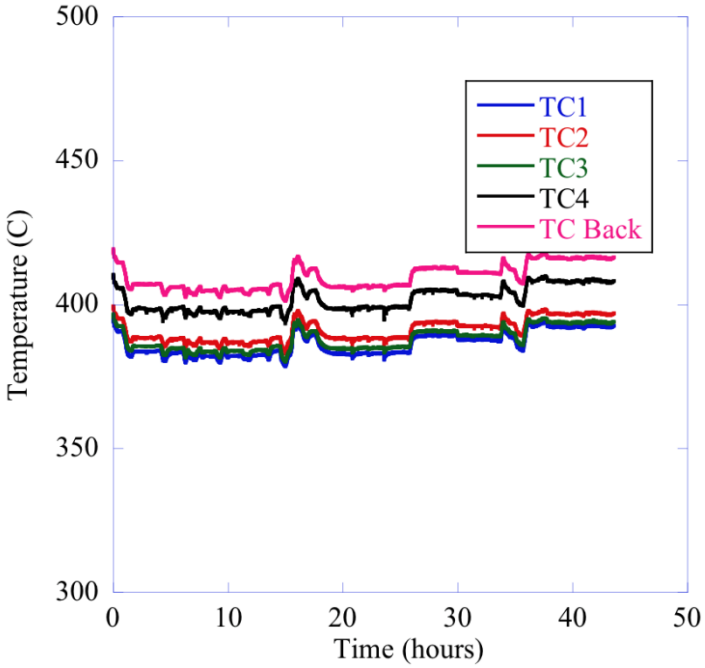

Fig. 49. Thermocouple history of the self-ion irradiation of 316L to a dose of 100 dpa.

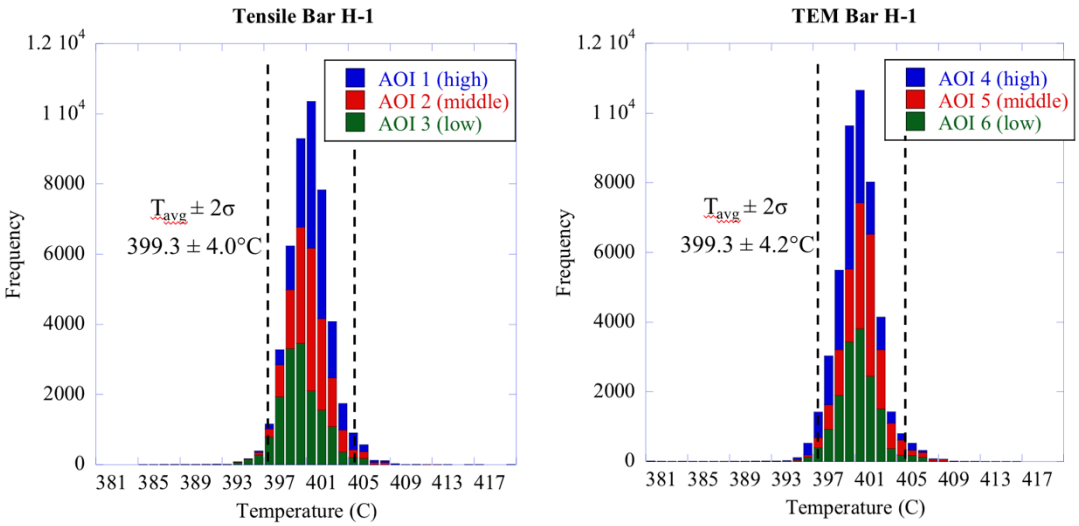

Fig. 50. Temperature history diagrams of self-ion irradiation to a dose of 100 dpa.

TEM disks were prepared with a twinjet polisher at 0°C and 10-20 V using an electropolishing solution of 10vol.% perchloric acid methanol solution. Proton irradiated specimens were prepared by back polishing to a thickness of ~ 20 μm, and then polished from both sides until perforated. This procedure was conducted to place the electron transparent region of the disk at a depth of 10±1.5μm, within the irradiated region of the sample bar. Electron backscatter diffraction (EBSD) mappings were performed on AR materials in a FEI Helios 650 system operating at a voltage of 20 kV and a working distance of 10 mm. The step size for EBSD collection was 0.2 μm. Backscatter electron (BSE) images were taken at a working distance of 4 mm.

Dislocation loops were imaged using a dark-field, red rod technique [82] on a JEOL 3011 microscope. Voids were confirmed by the under- and over-focus method. Precipitates were imaged by the dark field technique. The exposure time for dark-field was set to 4 s. All the instrumentation for the present work was performed at the Michigan Center for Materials Characterization. Only the proton irradiated microstructure is presented here.

The IASCC initiation susceptibility was evaluated in simulated Boiling Water Reactor (BWR) normal water chemistry (288°C, 1500 psi, 2ppm, dissolved oxygen and conductivity less than 1 μS/cm) in the High Temperature Corrosion Laboratory (HTCL) at the University of Michigan. A strain rate of 1×10^{-7}/s was applied until a plastic strain of 4% was reached. Fig.51 shows the gage section of the tensile bars relevant to the built direction of the AM 316L materials. Both proton and heavy ion irradiation were performed on the Y-Z-plane as shown. However, the CERT specimens were pulled along the Z or X direction to check the potential for anisotropic behavior.

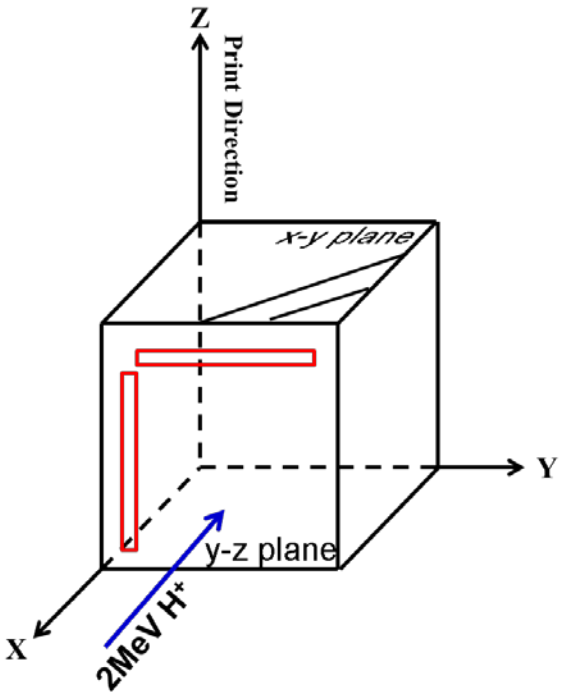

Fig. 51. Schematic of the orientations for microstructure characterization and constant extension rate tensile testing. Both protons and heavy ion irradiation were performed on X-Z plane. Tensile test or constant extension rate test were performed along both Z (printed direction PD) and X direction (perpendicular to PD).

8.2. Irradiated microstructure

Significant microstructure changes were observed after irradiation in different 316L alloys, such as loops (Fig. 52), voids (Fig. 53) and precipitates (Fig. 54). The dislocation network in the SR condition was not fully recovered during the irradiation. A high density of dislocation loops was observed in the SR condition compared to the HIP condition (Figs. 52a-b). The printed alloys (SR or HIP AM 316L) generally showed a higher density of dislocation loops compared with the forged condition (Fig. 52c), but the size is smaller than in the forged 316L.

Irradiation induced nano-sized voids were observed in all the conditions as shown in Fig. 53. Higher density of voids was observed in the SR condition compared with that of HIP condition. The void density of the HIP alloy is even less than that of the forged alloys. The swelling is generally less than 0.05%.

Irradiation-induced γ′ phase was observed in all the condition after irradiation as shown in Fig. 54. The nanosized γ′ precipitated at line dislocations or dislocation loops. A lower density and smaller size γ′ phase was observed in the SR condition after irradiation compared with HIP and forged condition. The detailed data of these microstructure features is available in Table 6.

Table 6. Effect of 2 MeV proton irradiation to 2.5 dpa at 360 °C on the microstructure features

Alloy ID	Dislocation loops			γ′ precipitates			Voids		
	d(nm)	$\rho(10^{22}/m^3)$	$L(10^{14}/m^2)$	d(nm)	$\rho(10^{21}/m^3)$	fv(%)	d(nm)	$\rho(10^{21}/m^3)$	S(%)
SR AM 316L	18.9±9.0	4.7±1.9	8.9	6.2±2.5	5.5±3.1	.07	6.6±1.6	3.1±1.2	.047
HIP AM 316L	20.2±10.4	1.5±0.7	3.0	6.6±2.4	2.9±1.7	.04	8.4±2.0	0.08±0.04	.0025
Forged 316L	32.6±22.0	0.32±0.12	3.3	7.8±2.5	2.2±1.4	.06	19.5±4.9	0.34±0.19	.156

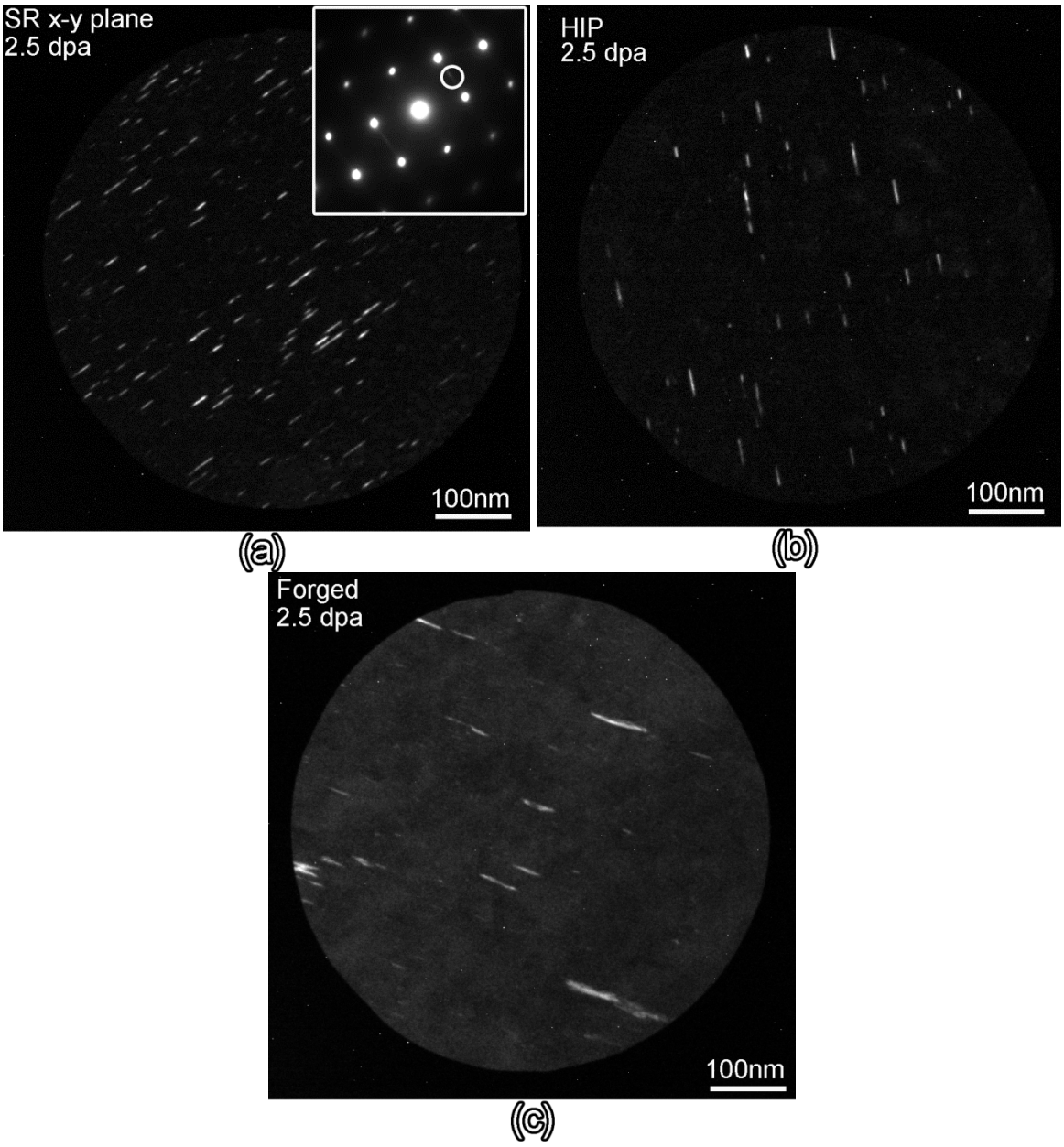

Fig. 52. Loops in irradiated 316L stainless steels after 2.5dpa irradaition at 360°C (a) Stress-relieved 316L with H-plane (b) HIPped (c) Conventional forged.

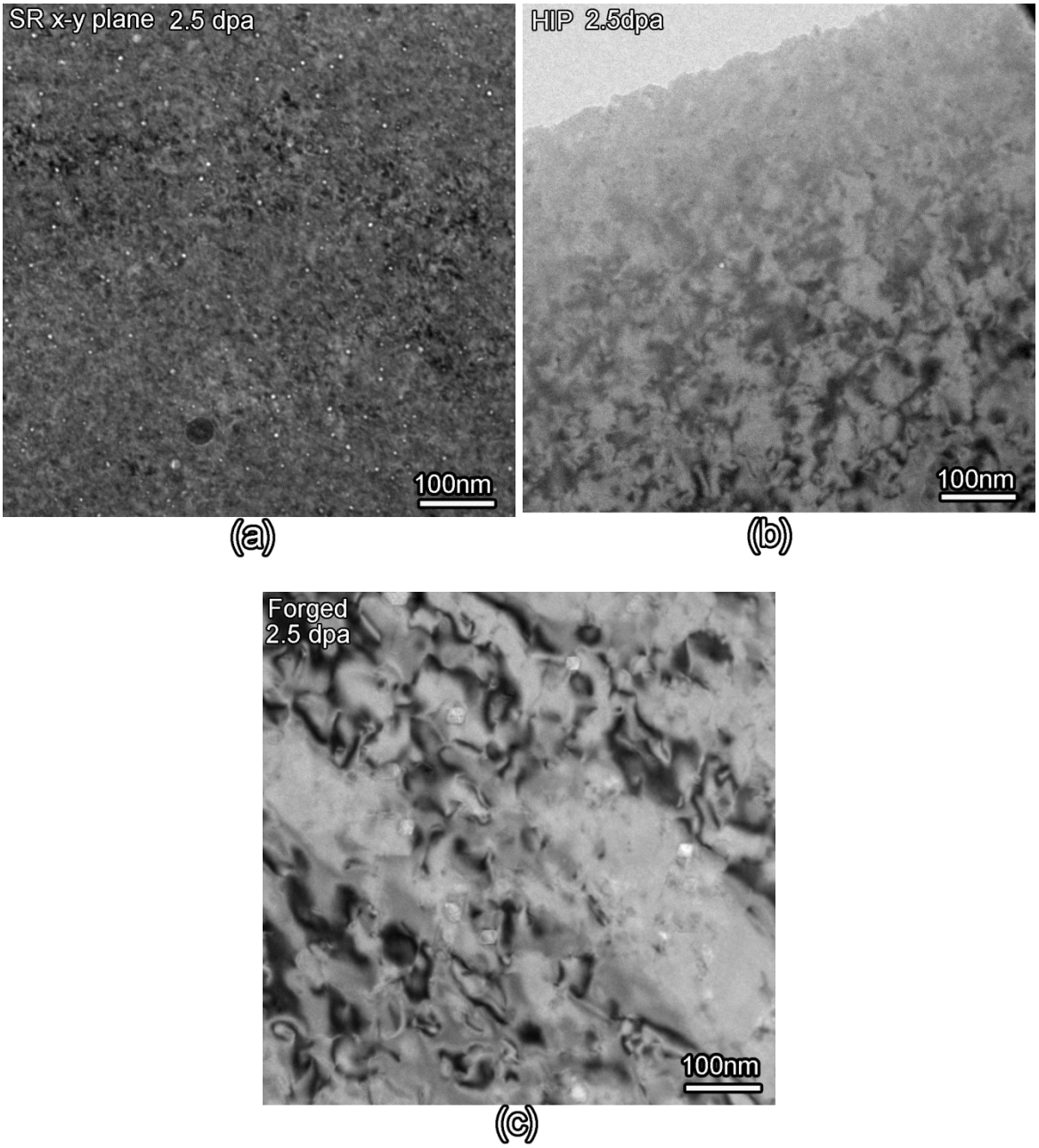

Fig. 53. Voids in irradiated 316L stainless steels after 2.5dpa irradaition at 360°C (a) Stress-relieved 316L with H-plane (b) HIPped (c) Conventional forged.

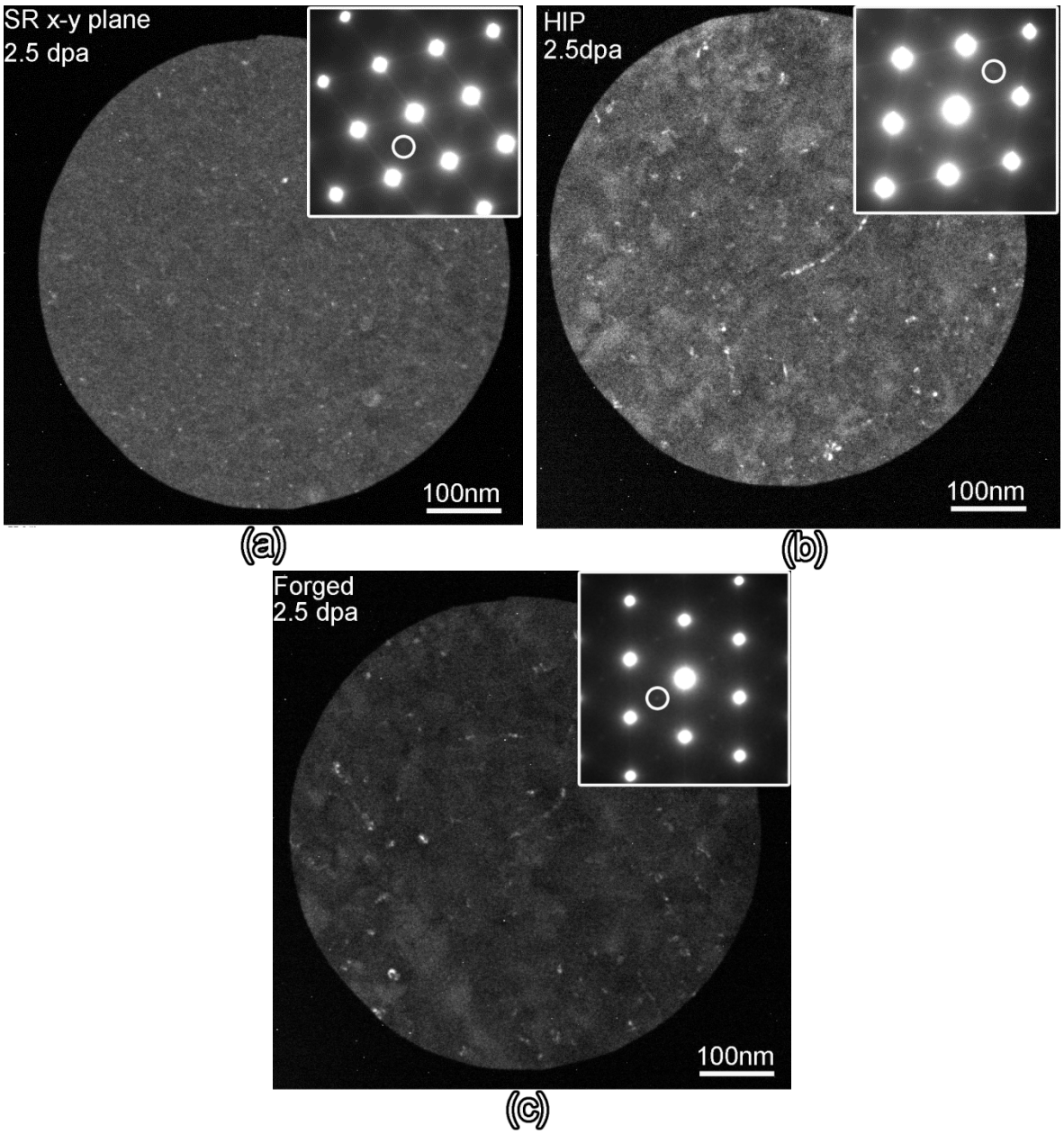

Fig. 54. Irradiation indcued γ′ precipitates in irradiated 316L stainless steels after 2.5dpa irradaition at 360°C (a) Stress-relieved 316L with H-plane (b) HIPped (c) Conventional forged.

8.3. Irradiation assisted stress corrosion cracking

The surface morphology of the tensile bar (irradiated area) after the CERT test is shown in Fig. 55. Cracks were observed in the irradiated area (IA) of SR 316L but absent in the unirradiated area (UIA), indicating the significance of irradiation in the SCC process. Few cracks were observed in the HIP AM 316L.

Significant anisotropy in cracking behavior was observed in SR AM 316L. For the samples pulled perpendicular to the printed direction, cracks were formed on the columnar grain boundary as shown in Fig. 55a. Meanwhile for the sample pulled along the printed direction, few SCC cracking was observed, Fig. 55b. However, cracks between layers were formed as shown in Fig. 55c. These

cracks between layers were also accelerated by the irradiation process but were largely absent in the unirradiated area.

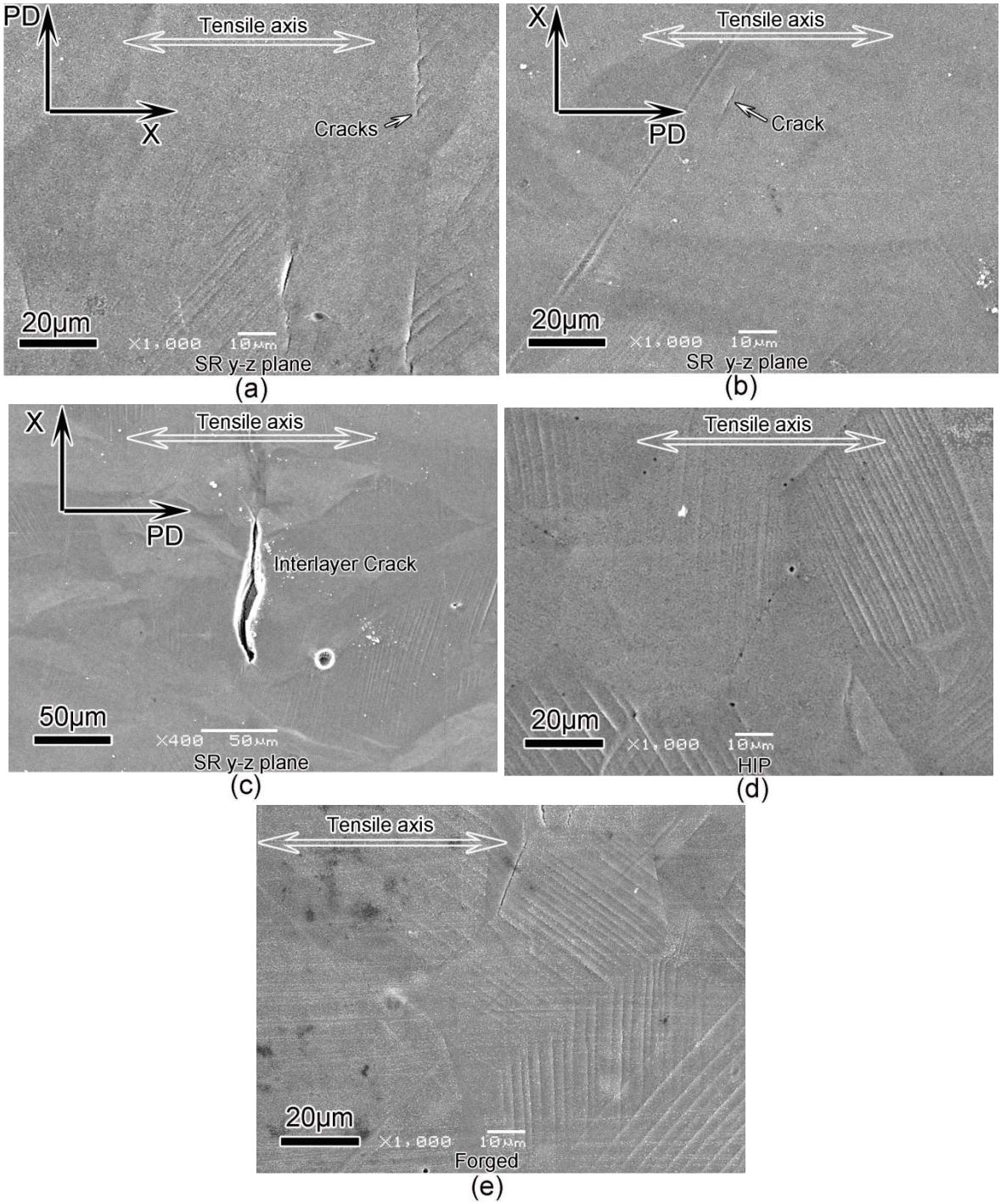

Fig. 55. SEM micrographs of irradiated area (2.5dpa) of the tensile bars of AM 316L SS strained to 4% in simulated BWR NWC (a) pulling along X direction of stess relieved AM 316L (b-c) pulling along printed direction of stress relieved AM 316L (d) HIPped AM 316L.

Crack length per unit area (the total crack length divided by analyzed area) was used to evaluate the cracking susceptibility as shown in Fig. 56. For proton irradiated samples, anisotropic cracking susceptibility was observed in that the cracking susceptibility is higher when pulled perpendicular to the printed direction than pulled along the printed direction in SR AM 316L. The cracking susceptibility of SR AM 316L was comparable to that of the forged material. HIP can significantly reduce the cracking susceptibility after proton irradiation. The cracking susceptibility after heavy ion irradiation shows the same trend as that after proton irradiation. Detailed data are listed in Table 7.

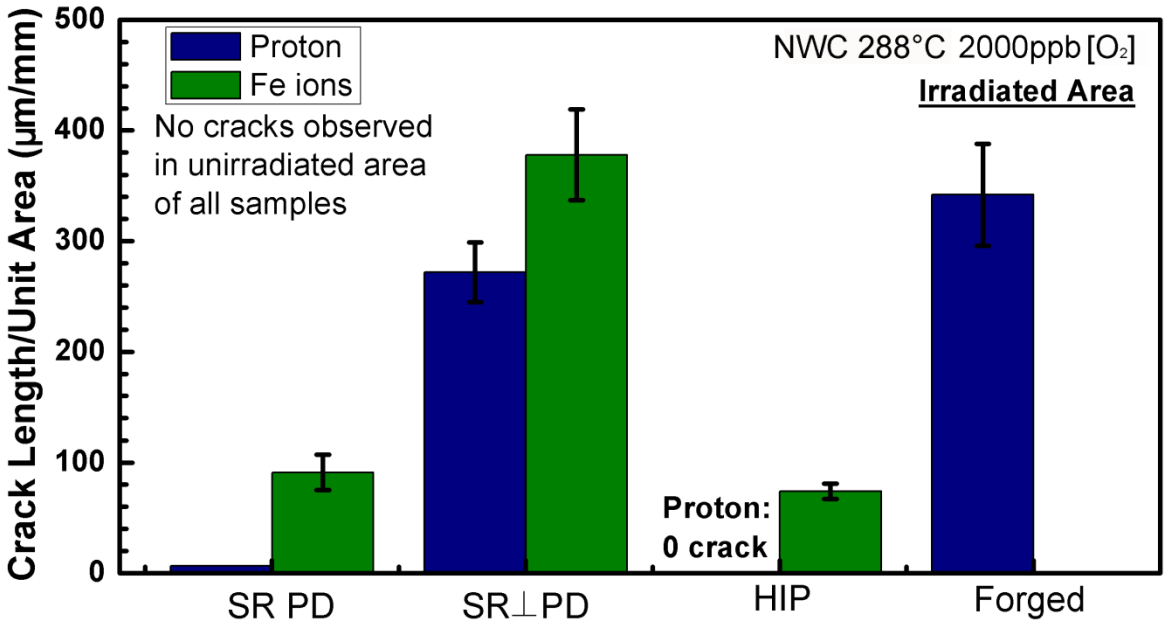

Fig. 56. Irradiation assisted stress corroison crackinig suspectibility of 316L after proton and heavy ion irradiation.

8.4. Results of AM alloy 800

Alloy 800 was tested only in the HIP condition. The fully recrystallization was not achieved even after HIP as shown in Fig. 57, where large grains mixed with fine grains. Processing related defects were observed after HIP.

Significant microstructure changes were observed after proton irradiation in alloy 800, such as formation of loops, voids, and γ′ precipitates as shown in Fig. 58. These features were all much larger than those in irradiated 316L, indicating a poor microstructure response to irradiation of alloy 800 compared to 316L.

No cracks were observed in the unirradiated area of the tensile bar. However, significant cracks were observed after irradiation as shown in Fig. 59. Both processing related and IASCC cracks were observed in the irradiated area. The cracking susceptibility was much higher than that of alloy 316L in the same processing condition (AM+HIP) as shown in Fig. 60. The detailed data is available in Table 7.

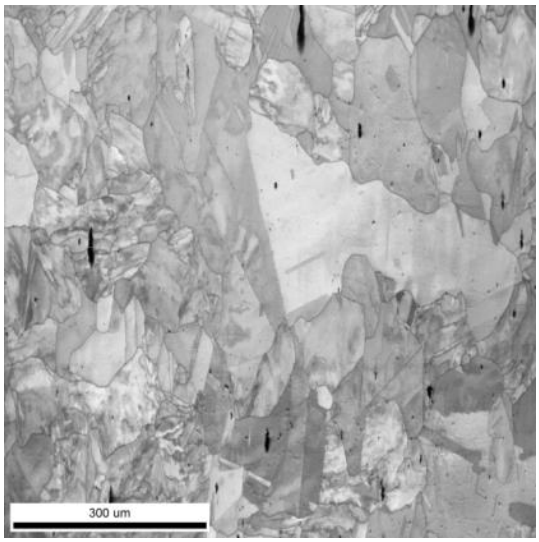

Fig. 57. Image quality map of AM alloy 800 after HIP.

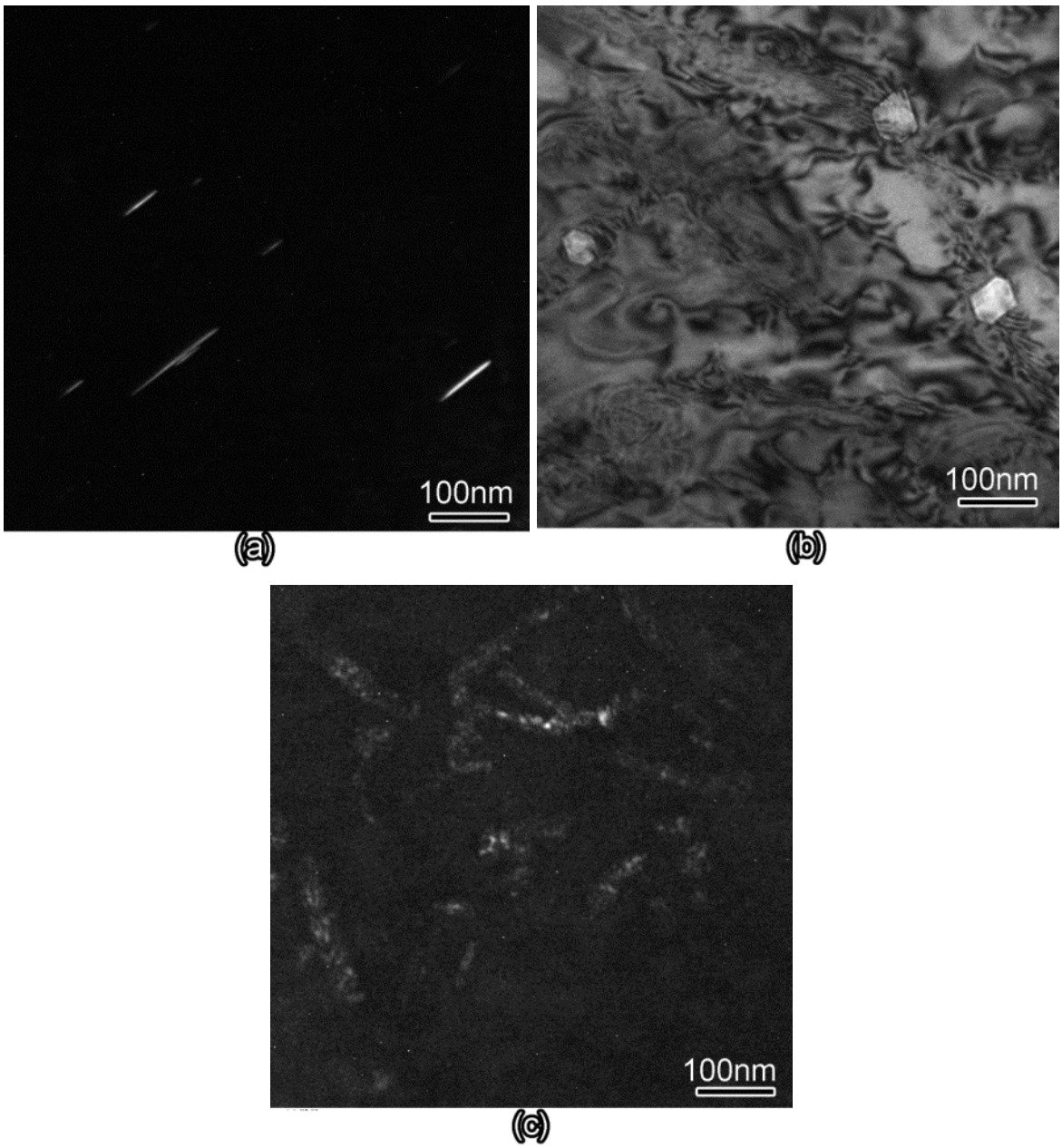

Fig. 58. Irradiated microstructure of HIP AM 800 irradiated by proton to 2.5dpa at 360°C (a) loop(b) void (c) γ′ precipitate.

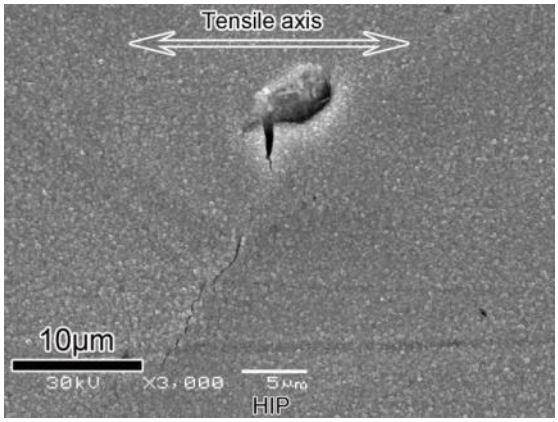

Fig. 59. SEM micrographs of irradiated area (2.5dpa) of the tensile bars of HIP AM 800 strained to 4% in simulated BWR NWC.

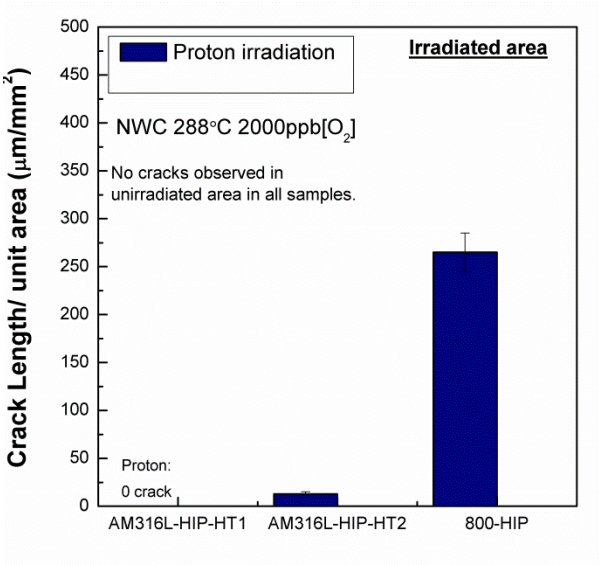

Fig. 60. Cracking suspectibility of AM 316L and 800 at the same processing condition.

Table 7. Crack data of AM or forged 316L to a dose ~ 2.5 dpa by proton or 100dpa by heavy ion and strained to ~ 4% in BWR NWC environment.

Alloy (dpa) (ε)	**Area**	**Number of cracks**	**Yield Stress (MPa)**	**Average Crack Length* (μm)**	**Crack density (#Cracks /mm^2)**	**Crack Length/unit area (Avg. length x density) (μm/mm^2)**
AM 316L-HIP (2.5dpa, 3+4.5%)	UIA	0	185 ± 7	0	0	0
	IA	0		0	0	0
AM 316L-HIP (100 dpa, 3+4%)	UIA	0	184 ± 3	0	0	0
	IA	7		10 ± 1	8 ± 0.1	74 ± 7
AM 316L-SR-PD (2.5 dpa, 4.3%)	UIA	0	421 ± 17	0	0	0
	IA	1		6.1	1.04	6.35
AM 316L-SR-PD (100 dpa, 4.25%)	UIA	0	472 ± 9	0	0	0
	IA	7		12 ± 2	8 ± 0.1	91 ± 16
AM 316L-SR⊥PD (2.5 dpa, 3.8%)	UIA	0	412 ± 21	0	0	0
	IA	35		7 ± 1	38 ± 0.2	272 ± 27
AM 316L-SR⊥PD (100 dpa, 4.0%)	UIA	0	479 ± 17	0	0	0
	IA	50		7 ± 1	54 ± 0.3	378 ± 41
Forged 316L (2.5 dpa, 4%)	UIA	0	203± 10	0	0	0
	IA	50		9 ± 2	38 ± 1	342 ± 46
AM 800 (2.5 dpa, 4.25%)	UIA	0	215± 11	0	0	0
	IA	44		6.5 ± 0.6	47 ± 0.3	308 ± 28

8.4. Conclusions on irradiation studies

1) Irradiation induced voids, loops, and γ′ precipitates were observed in all the material conditions. HIP AM 316L showed better irradiation tolerance and the best swelling resistance after proton irradiation.

2) Stress relieved AM 316L exhibited a significant increase in susceptibility to SCC following irradiation and is comparable to that of conventional forged 316L.

3) HIP AM 316L has lower IASCC susceptibility than conventional forged 316L.

4) HIP of AM Alloy 800 performed much worse in irradiated microstructure and IASCC resistance than that of 316L at same processing conditions.

9. AM Process Optimization and Improvement

9.1. Effect of different L-PBF processes (heats) on the SCC growth rate

Like wrought 316L SS, the SCC response of AM 316L SS also shows heat-to-heat differences, which was mainly contributed by the resulted microstructure from the process. Fig. 61 shows the heat-to-heat comparison on SCC growth rate for both AM 316L SS and wrought 316L SS. All materials shown in this figure were solution-annealed at high temperature. In general, SCC growth rate of AM 316L SS was similar or slightly higher than the conventional wrought 316L SS. More importantly, AM 316L SCC growth rate spread from $3x10^{-7}$ to $7x10^{-7}$ mm/s. Although the difference is only the factor of two, it suggests a clear effect of process/microstructure on SCC resistance.

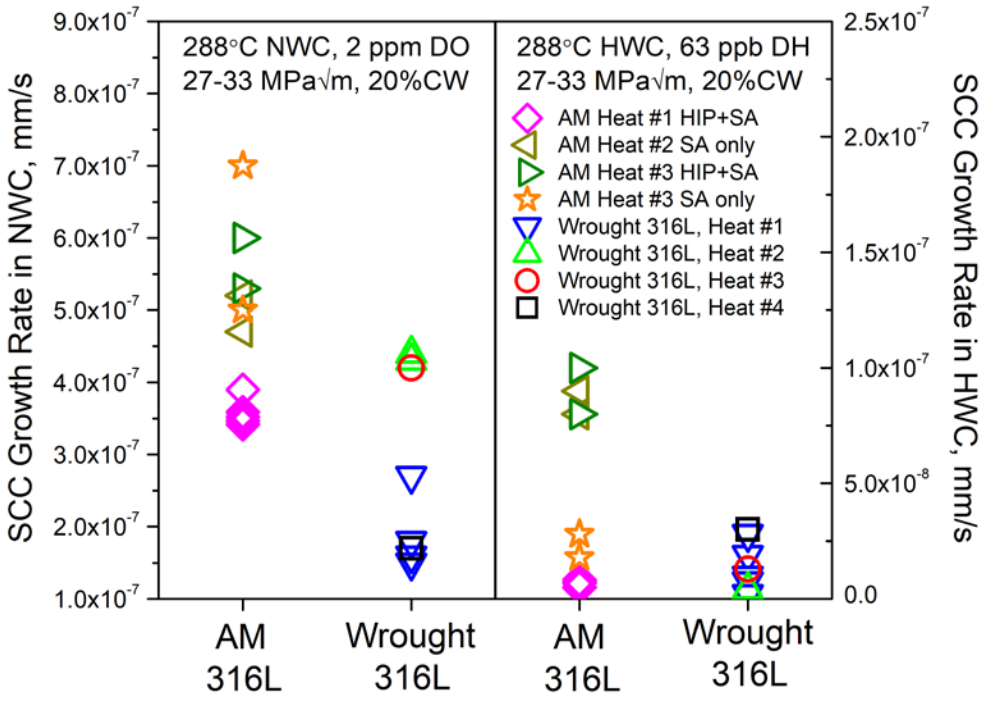

Fig. 61. Heat-to-heat comparison on SCC growth rate (AM 316L SS and wrought 316L SS)

9.2. Optimization of L-PBF for better SCC resistance

By optimizing the L-PBF process, it is possible to control the grain boundary structure to be more resistant to SCC propagation. Fig. 62 shows the results from two different L-PBF laser processes conducted using the same AM 316L powder and the same L-PBF system. The materials exhibited different solidification microstructures. Laser process 2 reduced the SCC growth rate of stress-relieved AM 316L SS by a factor of two. As we discussed earlier, stress-relieved AM 316L SS has an advantage of high yield strength, compared to wrought material. However, due to its worse SCC response, the project concluded that high temperature solution annealing/recrystallization is required for nuclear application, which eliminates its strength advantage. The result in Fig. 62 suggests that it

may be possible to obtain both good strength and reasonable SCC resistance by optimizing the boundary structure using L-PBF process.

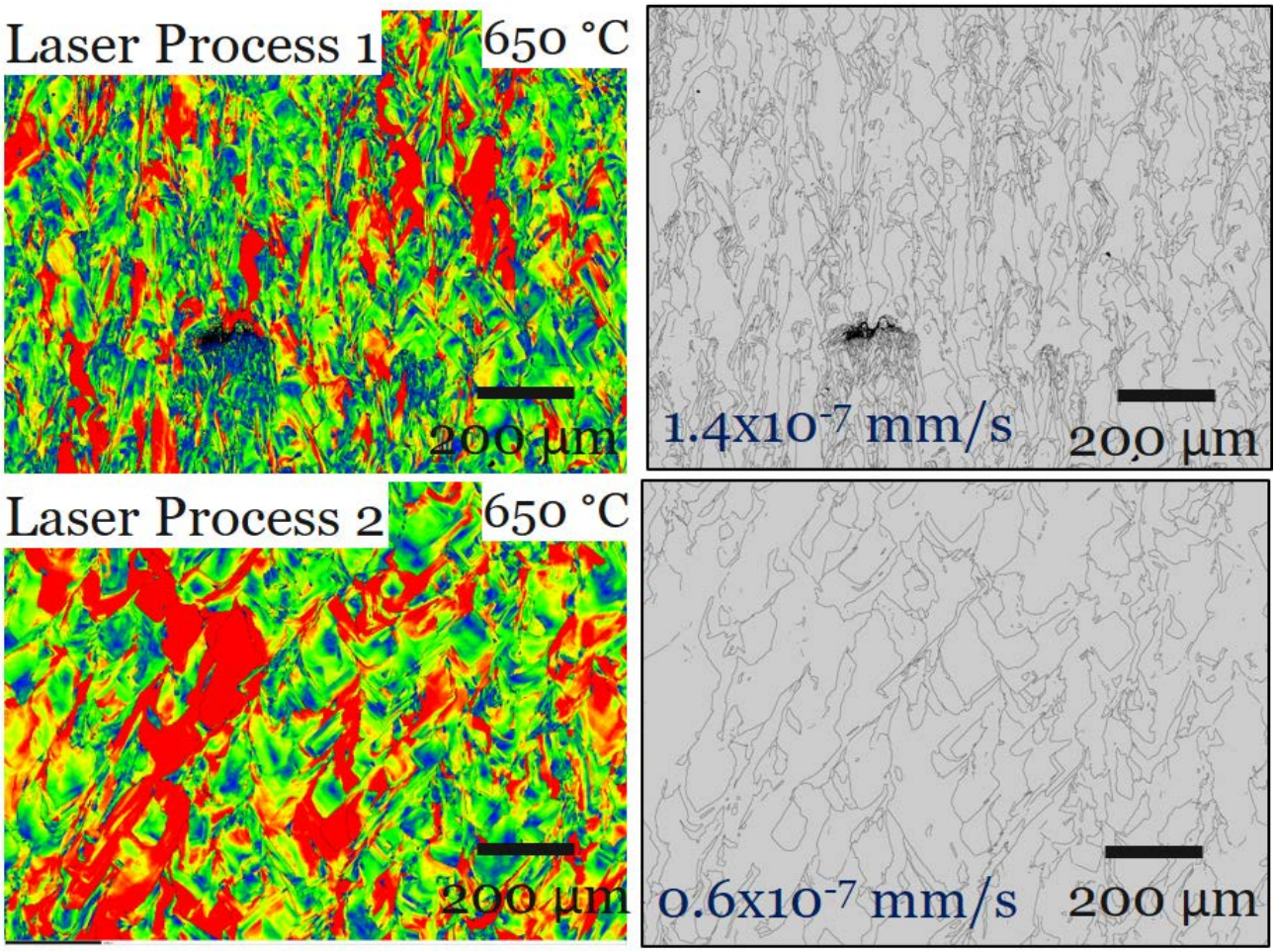

Fig. 62. Process optimization to improve the SCC resistance of AM 316L SS

9.3. AM Alloy 800 with higher Ni and Cr

AM Alloy 800 material was also developed and evaluated in this project. The main purpose of studying Alloy 800 as a candidate for nuclear AM is that Alloy 800 contains increased Cr and Ni content and is believed to be a better material than 316L SS. Meanwhile, the 800 alloy material also provides a good balance between cost and performance. The material was treated by HIP+SA. The heat-treated block was forged by 20% thickness reduction normal to the build direction. The crack grew along the build direction.

Fig. 63 shows the SEM image of AM Alloy 800 after HIP+SA. Most of the material has been fully recrystallized with a relatively large average grain size of 150~200 µm. The material still contained some residual unrecrystallized grains.

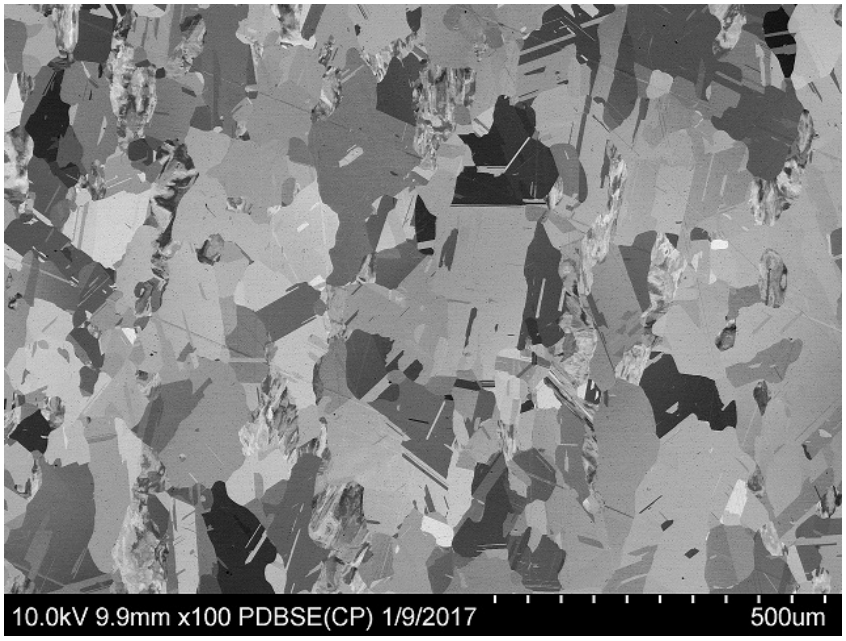

Fig. 63. SEM image of the AM Alloy 800 after HIP+SA (vertical direction is the build direction).

Table 8 shows the tensile properties of AM Alloy 800. The material after HIP+SA showed similar tensile properties and reasonable ductility to its wrought counterpart. The values are also very close to the AM 316L SS after HIP+SA.

Table 8. Tensile properties of AM Alloy 800 (two different build orientations) at room temperature

Material	Ultimate tensile strength (ksi)	0.2% Yield Strength (ksi)	Elongation (%)	Reduction in area (%)
AM Alloy 800, horizontal	89.0	35.8	47	77
AM Alloy 800, vertical	82.5	34.2	54	78

Corrosion fatigue crack growth rate was measured in 288°C NWC environment by DCPD at K_{max}=27.5 MPa√m and a load frequency of 0.5Hz. Table 9 shows the corrosion fatigue crack growth rate under different ΔK. Compared to AM 316L stainless steel tested under the same condition, AM alloy 800 (HIP+SA) showed a slightly slower corrosion fatigue crack growth rate under the same testing conditions.

Table 9. Fatigue crack growth rate of AM Alloy 800 HIP+SA sample in room temperature air (K_{max}=27.5 MPa√m, 0.5Hz)

ΔK MPa√m	**da/dt mm/s**	**da/dN mm/cycle**
22	2.25E-05	4.50E-05
16.5	1.86E-05	3.72E-05
11	9.40E-06	1.88E-05

Table 10 shows the SCC growth rate of the AM Alloy 800 from this project and from the literature for the wrought Alloy 800 [83] tested under similar conditions (constant K=27.5 MPa√m in both NWC and HWC). The AM Alloy 800 under HIP+SA condition showed large variations in crack growth rate, from 6.4E-9 mm/s to 5.5E-7 mm/s. It should be noted that most data fell into the range of 2E-7~5.5E-7 mm/s, which is similar to the literature value. In HWC, two different crack growth rates were observed under similar testing conditions. Wrought Alloy 800 is known to have microstructural variations in the material, which has been attributed for its inconsistency in the reported SCC growth rate values in literature. Compared to austenitic stainless steels, fewer studies have been conducted on Alloy 800 in terms of its behavior in high temperature water. Therefore, it is very difficult to provide a solid conclusion on the SCC performance of AM Alloy 800 tested in this project. But still, we can conclude that the AM Alloy 800 tested in this project behaved similarly to its wrought counterpart. In the fracture surface characterization, we discuss why the crack growth rate varied so much for Alloy 800.

Table 10. Comparisons in SCC growth rate of AM Alloy 800H (HIP+SA) and wrought Alloy 800H at 288 °C NWC under constant K=27.5 MPa√m

Material	**K MPa√m**	**NWC mm/s**	**HWC mm/s**
AM Alloy 800	27.5	2.00E-07	--
AM Alloy 800	27.5	6.40E-09	--
AM Alloy 800	30	4.00E-07	3.00E-07
AM Alloy 800	31	3.20E-07	1.40E-08
AM Alloy 800	33	5.50E-07	--
Wrought Alloy 800 [83]	27.5	1.70E-07	--

Fig. 64 shows the cross-sectional optical image of the crack in the AM Alloy 800 (HIP+SA) specimen. After the fatigue precracking, the crack exhibited a clear intergranular cracking feature. The grain boundaries were clearly shown in the material. The grains were deformed by the forging process, which may be due to the difference in the forging direction relative to the build direction.

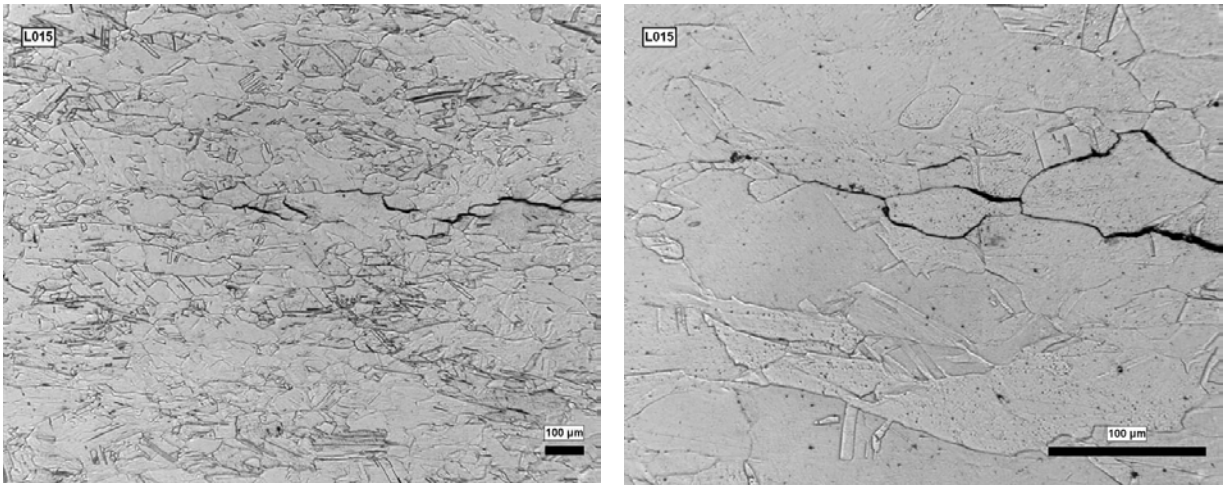

Fig. 64. Cross-sectional optical image of the stress corrosion crack on the AM Alloy 800 (HIP+SA) after etching

Fig. 65 shows the picture of the alloy 800 SCC fracture after testing. The crack front is uneven across the specimen. The non-uniform crack propagation in the SCC specimen is generally observed on weld materials or low alloy steel/carbon steel materials, which may be attributed to the possible microstructure variations in the material. Additional work is needed to understand the microstructure, and further optimize the AM Alloy 800 manufacturing through the laser process and heat treatment.

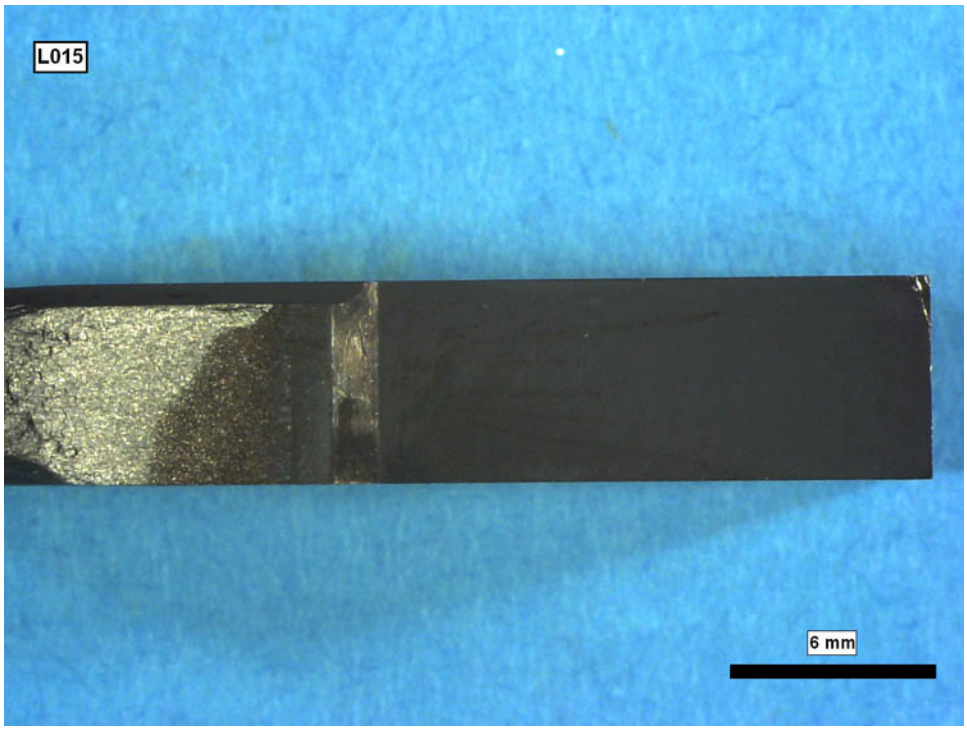

Fig. 65. Optical view of the fracture surface of AM Alloy 800 (HIP+SA)

9.4. Is hot isostatic pressing necessary for stress corrosion cracking?

In Section 6.6, the comparison between low porosity and high porosity heats suggests the increasing in porosity and size may increase SCC susceptibility. However, as shown in Table 4, AM 316L, with optimized L-PBF process, generally exhibits reasonably good density. HIP does not influence considerably the defect size and distribution. Based on the cost analysis of the component demonstration which will be shown in the next section, the cost of HIP is roughly 10-15% of the total AM component cost. Here, we need to understand if HIP can be removed from the manufacturing process of AM 316L SS component to save cost.

Table 11 shows the effect of HIP on the SCC growth rate of a commercial grade AM 316L SS with an optimized L-PBF process. There was no difference observed in CGR between HIP'ed and non-HIP'ed materials. It should be noted that the data here is still limited and more work should be done to confirm whether HIP is necessary for the conditions where high cycle fatigue is not expected. But this result, along with other literature data on cast materials where porosity was also present, suggests that microstructural defects may play a more important role in corrosion cracking than macro defects like micropores. HIP may not be needed for nuclear components in which the most important damaging mode is stress corrosion cracking.

Table 11. The effect of HIP on the SCC growth rate of a commercial grade AM 316L SS with optimized L-PBF process

Tested Materials	CGR (mm/s)
AM 316L, HIP+SA	3.6×10^{-7}
AM 316L, SA only	3.8×10^{-7}
Wrought with SA	$2\sim4 \times 10^{-7}$

9.5. Benefits from laser solidified non-equilibrium microstructure

Fast cooling rate due to laser solidification results in many unique microstructural features that were normally not observed in wrought alloys, including a mix of low to high angle boundaries, fine subgrain cellular dislocation structure, oxide nanoparticles, element segregation along boundaries. The disconnected boundaries structure was expected to be beneficial to SCC resistance. And other nanoscale subgrain features were considered as sink-type features, which should help irradiation resistance.

However, as observed in this project, the stress-relieved AM 316L SS, which possesses all these microstructural features in the material, exhibited worse SCC growth rate, irradiation response, and IASCC susceptibility. Therefore, non-equilibrium microstructure created by L-PBF does not guarantee better nuclear properties. A careful control of those features, such as boundary structure, nano oxide density and stability, and boundary segregation, is needed if improved nuclear properties are desired. Fig. 62 gives a perfect example how SCC resistance can be improved by modifying grain boundary network using different laser process parameters. The material in Fig. 62 is expected to have both better strength and SCC resistance. More stable nano oxide can also be achieved by introducing better oxygen getter than Si. This project planned to create an ODS stainless steel during laser process. The first attempt failed due to the oxygen control issue. Later, due to GE's organizational structure change in early 2017, this ODS approach was not able to be executed.

However, some later observations suggested that SCC susceptibility can be significantly reduced by modifying the local microchemistry and grain microstructure through new material design and L-PBF process. With better understanding the relationship among process, microstructure, and nuclear properties, L-PBF process has a potential to create material which has exceptionally better material performance than its conventional wrought processed counterpart.

10. Nuclear Specification Development, Component Demonstration, and Commercialization at GE Nuclear

10.1. Nuclear Specification and Regulatory Approval

The specification for materials and parts in nuclear power plants is dependent on the operating environment, duty, and regulatory requirements (i.e., the intended application). The operating environment of a part can vary based on temperature, chemistry and radiological conditions. Duty can vary based on loading. Regulatory requirements can vary based on safety significance.

The following breakdown of application is commonly applied for nuclear power plants:

1. Operating environment
    a. Fuel
    b. Reactor internals
    c. Non-reactor Internal
2. Duty
    a. Nuclear pressure boundary (ASME BPVC Section III Subsection NB - Class 1 Components)
    b. Non-pressure boundary
    c. Application specific duty
3. Regulatory Requirement
    a. Safety-related (relied upon for design-basis events)
    b. Non-safety

316L Austenitic Stainless Steel is widely used in nuclear power plants. Independent of application, the material will be governed by an ASTM specification. 316L (wrought and cast) has a set of ASTM specifications depending on the product form (e.g., ASTM A240, A479, A276, A351). The base ASTM specification for AM 316L by L-PBF is ASTM 3184-16, “Standard Specification for the Additive Manufacturing Stainless Steel Alloy (UNS S31603) with Powder Bed Fusion”.

The ASTM 3184-16 manufacturing plan requires process-specific qualification. For the purpose of further discussion this is called the Materials Baseline. The Materials Baseline establishes defined material which has been produced from a specified powder, on a specified machine, with a specified set of machine parameters, and post-treated in a specified manner. The defined material then can be characterized based on its microstructure, tensile properties, toughness, fatigue, and stress corrosion cracking performance.

The Materials Baseline serves the following purposes:

1. Provides the source of data for a specific application (e.g. ASME Code Case)
2. Provides a reference for build plate specific testing. If test results can be shown to consistent with the Material Baseline, the expanded set of properties from the Material Baseline can be assumed to apply.
3. Provides a reference for qualification of a new machine or a new set of machine parameters. If test results can be shown to consistent with the Material Baseline, the expanded set of properties from the Material Baseline can be assumed to apply.

As an example of a Material Baseline for the material characterized in this program, Table 12 provides a set of critical characteristics.

Table 12. AM 316L Material Baseline Data / Specification

Parameter	Baseline Data	Specification
Powder – Carbon	0.018	0.030 max
Manganese	1.31	2.00 max
Phosphorous	0.02	0.045 max
Sulfur	0.004	0.030 max
Chromium	16.2	16.0 – 18.0
Nickel	10.4	10.0 – 14.0
Molybdenum	2.02	2.00 – 3.00
Cobalt	0.042	0.05 max
Machine	EOS-290	EOS-290
Post-treatment Step 1 – Stress Relief	Within Spec	1900°F min, 2 hrs -5/+15 min, Inert, cool to 800°F
Step 2 – HIP	Within Spec	2050-2125°F, 4 hrs ±1hr, 14.5 ksi, Inert, cool to 800°F
Step 3 – Solution Anneal	Within Spec	1950°F min, 1-2 hrs, Inert, cool to 800°F in <10min, quench to 400°F
Microstructure	Within Spec	Characterized as consistent or better than the microstructure described as adequate for SCC, FCG, and IASCC behavior
Mechanical (Room Temperature) UTS (ksi) X,Y,Z	92.7, 93.5, 87.0	90 ±10
Yield Strength (ksi) X,Y,Z	40.8, 43.3, 41.7	40 ±10
Elongation (%) X,Y,Z	70, 62, 70	70 ±10
Rockwell Hardness	79, 80, 80	80 ±10
Fatigue Crack Growth mm/cycle (0.5Hz)	4.64E-5	4E-5 to 8E-5
IGSCC – 2 ppm O_2 (mm/s)	5.6E-7	7E-7 max
63 ppb H_2 (mm/s)	9E-8	1E-7 max
IASCC – 2 ppm O_2 (μm/m^2) 5 dpa Proton	11	50 max

Fig. 66 illustrates the process for application and regulatory approval. For reactor internals, the BWRVIP-84 and ASME Code Case paths have additional data requirements specific to these applications. They also require review and approval (EPRI for BWRVIP-84 and ASME for Code Case). For fuel, applications are demonstrated through a lead-use process (LUA is Lead Use Assembly). A LUA report is provided to the customer including justification of material adequacy with reliance on the Material Baseline and application specific testing. The non-internals, the

environment will not include threat of irradiation damage or SCC. A non-internal part may have a safety-related function and would require the ASME Code Case. These details have been discussed with the US NRC (Reference 3.2 and 3.3).

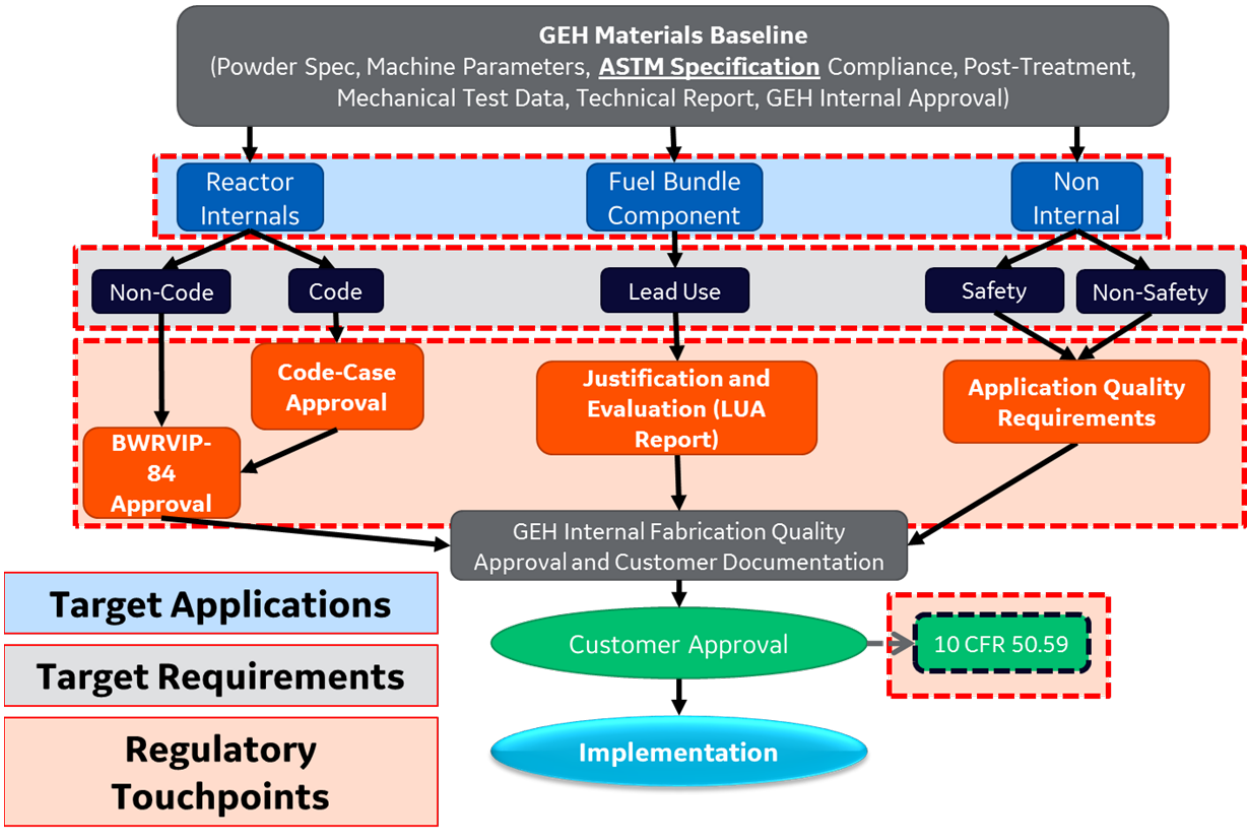

Fig. 66. Application Specific L-PBF AM Process Implementation

10.2. Fabrication of a Nuclear Component

10.2.1. Nuclear Component Design Process

Based on discussions with GE Global Research and GEH the fuel debris filter has been chosen as the target component for nuclear component fabrication and evaluation. The fuel debris filter is inserted into the bottom of the BWR fuel bundle (see Fig. 67).

Fig. 67. BWR Fuel Bundle with Debris Filter

The debris filter was chosen because it challenges the capabilities of the L-PBF process, leverages the strengths of the L-PBF due to its complexity, and is being seriously evaluated as a part that may serve the nuclear fuel market in the future.

The process parameters and alloy chosen for this demonstration are Solution Anneal as described in 2.1, and HIP. Although not leveraging the simplification of the anneal-only approach or the alternative improved alloy options, this alloy and post-treatment has demonstrated acceptable properties for nuclear application.

The critical characteristics of the filter are as follows:

A. The filter can effectively remove small wires (0.02” OD x 0.2” length)
B. The filter pressure drop is approximately the same as current (Defender^{TM}) filter
C. The filter is mechanically able to withstand the pressure loading of water flowing into a fuel bundle.

Items A and B act in opposite direction of design because effective filtering requires a tight grid while lower pressure drop may require a more open grid. Characteristic C requires a grid matrix strong enough to withstand the loading.

An effective filtering design for maximizing debris removal was found to be a perforated plate with round holes. Based on alternatively manufactured prototypes, scaled testing, and computational flow dynamics, a design was developed that was expected to meet the critical characteristics. These designs were manufactured with L-PBF and tested. Fig. 68 shows a magnified view of the hole pattern. The 1 mm holes were about 20% smaller than the model specification. As is common with this process, the top of the holes experienced a droop as the preceding layer lacked the ability to support the melt. The holes also had a large surface roughness. The pattern failed to achieve the pressure drop goal.

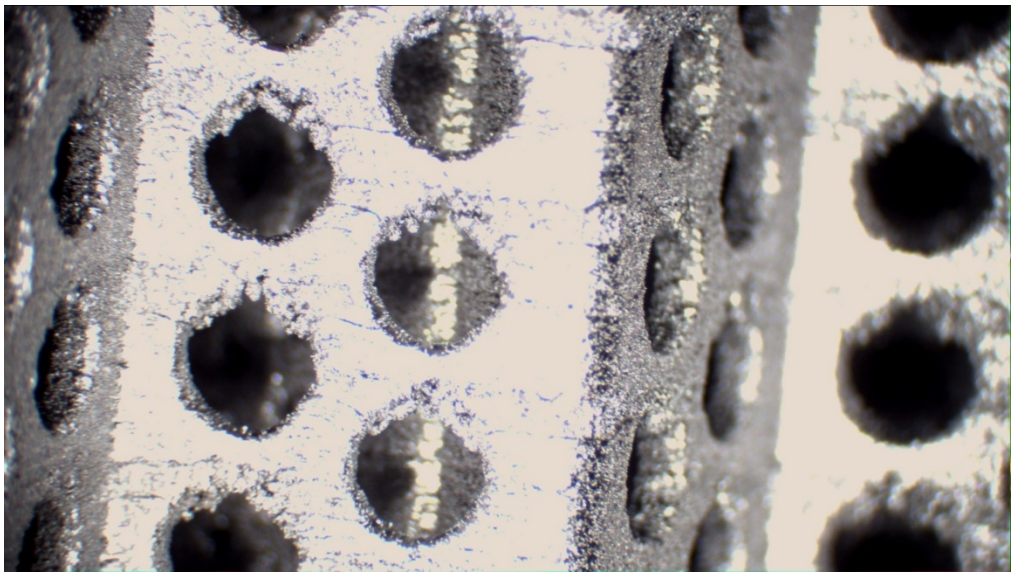

Fig. 68. Hole Pattern with 1 mm holes

To determine the limitations of the hole, a matrix of hole patterns was built. Fig. 69 provides the impact of building holes when design model applied a teardrop shape in the axial direction of the build.

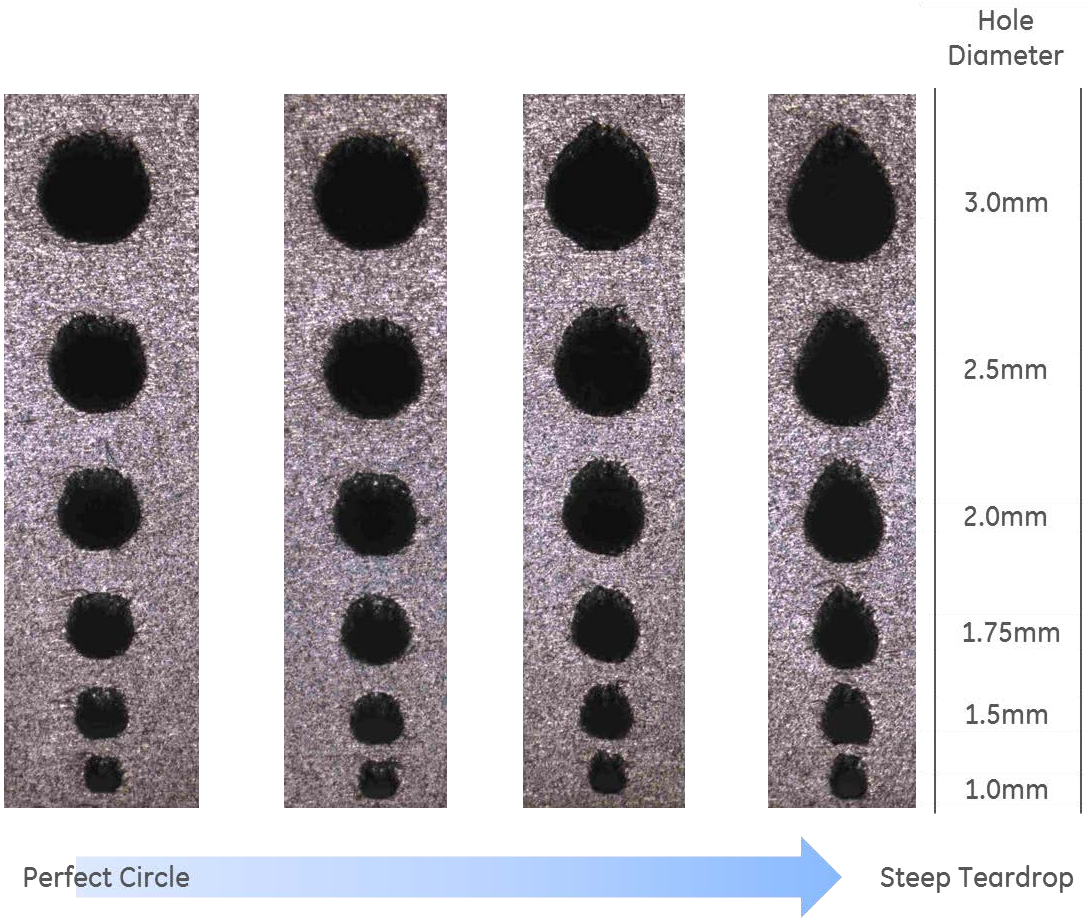

Fig. 69. Hole Pattern Quality Study

After reviewing these results, it became clear that adjustment to a teardrop shape would not provide the required open flow area to meet the pressure drop requirement. A triangular pattern had been shown to provide a more exact dimension hole with cleaner edges. It was decided to move to a diamond pattern (Fig. 70). The pattern was designed to be elongated in the axial direction to provide the necessary support during the build. The filter was built in 2 different planes. Building the filter on the X,Y plane (filter x,y,z is approx. 120mm x 120mm x 15mm) would allow fewer filters on the build plate (approximately 4) but would allow the elongated diamonds on the Z direction. Building the filter on the side would allow more filters on the build plate. This is a more cost-effective approach to the L-PBF process.

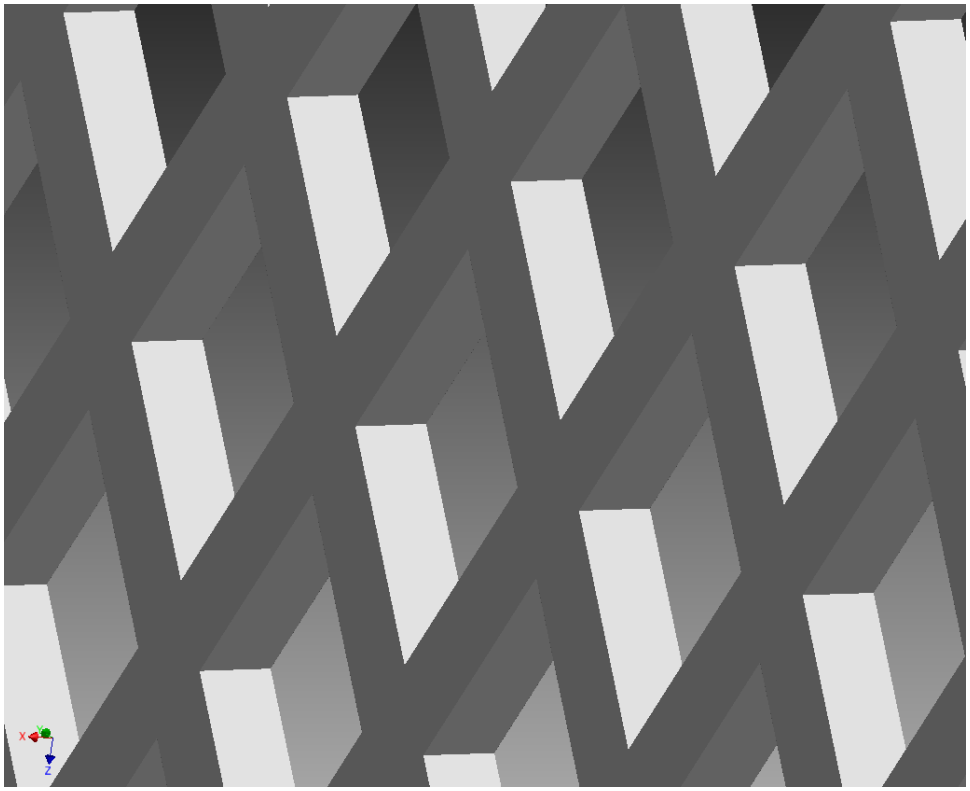

Fig. 70. Filter Concept with Diamond Pattern

10.2.2. Nuclear Component Production

The debris filter is a Fuels component and subject to the requirements of a LUA part. The production build process is applied in a manner that will support all the quality requirements necessary for reactor deployment. In fact, the parts and the associated quality records are ready for lead-use deployment.

The production build includes the following provisions:

1. The powder defined by the Materials Baseline is applied
2. The machine and machine parameters defined by the Materials Baseline are applied
3. The post treatment defined by the Materials Baseline is applied
4. The build plate includes 4 vertically oriented filters and tensile bars in the x, y, z direction for tensile testing in accordance with the ASTM specification. One of the filters is for destructive testing.
5. Materials and process traceability is maintained throughout.

Fig. 71 shows the resulting build plate.

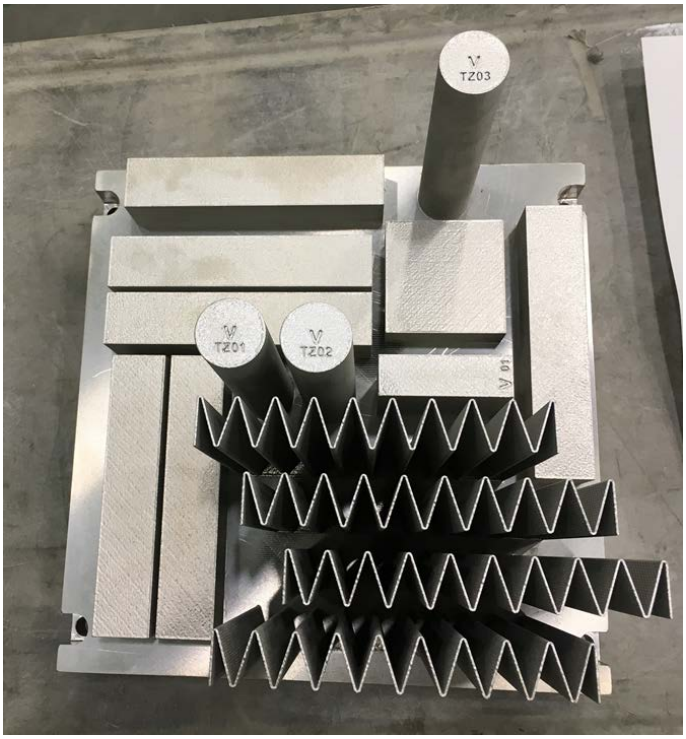

Fig. 71. Build Plate Layout

10.2.3. Nuclear component testing

Microstructure and Mechanical Testing has been completed. Fig. 72 and Fig. 73 show photomicrographs from the debris filter. The microstructure is consistent with the Materials Baseline. Grains show some elongation along the build direction but the material was sufficiently recrystallized to provide adequate IGSCC and IASCC behavior. Fig. 72 shows small beads on the top edges of the diamonds that are not uncommon for a L-PBF build. These beads are not considered a risk to structural integrity or a source of debris if they break off considering their size.

Dimensional inspection is a unique challenge for L-PBF. Overall dimension and large feature dimensions can be accomplished with traditional techniques (e.g., CMM). The overall dimension can be held to tolerances similar to traditional parts. On average, the AM parts are slightly larger than the nominal CAD model. Internal features and small features (e.g., filter diamonds) are often not accommodated with traditional inspection techniques. Blue Light laser scanning and Computed Tomography (CT) can produce point clouds of the structure which can be compared to the CAD model to detect variances. CT can identify structure in part interior. These techniques have an accuracy of about 0.2 mm. Fig. 74 shows a CT scan of a more complex filter design and variances found relative to the model. Fig. 75 is from a Blue Light scan of final nuclear component. Blue Light inspection provides a good representation of overall part geometry and any warping on a global scale. CT scanning provides more accurate dimensional measurements for checks of smaller features and internal geometries.

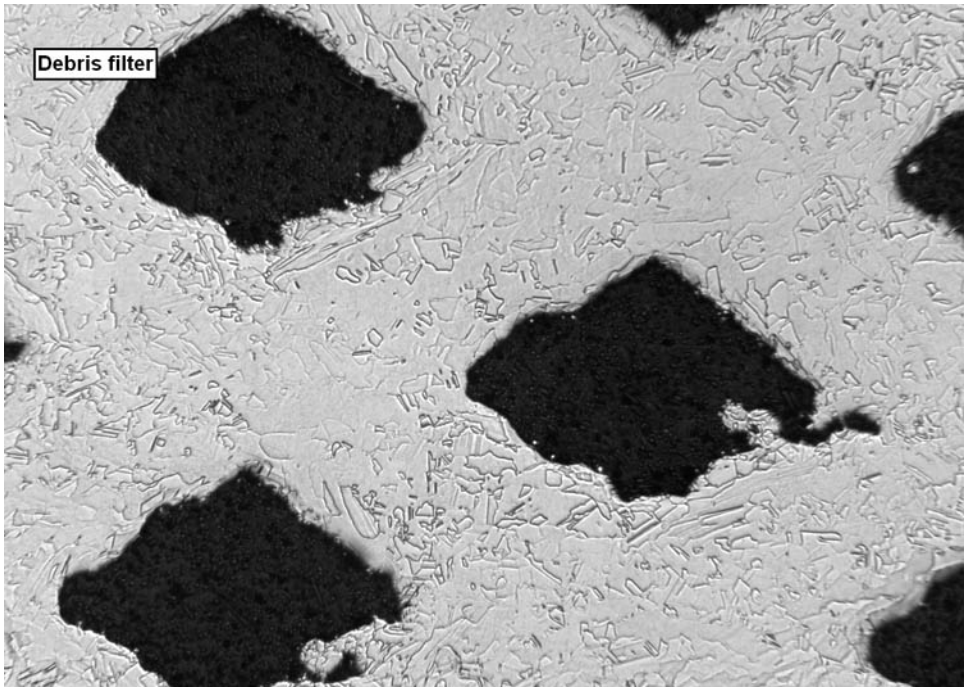

Fig. 72. Side View of Filter (build direction left to right)

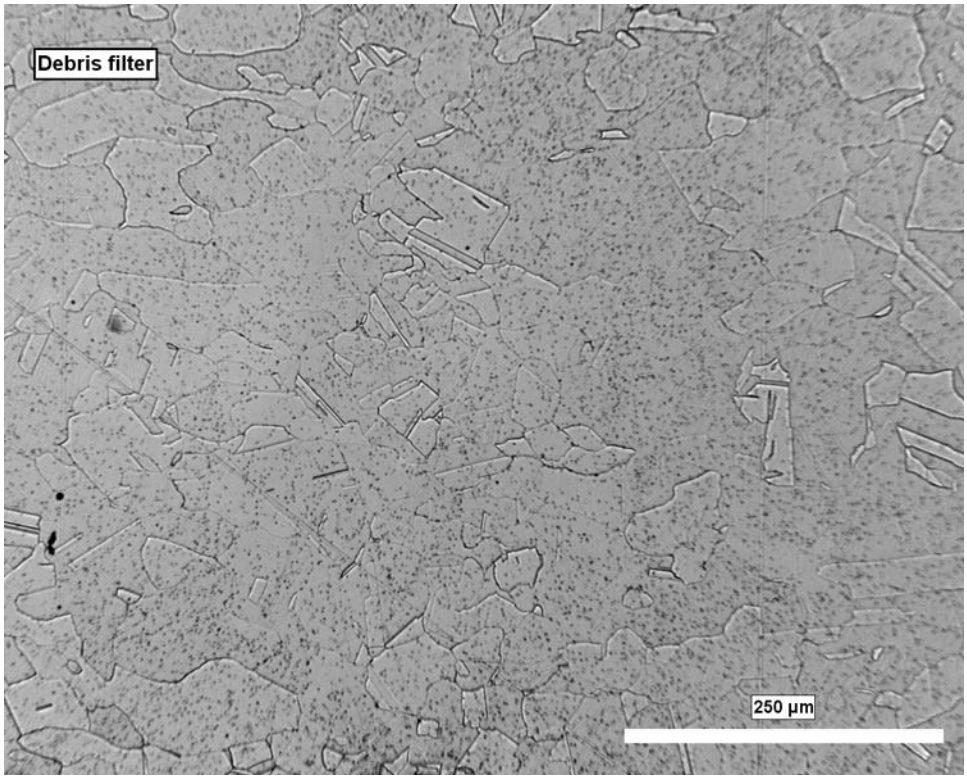

Fig. 73. Top View of Filter

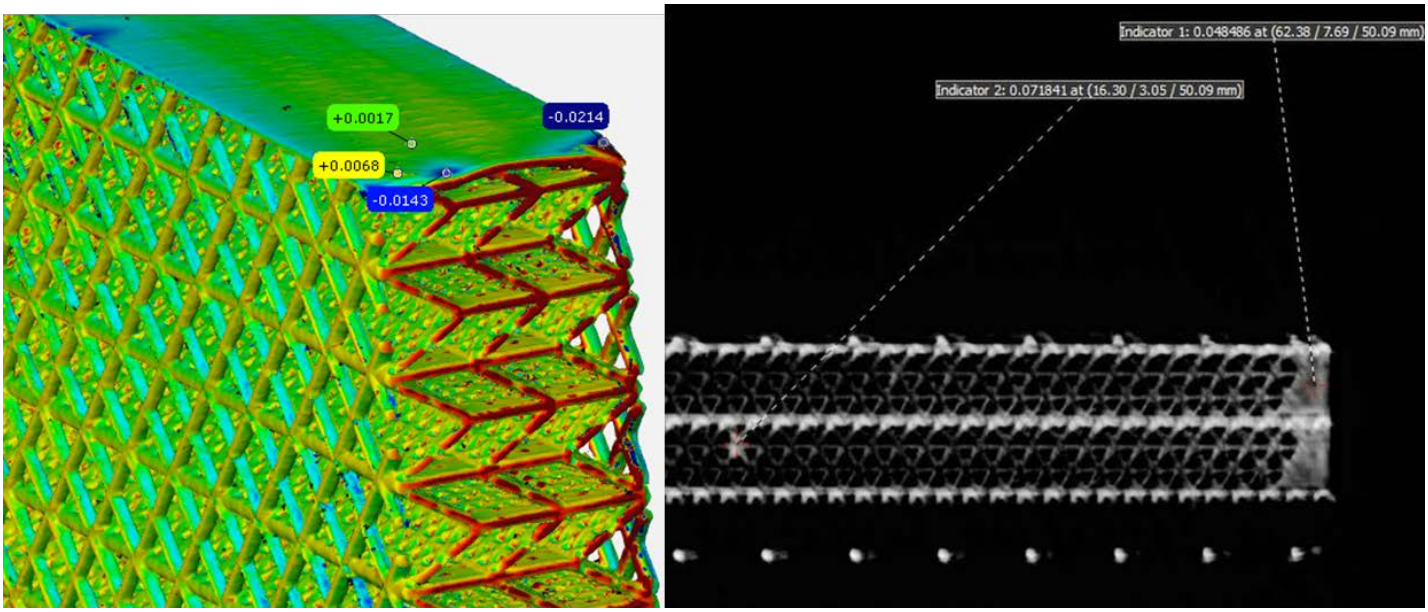

Fig. 74. CT Scan of Design Interior (red is outside allowable tolerance)

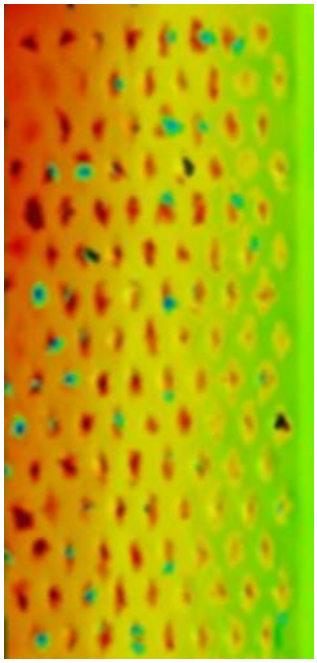

Fig. 75. Blue Light Scan of Design Exterior (red is outside allowable tolerance)

As the smaller internal features can be challenging to inspect and meet tolerance via an approved nuclear inspection process, an alternative criterion may be required to demonstrate adequacy of the application. In the case of the debris filter, the filter pressure drop can serve as a measure of overall "openness" of the flow path. This is a critical characteristic of the filter as has been described in Section 2.2.1. In the case of the 3 production filters, the dimensionality would be considered outside tolerance but it can be shown to meet the pressure drop requirement, filtering requirement, and structural adequacy via engineering testing.

10.3. Commercialization

10.3.1. Production process

The production process for an additive debris filter has multiple steps, but 3 main processes:

The process flow map for production, color coded by these three main processes, can be seen in Fig. 76. This process is representative for most parts including the debris filter. The "dedication" step is unique to nuclear quality assurance.

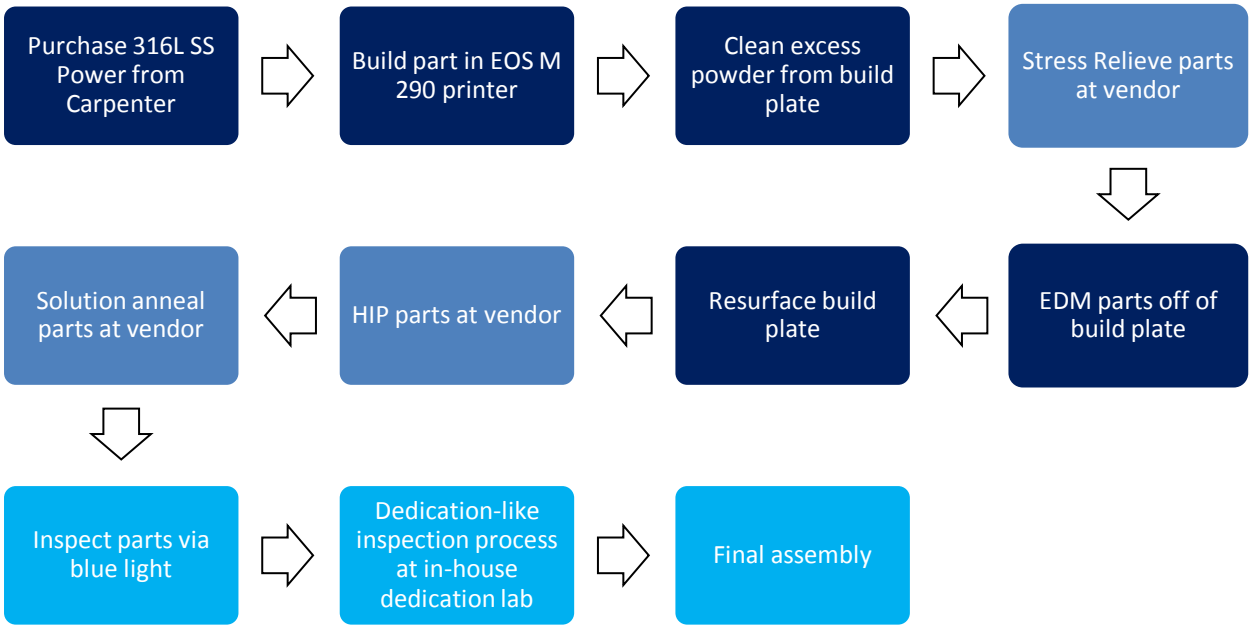

Fig. 76. Additive Production Flow

10.3.2. Filter production cost model

A model was prepared to estimate the cost per part from the cumulative cost associated with each step of the production process. A new production line is fully equipped except for HIP chamber. The cost estimate is based on the assumption that the target production volume for additive manufacturing debris filters is 1,000 parts per year. The printer assumed is an EOS 290 M. For the debris filter, 14 parts can be printed on each build plate. The build time per job is 3.5 days. It is assumed that powder must be unused or virgin. Printer utilization is capped at 65% to account for downtime to load and clean materials between builds. The costs associated with the construction of this facility and the overhead cost of the building are excluded from this analysis. All capital investments are assumed to have a 7-year depreciation.

The total cost to manufacture nuclear debris filters in a new fully-equipped production line is approximately $700 per part. The breakdown of cost is shown in Fig. 77.

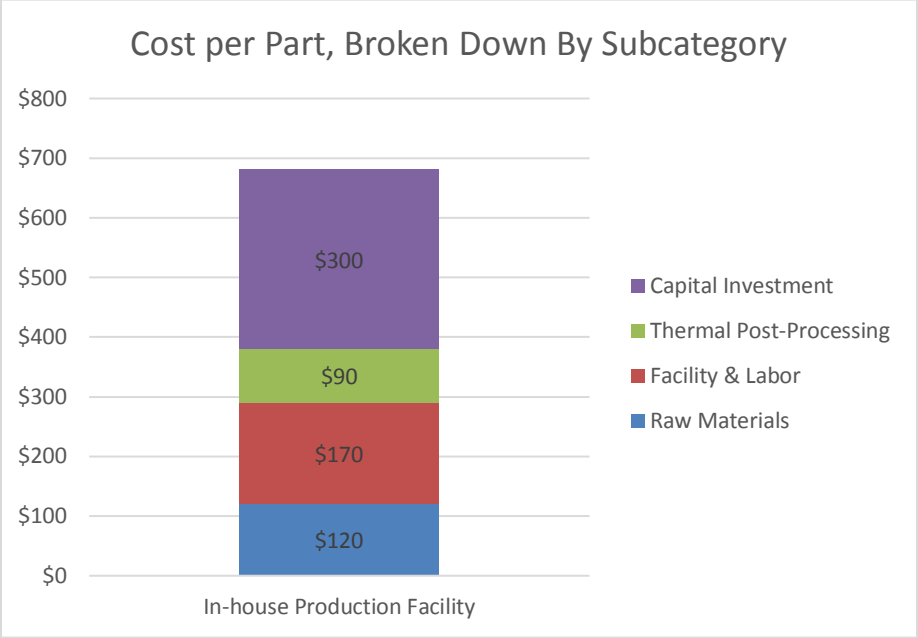

Fig. 77. Debris Filter Cost per Part

10.3.3. Filter capital costs

The production facility (excluding HIP chamber) requires a capital investment in 6 major systems, as outlined in Table 13.

Table 13. Capital Cost Breakdown

System	Reason	Capital Investment
Direct Metal Laser Melting Printers	To print parts	$800,000 Two EOS 290 M printers
Power Removal System	To remove excess powder from build plate after printer job is complete	$50,000
Heat Treatment Furnace	To stress relieve the build plate and solution anneal parts	$800,000
Machining Capabilities (Grinder, End mill, EDM)	To EDM final parts off from the build plate and resurface the build plate after the job is complete	$200,000
Bulk Inert Gas Storage System	To flood build chamber and heat treatment furnace	$90,000
Blue Light Inspection System	To measure variance between part and model	$250,000
Total Capital Investment Cost		2.2 MM

Distributing these costs over a 7-year period with the assumption of 1,000 parts produced per year means that the cost per part to finance this investment is $300. This expense is the largest contributor to the overall cost of the part. Filter Raw Materials

There are 3 main categories of raw materials that must be considered for this analysis: the powder; the build plate; and the inert gas supply. The cost of 316L Stainless Steel powder is estimated to be $30 per pound. The debris filter would require 3 pounds of powder per part, costing roughly $90. The cost of build plates (periodic replacement) would add another $30 per part, bringing the total cost to $120. Gas cost is negligible.

To lower this cost in the future, the manufacturer could choose to develop a powder recycling program. If the powder could be used for 10 cycles, it would lower the cost per part for raw materials from $120 to $40. Powder recycling would require qualifying the material made from re-used powder. This has been done successfully in other industries.

10.3.4. Filter heat treatment costs

There are 3 steps included in the heat treatment of 316L for a nuclear debris filter:

1. Stress relief (while still on build plate)
2. Hot Isostatic Press (HIP)
3. Solution Anneal

Stress relief and solution anneal are assumed to be done in-house for the scope of this model; however, given the prohibitively expensive furnace needed, HIP is assumed to be sub-contracted. The most significant cost for heat treatment is HIP at $1200- $2500 per build plate, or $80-$180 per part. As has been shown, material quality is acceptable without HIP but is retained as a material quality risk mitigation protocol applied to many AM applications today.

10.3.5. Filter labor costs

The facility would need to employ the following personnel:

- Printer Technicians,
- Inspection Technicians, and
- Machinists

It was estimated that a printer technician would spend roughly 8 hours supporting each build, the inspection technician would spend 2 hours running automated inspection software, and the machinist would spend 4 hours cleaning the build plate. Assuming an overhead rate of $100/hr for each technician, it would be about $170 of labor per part.

10.3.6. Filter cost summary

When considering investing in a production facility, the depreciation of the capital cost is the largest contributor to the cost per part. Labor is the next largest, followed by the raw material and thermal post-processing (assuming the production volume is large enough to not require paying for a dedicated HIP run). To lower the cost per part as production ramps up, the manufacturer could increase the production volume to increase machine utilization percentages, partner with an existing machining facility to lower the capital investment, qualify the powder to be re-used to lower the raw material cost, or remove the HIP process from heat treatment.

10.3.7. Business case for additive filters

The $700 cost per filter is higher than the existing Defender^{TM} filter, therefore the price of each bundle would need to be increased to ensure profitability. As described in 2.2.1, the additive filter meets all design criteria. Customers have indicated they would be willing to pay more for the

extra level of debris removal provided by the design so the additive design is expected to be profitable. As successful as the design has proven, a similar traditionally manufacturable design was also developed that performs as well and can be made at a significantly lower cost. Therefore, the traditionally manufacturable design will be pursued.

Note that more complex additive designs can be produced at similar cost. Many of the more complex concepts are clearly not manufacturable in a traditional manner. It ultimately becomes a question of performance and associated pricing opportunity. Another option to find a favorable balance is to build the lower tie plate assembly in a single build. Figure 2-2 shows that the filter is inserted to the lower tie plate and, once inserted, a cover plate to welded to secure the filter and close the tie plate opening. It is possible that the entire lower tie plate and filter could be fabricated in a single build. This would lower overall assembly cost and might tip the scale on profitability.

10.3.8. Additive part commercial summary

Considering all the factors mentioned relative to debris filter manufacturing cost today, it is a challenge to competitively produce AM parts. Capital cost in particular, will continue to decrease as the technology grows and expands, changing the cost equation for the debris filter in a few years.

For the proper complex multi-piece assembly, AM can provide a cost reduction by fabricating an assembly in a single build. This opportunity will grow as the machine build capabilities increase.

Designs targeted for AM and driven by performance opportunity are the biggest drivers in the aviation industry and thus provide the greatest opportunities for nuclear. Flow and heat transfer improvements can come from creative shapes buildable without the normal manufacturing constraints. Fuel is the obvious target for LWRs since the designs continue to be improved to optimize performance.

The opportunity related to the build speed should not be underestimated. Emergent parts needs may be discovered during periods of inspection or maintenance. The AM can often produce a part faster than traditional manufacturing and this could provide significant value if the reactor startup is delayed due the need.

A key objective of this program was to develop 316L with nanostructures having improved material properties and irradiation resistance. It was determined that the stress relieved-only material would not be acceptable but the solution annealed-only material would provide properties as good or better than wrought material. The data obtained has not identified a material to replace high performance alloys like Nitronic 50 or Inconel Alloy X750 but evidence does exist to show that such a goal is achievable.

10.3.9. Additive part commercialization enablement

To commercially deploy AM 316L the following activities are considered valuable if not critical:

1. Obtain all the required data and obtain approval for an ASME Code case for pressure boundary components (ASME BPVC Section III Subsection NB - Class 1 Components). This is regarded as the strongest materials basis for nuclear application.
2. Obtain neutron irradiation data. DOE NSUF Program CFA-16-10393 Irradiation Testing of LWR Additively Manufactured Materials. The data will be to approximately 0.7 dpa and will be difficult to compare to the proton IASSC data at 5 dpa.

3. Develop a quantitative method of determining if microstructure will provide adequate irradiation resistance (e.g., IGSCC). It is expensive and time consuming to perform IGSCC tests on materials produced on each build plate. Based on microstructure evaluation the level of grain recrystallization, grain orientation, and oxide deposition can be evaluated and quantified for acceptability. This technique requires research and development.
4. Material operating in an LWR and then inspected can provide valuable insights on environmental effects.

With the right enablement and commercial business opportunity, there is optimism that the material can be used in production parts within 2 years.

11. Project Summary and Achievements

This project completed all the tasks in the proposal and achieved all the original goals. This is the first study in the world which delivers a comprehensive understanding of the nuclear related properties of AM austenitic stainless steel and its process-structure-property relationship for nuclear applications. These properties include microstructure, tensile properties, Charpy impact toughness, SCC, corrosion fatigue, irradiation effects, and IASCC. The research greatly contributes to develop nuclear specifications for both non-critical and critical applications. In addition, the research also provides suggestions to the required procedures of L-PBF process and post treatment to improve structural integrity and reduce the manufacturing cost. Based on the findings of this project, GE has demonstrated the technology on its Defender™ advanced debris filtration system which currently needs a re-design. Through the produce, GE completed the cost analysis for its commercialization. This project has been well communicated with regulatory agency (US NRC), standard body (EPRI), nuclear industries and universities.

11.1. Material development

A good understanding of nuclear related material properties and the relationship among process, microstructure, and properties are the keys for nuclear industry to adopt a new technology. The project has made significant progress in the following areas:

1) Powder development, microstructure control and process optimization for AM 316L stainless steel, AM Alloy 800, and the modification of AM SS including boundary structure modification and ODS.

2) High resolution characterization to understand the hierarchy of the AM stainless steel, such as grain/dendrite structure, strain distribution, boundary structure, segregation, precipitation, etc.

3) Tensile properties of AM SS at both room temperature and reactor operating temperature are similar or better that its wrought counterpart.

4) Comprehensive stress corrosion cracking growth study of various heats of AM 316L stainless steel, AM Alloy 800 and modified AM SS were studied, including the effects of microstructure, heat treatment, stress intensity factor, cold work, crack orientation, oxidizing vs. reducing conditions, and porosity. High temperature post manufacturing treatment above solution annealing temperature is required for nuclear applications. HIP may not be needed if the as-built part shows good density. Retained unrecrystallized grains in AM part may not affect SCC resistance if the part goes through the high temperature annealing treatment.

5) Comprehensive corrosion fatigue study of AM 316L stainless steel. AM 316L SS shows similar corrosion fatigue response to its conventional forged material.

6) Oxide inclusions in AM SS influence Charpy impact toughness of AM 316L stainless steel.

7) Comprehensive study of proton and heavy ion irradiation effect and irradiation assisted stress corrosion cracking was conducted on AM materials. Based on the results, the HIPed AM

316L SS shows better irradiation tolerance and IASCC resistance than both stress-relieved AM 316L SS and wrought 316L SS.

8) Non-equilibrium microstructure on AM 316L SS, including mixed low to high angle boundaries, subgrain cellular dislocation structure, nano oxides, does not guarantee a benefit to SCC and irradiation resistance. However, this research suggests, with better understanding the relationship among process, microstructure, and nuclear properties, L-PBF process has a potential to create material which has exceptionally better performance than its conventional counterpart.

Some key recommendations to AM manufacturing process are summarized below, to improve material structural integrity and save manufacturing cost.

1) High-temperature annealing of AM SS component should be required for any critical nuclear applications.

2) If the component has been post treated above solution annealing temperature, some retained unrecrystallized grains in the material are acceptable for most nuclear related properties, including mechanical properties, SCC, and corrosion fatigue. At this moment, we still have not evaluated the effects of retained unrecrystallized grains on the irradiation properties.

3) HIP may not be needed if the as-built part exhibits reasonably good density.

4) Oxygen control during powder and L-PBF process is important for impact toughness and environmental cracking. When powder recycling is used to save cost, attentions are needed to make sure oxygen is controlled in the used powder.

11.2. Nuclear Specification

The results from the prior 2 years of experimental work were consolidated to form a baseline for GE Nuclear internal AM material specification. The roadmap for nuclear specification and regulatory requirements has been discussed with the US NRC on June 7 (see ADAMS ML17163A266 ML17173A539). US NRC commented on the importance of a strong nuclear quality commercial grade dedication process.

11.3. Nuclear Product Demonstration

The additive manufacturing design and fabrication process was executed with a rigorous nuclear quality assurance (QA) oversight program to produce three nuclear fuel debris filters. These parts were subject to material testing and have the fabrication pedigree to be considered for in-reactor use. The GE Nuclear component inspection and qualification program was adapted and executed for the first time on AM parts. This included supplementing the standard GE Nuclear inspection processes with CT and Blue Light scanning to better characterize additive manufacturing tolerances. The additive debris filter meets all design criteria.

11.4. Commercialization

The cost per part and capital investment requirements for a production scale facility were determined via a mathematical model developed in collaboration with the GE Greenville AMW. The cost per part for the fuel debris filter is still estimated higher than the conventional manufacturing process. But despite the higher cost, customers have indicated they would be willing to pay more for the extra

level of debris removal provided by the design so the additive design is expected to be profitable. As part of the commercialization analysis, a customer with serious interest in using these AM nuclear debris filters in-reactor was identified.

Further reduction in the manufacturing cost can be achieved by implementing the following changes in the manufacturing:

- Capital investment cost per filter will reduce with the improved AM machine.
- Possibility of eliminating HIP process.
- Possibility of recycling raw powder material.

In addition, the value of the nuclear product can be significantly improved if the following can be achieved:

- Ability to produce high value product with a geometry that cannot be achieved by traditional manufacturing, including complex multiple piece component.
- Functional gradient component with the integration of different materials.
- AM material that exhibits much better nuclear properties than traditional material.

The opportunity related to the build speed should not be underestimated. Emergent parts needs may be discovered during periods of inspection or maintenance. The AM can often produce a part faster than traditional manufacturing and this could provide significant value if the reactor startup is delayed due the need.

11.5. Patents and publications

1. Patents

- Xiaoyuan Lou, Martin Morra, "Additive manufacturing method and materials" (filed, patent pending)
- Xiaoyuan Lou, Martin Morra, "Grain boundary engineering for additive manufacturing" (filed, patent pending)

2. Journal papers

- Xiaoyuan Lou, Song Miao, Mallikarjun Karadge, Frederick A. List, Raul B. Rebak, "The nature, origin, and evolution of nano oxide inclusions in austenitic stainless steel made by laser powder bed fusion", Acta Materialia (To be submitted)
- M. Song, M. Wang, X. Lou, G. S. Was, R. B. Rebak, "Radiation Damage and Irradiation-assisted Stress Corrosion Cracking of Additively Manufactured 316L Stainless Steels", Journal of Nuclear Materials (To be submitted)
- Xiaoyuan Lou, Peter Andresen, Raul B. Rebak, "Oxide inclusion in the laser additive manufactured stainless steel and its effects on impact toughness and stress corrosion cracking behavior", *Journal of Nuclear Materials*, 499, pp 182-190, 2018
- Xiaoyuan Lou, Miao Song, Paul W. Emigh, Michelle A. Othon, Peter L. Andresen, "On the stress corrosion crack growth behaviour in high temperature water of 316L stainless steel made by laser powder bed fusion additive manufacturing", *Corrosion Science*, 128, pp 140-153, 2017

- Xiaoyuan Lou, Michelle A. Othon, Raul B. Rebak, "Corrosion fatigue crack growth of laser additively-manufactured 316L stainless steel in high temperature water", *Corrosion Science*, 127, pp 120-130, 2017

3. Conference Presentations

- Xiaoyuan Lou, Peter Andresen, Raul Rebak, "On the stress corrosion crack growth of laser additive manufactured 316L stainless steel", NACE Corrosion 2018 Conference and EXPO, Phoenix, Arizona, USA, April 15-19, 2018
- Xiaoyuan Lou, Raul Rebak, Myles Connor, Francis Bolger, David Webber, Gary Was, Miao Song, Mi Wang, Frederick List, "Additive stainless steel for nuclear: from material aspects to quality part", TMS 2018 Annual Meeting, Phoenix, AZ, USA, March 11-15, 2018
- Xiaoyuan Lou and Raul Rebak, "Microstructural effects on environmental assisted crack growth behaviors of austenitic stainless steel by laser powder bed fusion", TMS 2018 Annual Meeting, Phoenix, AZ, USA, March 11-15, 2018
- Miao Song, Mi Wang, Gary Was, Xiaoyuan Lou, Raul Rebak, "Effects of proton irradiation on microstructure in additively manufactured 316L stainless steel made by laser powder bed fusion", TMS 2018 Annual Meeting, Phoenix, AZ, USA, March 11-15, 2018
- Mi Wang, Miao Song, Xiaoyuan Lou, Raul Rebak, Gary Was, "IASCC behavior of additively manufactured 316L stainless steel in light water reactor environments", TMS 2018 Annual Meeting, Phoenix, AZ, USA, March 11-15, 2018
- (Invited Talk) Xiaoyuan Lou, Paul Emigh, Michelle Othon, “Environmental assisted cracking of the additively manufactured austenitic stainless steel in high temperature water”, TMS 2017 Annual Meeting, San Diego, CA, USA, Feb 26-Mar 2, 2017
- (Invited Talk) Xiaoyuan Lou, Fran Bolger, Myles Connor, “3D Metal Printing for Nuclear”, 2016 DOE Workshop: Pathway to SMR Commercialization, North Bethesda, MD, USA, 2016
- Xiaoyuan Lou, Paul Emigh, Michelle Othon, Martin Morra, Peter Andresen, "Stress corrosion cracking of the additively manufactured stainless steel by laser powder bed process”, 2016 Meeting of International Cooperative Group on Environmental Assisted Cracking of Water Reactor Materials, Qindao, China, May 15-20, 2016
- Xiaoyuan Lou, Evan Dolley, Martin Morra, Fran Bolger, Myles Connor, Ronald Horn, David Webber, "Stress corrosion cracking of the additively manufactured 316L stainless Steel in high temperature water", Materials Science & Technology 2015, Columbus, OH, USA, October 4-8, 2015

12. References

[1] L.E. Murr, S.M. Gaytan, D.A. Ramirez, E. Martinez, J. Hernandez, K.N. Amato, P.W. Shindo, F.R. Medina, R.B. Wicker, Metal fabrication by additive manufacturing using laser and electron beam melting technologies, J. Mater. Sci. Tech., 28 (2012) 1-14.
[2] D.D. Gu, W. Meiners, K. Wissenbach, R. Poprawe, Laser additive manufacturing of metallic components: materials, processes and mechanisms, Int. Mater. Rev. , 57 (2013) 133-164.

[3] W.E. Frazier, Metal additive manufacturing: a review, J. Mater. Eng. Perform., 23 (2014) 1917-1928.

[4] J.J. Lewandowski, M. Seifi, Metal additive manufacturing: a review of mechanical properties, Annu. Rev. Mater. Res., 46 (2016) 151-186.
[5] D. Herzog, V. Seyda, E. Wycisk, C. Emmelmann, Additive manufacturing of metals, Acta Mater., 117 (2016) 371-392.
[6] S.A. Anderson, Final technical report on laser direct manufacturing (LDM) for nuclear power components, in: USDOE-NE0000542 Final Technical Report, Lockheed Martin Corporation,, 2015.
[7] A.S. Wu, D.W. Brown, M. Kumar, G.F. Gallegos, W.E. King, An experimental investigation into additive manufacturing-induced residual stresses in 316L stainless steel, Metall. Mater. Trans. A 45 (2014) 6260-6270.
[8] L.E. Murr, E. Martinez, J. Hernandez, S. Collins, K.N. Amato, S.M. Gaytan, P.W. Shindo, Microstructures and properties of 17-4 PH stainless steel fabricated by selective laser melting, J. Mater. Res. Technol., 1 (2012) 167-177.
[9] Y. Tian, D. Mcallister, H. Colijn, M. Mills, D. Farson, M. Nordin, S. Babu, Rationalization of microstructure heterogeneity in Inconel 718 builds made by the direct laser additive manufacturing process, Metall Mater Trans A, 45 (2014) 4470-4483.
[10] P.A. Kobryn, S.L. Semiatin, The laser additive manufacture of Ti-6Al-4V, JOM, 53 (2001) 40-42.
[11] B. Verlee, T. Dormal, J. Lecomte-Beckers, Density and porosity control of sintered 316L stainless steel parts produced by additive manufacturing, Powder Metall., 55 (2012) 260-267.
[12] Z.Q. Wang, T.A. Palmer, A.M. Beese, Effect of processing parameters on microstructure and tensile properties of austenitic stainless steel 304L made by directed energy deposition additive manufacturing, Acta Mater., 110 (2016) 226-235.
[13] A.B. Spierings, N. Herres, G. Levy, Influence of the particle size distribution on surface quality and mechanical properties in AM steel parts, Rapid Prototyping J., 17 (2011) 195-202.
[14] J. Suryawanshi, K.G. Prashanth, U. Ramamurty, Mechanical behavior of selective laser melted 316L stainless steel, Mat. Sci. Eng. A-Struct., 696 (2017) 113-121.
[15] B. Van Hooreweder, D. Moens, R. Boonen, J.P. Kruth, P. Sas, Analysis of fracture toughness and crack propagation of Ti6Al4V produced by selective laser melting, Adv. Eng. Mat., 14 (2011) 92-97.
[16] V. Cain, L. Thijs, J. Van Humbeeck, B. Van Hooreweder, R. Knutsen, Crack propagation and fracture toughness of Ti6Al4V alloy produced by selective laser melting, Addit. Manuf., 5 (2015) 68-76.
[17] S. Leuders, M. Thone, A. Riemer, T. Niendorf, T. Troster, H.A. Richard, H.J. Maier, On the mechanical behaviour of titanium alloy TiAl6V4 manufactured by selective laser melting: fatigue resistance and crack growth performance, Int J Fracture, 48 (2013) 300-307.

[18] A. Riemer, S. Leuders, M. Thone, H.A. Richard, T. Troster, T. Niendorf, On the fatigue crack growth behavior in 316L stainless steel manufactured by selective laser melting, Eng. Fract. Mech. , 120 (2014) 15-25.
[19] X. Lou, M.A. Othon, R.B. Rebak, Corrosion fatigue crack growth of laser additively-manufactured 316L stainless steel in high temperature water, Corro. Sci., 127 (2017) 120-130.
[20] P.L. Andresen, C.L. Briant, Environmentally assisted cracking of types 304L/316L/316NG stainless steel in 288C water, Corrosion, 45 (1989) 448-463.
[21] P.L. Andresen, Environmentally assisted growth rate response of nonsensitized AISI 316 grade stainless steels in high temperature water, Corrosion, 44 (1988) 450.
[22] P.L. Andresen, M.M. Morra, Stress corrosion cracking of stainless steels and nickel alloys in high-temperature water, Corrosion, 64 (2008) 15-29.
[23] ASTM-A276, Standard Specification for Stainless Steel Bars and Shapes, in, ASTM International, 100 Barr Harbor Drive, West Conshohocken, PA 19428, USA.
[24] ASTM-E2109-01, Standard Test Methods for Determining Area Percentage Porosity in Thermal Sprayed Coatings, in, ASTM International, 100 Barr Harbor Drive, West Conshohocken, PA 19428, USA, 2014.
[25] M. Zietala, T. Durejko, M. Polanski, I. Kunce, T. Plocinski, W. Zielinski, M. Lazinska, W. Stepniowski, T. Czujko, K.J. Kurzydlowski, Z. Bojar, The microstructure, mechanical properties and corrosion resistance of 316L stainless steel fabricated using laser engineered net shaping, Mat. Sci. Eng. A-Struct., 677 (2016) 1-10.
[26] M.L. Montero-Sistiaga, S. Nardone, C. Hautfenne, J.V. Humbeeck, Effect of Heat Treatment on 316L Stainless Steel Produced by Selective Laser Melting (SLM), in: 2016 Annual International Solid Freeform Fabrication Symposium, Austin, Texas, USA 2016, pp. 558-565.
[27] D.W. Gandy, Innovative Manufacturing Process for Nuclear Power Plant Components via Powder Metallurgy & Hot Isostatic Pressing Method, in: US DOE Advanced Methods of Manufacturing Workshop, US Department of Energy, Germantown, MD, USA, 2016.
[28] A.J. Cooper, N.I. Cooper, A. Bell, J. Dhers, A.H. Sherry, A microstructural study on the observed differences in Charpy impact behavior between hot isostatically pressed and forged 304L and 316L austenitic stainless steel, Metall Mater Trans A, 46A (2015) 5126-5138.
[29] A.J. Cooper, N.I. Cooper, J. Dhers, A.H. Sherry, Effect of oxygen content upon the microstructural and mechanical properties of Type 316L austenitic stainless steel manufactured by hot isostatic
pressing, Metall Mater Trans A, 47A (2016) 4467-4475.
[30] T.S. Byun, T.G. Lach, Mechanical properties of 304L and 316L austenitic stainless steels after thermal aging for 1500 hours, in, Pacific Northwest National Laboratory, Richland, Washington, USA, 2016.
[31] Outokumpu, Handbook of stainless steel, Outokumpu Oyj, Espoo, Finland, 2013.
[32] S. Kozuh, M. Gojic, L. Kosec, Mechanical properties and microstructure of austenitic stainless steel after welding and post-weld heat treatment, Kovove Mater., 47 (2009) 253-262.
[33] AISC, Specification for safety-related steel structures for nuclear facilities, in, American Institute of Steel Construction, Chicago, IL, USA, 2012.
[34] X. Lou, M. Song, P.W. Emigh, M.A. Othon, P.L. Andresen, On the stress corrosion crack growth behaviour in high temperature water of 316L stainless steel made by laser powder bed fusion additive manufacturing, Corro. Sci., 128 (2017) 140-153.
[35] J.Y. Choi, S.K. Kim, Y.B. Kang, H.G. Lee, Compositional Evolution of Oxide Inclusions in Austenitic Stainless Steel during Continuous Casting, Steel Res. Int., 86 (2014) 284-292.
[36] Y.B. Kang, H.S. Kim, J. Zhang, H.G. Lee, Practical application of thermodynamics to inclusions engineering in steel, J. Phys. Chem. Solids, 66 (2005) 219-225.

[37] E.S. Surian, J.L. Trotti, T. Boniszewski, Effect of oxygen content on Charpy V-notch toughness in 3% Ni Steel SMA weld metal, Weld J. Res. Suppl, 71 (1992) 263s-268s.
[38] J.S. Liao, M. Hotta, A. Koshi, Effect of oxygen content on impact toughness of a fine-grained magnesium alloy, Mater. Lett., 65 (2011) 2995-2999.
[39] Q. Chao, V. Cruz, S. Thomas, N. Birbilis, P. Collins, A. Taylor, P.D. Hodgson, D. Fabijanic, On the enhanced corrosion resistance of a selective laser melted austenitic stainless steel, Scr. Mater., 141 (2017) 94-98.
[40] Y. Zhong, L.F. Liu, S. Wikman, D.Q. Cui, Z.J. Shen, Intragranular cellular segregation network structure strengthening 316L stainless steel prepared by selective laser melting, J. Nucl. Mater. , 470 (2016) 170-178.
[41] ASTM-E647-08, Standard test method for measurement of fatigue crack growth rates, in, ASTM International, 100 Barr Harbor Drive, West Conshohocken, PA 19428 USA, 2008.
[42] P.L. Andresen, IGSCC crack propagation rate measurement in BWR environments, in, SKI-Swedish Nuclear Power Inspectorate, Stockholm, Sweden, 1998.
[43] P.L. Andresen, SCC testing and data quality considerations, in: Ninth International Conference on Environmental Degradation of Materials in Nuclear Power Systems - Water Reactors, TMS, Newport Beach, California, USA, 2013.
[44] P.L. Andresen, Understanding and predicting stress corrosion cracking (SCC) in hot water, in: D. Feron, R.W. Staehle (Eds.) Stress Corrosion Cracking of Nickel Based Alloys in Water-cooled Nuclear Reactors: The Coriou Effect, Elsevier, 2016, pp. 169–238.
[45] X. Lou, R. Pathania, P.L. Andresen, Effects of chloride transients on stress corrosion crack in pressure vessel low alloy steels in high temperature water, Corro. Sci., 126 (2017) 305-316.
[46] K. Arioka, T. Yamada, T. Terachi, G. Chiba, Cold work and temperature dependence of stress corrosion crack growth of austenitic stainless steels in hydrogenated and oxygenated high temperature water, Corrosion, 63 (2007) 1114.
[47] H.P. Seifert, S. Ritter, The influence of ppb levels of chloride impurities on the stress corrosion crack growth behaviour of low-alloy steels under simulated boiling water reactor conditions, Corros. Sci., 108 (2016) 134-147.
[48] Q.J. Peng, S. Teysseyre, P.L. Andresen, G.S. Was, Stress corrosion crack growth in Type 316 stainless steel in supercritical water, Corrosion, 63 (2007) 1033-1041.
[49] L. Dong, Q. Peng, E. Han, W. Ke, L. Wang, Stress corrosion cracking in the heat affected zone of a stainless steel 308L-316L weld joint in primary water, Corro. Sci., 107 (2016) 172-181.
[50] L. Zhang, K. Chen, D. Du, W. Gao, P.L. Andresen, X. Guo, Characterizing the effect of creep on stress corrosion cracking of cold worked Alloy 690 in supercritical water environment, J. Nucl. Mater., 492 (2017) 32-40.
[51] L.W. Niedrach, A new membrane type pH sensor for use in high temperature high pressure water, J. Electrochem. Soc., 127 (1980) 2122.
[52] F.P. Ford, Environmentally assisted cracking of low-alloy steels, in, Electric Power Research Institute,, Palo Alto, CA, USA, 1992.
[53] C. Hahin, R.M. Stoss, B.H. Nelson, P.J. Reucroft, Effect of Cold Work on the Corrosion Resistance of Nonsensitized Austenitic Stainless Steels in Nitric Acid, Corrosion, 32 (1976) 229-238.
[54] Q.J. Peng, J. Kwon, T. Shoji, Development of a fundamental crack tip strain rate equation and its application to quantitative prediction of stress corrosion cracking of stainless steels in high temperature oxygenated water, J. Nucl. Mater., 324 (2004) 52-61.
[55] M.M. Hall, An alternative to the Shoji crack tip strain rate equation, Corro. Sci., 50 (2008) 2902-2905.

[56] L.M. Young, P.L. Andresen, T.M. Angeliu, Crack tip strain rate: estimates based on continuum theory and experimental measurement, in: NACE Corrosion 2001, NACE International, Houston, Texas, USA, 2001, pp. NACE-01131.
[57] W.C. Moshier, C.M. Brown, Effect of cold work and processing orientation on stress corrosion cracking behavior of Alloy 600, Corrosion, 56 (2000) 307-320.
[58] P.L. Andresen, M.M. Morra, J. Hickling, A. Ahluwalia, J. Wilson, Effect of deformation and orientation on SCC of alloy 690, in: NACE Corrosion 2009, NACE, Atlanta, GA, USA, 2009, pp. Paper No. 09412.
[59] K. Saeidi, X. Gao, Y. Zhong, Z.J. Shen, Hardened austenite steel with columnar sub-grain structure formed by laser melting, Mater. Sci. Eng., A 625 (2015) 221-229.
[60] Y.J. Kim, Analysis of oxide film formed on Type 304 stainless steel in 288°C water containing oxygen, hydrogen, and hydrogen peroxide, Corrosion, 55 (1999) 81-88.
[61] Y.J. Kim, Characterization of the oxide film formed on Type 316 stainless steel in 288°C water in cyclic normal and hydrogen water chemistries, Corrosion, 51 (1995) 849-860.
[62] ASTM-E399-09, Standard test method for linear-elastic plane-strain fracture toughness KIc of metallic materials, in, ASTM International, 100 Barr Harbor Drive, West Conshohocken, PA 19428, USA, 2009.
[63] D. Herzog, V. Seyda, E. Wycisk, C. Emmelmann, Additive manufacturing of metals, Acta Mater., 117 (2016) 371-392.
[64] D. Gu, W. Meiners, K. Wissenbach, R. Poprawe, Laser additive manufacturing of metallic components: materials, processes and mechanisms, International materials reviews, 57 (2012) 133-164.
[65] W.E. Frazier, Metal additive manufacturing: a review, Journal of Materials Engineering and Performance, 23 (2014) 1917-1928.
[66] S. Anderson, Final Technical Report on Laser Direct Manufacturing (LDM) for Nuclear Power Components, DOE-NE0000542, (2015).
[67] D.W. Gandy, Strategy/approach for qualification of nuclear components produced via additive manufacturing, in: US DOE Advanced Methods of Manufacturing Workshop, US Department of Energy, Germantown, MD, USA, (2016).
[68] A. Riemer, S. Leuders, M. Thöne, H. Richard, T. Tröster, T. Niendorf, On the fatigue crack growth behavior in 316L stainless steel manufactured by selective laser melting, Engineering Fracture Mechanics, 120 (2014) 15-25.
[69] B. Verlee, T. Dormal, J. Lecomte-Beckers, Density and porosity control of sintered 316L stainless steel parts produced by additive manufacturing, Powder Metallurgy, 55 (2012) 260-267.
[70] I. Tolosa, F. Garciandía, F. Zubiri, F. Zapirain, A. Esnaola, Study of mechanical properties of AISI 316 stainless steel processed by "selective laser melting", following different manufacturing strategies, The International Journal of Advanced Manufacturing Technology, 51 (2010) 639-647.
[71] X. Lou, M. Song, P.W. Emigh, M.A. Othon, P.L. Andresen, On the stress corrosion crack growth behaviour in high temperature water of 316L stainless steel made by laser powder bed fusion additive manufacturing, Corrosion Science, 128 (2017) 140-153.
[72] X. Lou, M.A. Othon, R.B. Rebak, Corrosion fatigue crack growth of laser additively-manufactured 316L stainless steel in high temperature water, Corrosion Science, 127 (2017) 120-130.
[73] X. Lou, P.L. Andresen, R.B. Rebak, Oxide inclusions in laser additive manufactured stainless steel and their effects on impact toughness and stress corrosion cracking behavior, J. Nucl. Mater., 499 (2018) 182-190.
[74] P. Scott, A review of irradiation assisted stress corrosion cracking, J. Nucl. Mater., 211 (1994) 101-122.

[75] P.L. Andresen, Irradiation-assisted stress corrosion cracking, Stress Corrosion Cracking: Materials Performance and Evaluation, ed. RH Jones (Materials Park, OH: ASM International, 1992), (1992) 181-210.
[76] G. Was, P. Andresen, Stress corrosion cracking behavior of alloys in aggressive nuclear reactor core environments, Corrosion, 63 (2007) 19-45.
[77] K. Fukuya, Current understanding of radiation-induced degradation in light water reactor structural materials, J. Nucl. Sci. Technol., 50 (2013) 213-254.
[78] T. Shoji, S.-i. Suzuki, K. Raja, Current status and future of IASCC research, J. Nucl. Mater., 258 (1998) 241-251.
[79] S.M. Bruemmer, E.P. Simonen, P.M. Scott, P.L. Andresen, G.S. Was, J.L. Nelson, Radiation-induced material changes and susceptibility to intergranular failure of light-water-reactor core internals, J. Nucl. Mater., 274 (1999) 299-314.
[80] G.S. Was, Fundamentals of radiation materials science: metals and alloys, Springer, 2016.
[81] Advanced Radiation Resistance Materials Interim Report, U.S. Department of Energy, 2018, in preparation.
[82] D.J. Edwards, E.P. Simonen, S.M. Bruemmer, Evolution of fine-scale defects in stainless steels neutron-irradiated at 275 C, J. Nucl. Mater., 317 (2003) 13-31.
[83] J.S. Janssen, M.M. Morra, D.J. Lewis, Sensitization and stress corrosion cracking of Alloy 800H in high-temperature water, Corrosion, 65 (2009) 67-78.